Technische Universität München

TUM School of Engineering and Design

Fixed Switching Frequency Direct Model Predictive Control for Variable Speed Drives

Qifan Yang

Vollständiger Abdruck der von der TUM School of Engineering and Design der Technischen Universität München zur Erlangung des akademischen Grades eines

Doktors der Ingenieurwissenschaften (Dr.-Ing.)

genehmigten Dissertation.

Vorsitz: Prof. Dr.-Ing. Hans-Georg Herzog
Prüfende der Dissertation:
1. Prof. Dr.-Ing. Dr. h.c. Ralph Kennel
2. Assoc. Prof. Dr.-Ing. Petros Karamanakos

Die Dissertation wurde am 15.04.2024 bei der Technischen Universität München eingereicht und durch die TUM School of Engineering and Design am 26.08.2024 angenommen.

Acknowledgment

First and foremost, I would like to thank my supervisor, Prof. Ralph Kennel, whose lecture on power electronics introduced me to this exiting field. The institute he led has provided us with an excellent environment where we can gain our technical competence and work in a free and pleasant atmosphere. The seven years of studying/working experience in this institute—three years in the master's program and four years in the Ph.D. program—was a significant period in my life and will always be a happy memory.

I am deeply grateful to my mentor, Prof. Petros Karamanakos, who has guided me with great detail since my master thesis and throughout the whole Ph.D. period. Many times, I was impressed by the high diligence and carefulness that he persistently put into our research work. This has always encouraged me to face difficulties and pursue meaningful research results. Moreover, he taught me how to conduct research work methodically and scientifically.

I feel fortunate to have worked together with many friendly colleagues. I would like to particularly mention Eyke Liegmann Aufderheide, who has always been patient and ready to help, especially when I had little experience with hardware, Wei Tian, who shared with me openly the test bench as well as plenty of other resources, and Stefan Klaß, who has helped me with the German translation of the abstract. Thanks to all their help and companionship, the work could be done, and the time could be pleasant.

Last but not least, I would like to thank Prof. Marcelo Lobo Heldwein, who took over the institute after Prof. Kennel retired. He has strongly supported me in finishing my Ph.D. work.

Munich, in March 2024
Qifan Yang

Abstract

This thesis presents a direct model predictive control (MPC) method for variable speed drives (VSDs) with grid-tied back-to-back converters. Specifically, the discussed MPC scheme directly manipulates the converter switching positions, thus possessing the fast transient responses that characterize direct controllers. Moreover, it operates the converter at a fixed switching frequency, while the output harmonic spectrum is discrete, with harmonics at non-triple, odd integer multiples of the fundamental frequency. As a result, the proposed method achieves similar or superior steady-state behavior than modulator-based control schemes. Thanks to the adopted modeling approach, the multiple control objectives of the systems, as well as the modulation problem, are formulated altogether as a constrained quadratic programming (QP) problem, thus avoiding an explicit modulator or any additional control loops in a cascaded or parallel structure. In doing so, not only is the controller design and commissioning process greatly simplified, but favorable performance in controller bandwidth and robustness is also achieved. This is in stark contrast to conventional linear control methods, where different cascaded and/or parallel control loops often lead to an adverse interaction with each other, particularly during transients and faults. The real-time implementation of the proposed direct MPC scheme is facilitated by a computationally efficient QP solver tailored to specific control problems. Consequently, as demonstrated by the presented experimental results, the proposed algorithm achieves superior performance for a wide range of operating conditions, rendering it a promising control approach for the studied systems.

Zusammenfassung

In dieser Arbeit wird eine direkte modellprädiktive Regelungsmethode (MPC) für drehzahlgeregelte Antriebe vorgestellt. Das diskutierte MPC-Schema beeinflusst direkt die Schaltzustände des Umrichters, wodurch das Verfahren das für direkte Regler charakteristische, schnelle Einschwingverhalten aufweist. Des Weiteren wird der Umrichter mit fester Schaltfrequenz betrieben. Das ausgangsseitige Frequenzspektrum ist dementsprechend von diskreter Form mit Harmonischen bei ungeraden ganzzahligen Vielfachen der Grundfrequenz, mit Ausnahme der Vielfachen von 3, die nicht im Spektrum enthalten sind. Infolgedessen erreicht die vorgeschlagene Methode ein ähnliches oder besseres stationäres Verhalten als Regelverfahren mit Modulator. Aufgrund des gewählten Modellierungsansatzes können die verschiedenen Regelungsziele des Systems/der Systeme sowie die Modulation gemeinsam als ein quadratisches Optimierungsproblem (QP) mit Nebenbedingungen formuliert werden. Auf einen expliziten Modulator oder zusätzliche Regelkreise in kaskadierter oder paralleler Struktur kann auf diese Weise verzichtet werden. Dadurch wird nicht nur die Auslegung und Inbetriebnahme des Reglers stark vereinfacht, sondern auch eine bessere Regelgüte hinsichtlich der Bandbreite und Robustheit des Reglers erreicht. Dies unterscheidet sich deutlich von konventionellen linearen Regelungsverfahren, bei denen sich verschiedene kaskadierte und/oder parallele Regelkreise häufig nachteilig gegenseitig beeinflussen, insbesondere während transienter Vorgänge und im Fehlerfall. Die Echtzeitimplementierung des vorgeschlagenen direkten MPC-Schemas wird durch einen rechnerisch effizienten Solver für QP-Probleme erleichtert, der auf die spezifische Regelungsproblematik angepasst ist. Die vorgestellten experimentellen Ergebnisse zeigen, dass der vorgeschlagene Algorithmus für eine große Auswahl von Betriebspunkten überlegene Ergebnisse liefert, was die Methode zu einem vielversprechenden Ansatz zur Regelung der untersuchten Systeme macht.

Contents

CHAPTER 1

Introduction

This thesis focuses on model predictive control for variable speed drives (VSDs) with grid-tied back-to-back converters. This beginning chapter introduces the background, motivations, and targeted objectives of this work. Then, the main contributions are summarized, and the structure of this thesis is outlined.

1.1 Background

1.1.1 Motivation

The observation of global warming and climate change has raised public concern about the environmental pollution caused by human activities, particularly the vast fossil fuel consumption since the industrial age. Under the pressure of this public concern, numerous industries are trying to replace their conventional plants with more environmentally friendly ones. For example, the ever-increasing number of electrical vehicles [1] and the significant growth of distributed power-generation systems using renewable energy sources [2] are two remarkable ongoing changes in the industry. This trend has led to an even broader use of power electronics (PEs) and, simultaneously, posed more challenges to their control design.

More specifically, three major technology trends are shaping the development of future PE systems [3]. First, the power rating keeps increasing. This leads to a more widely adoption of multi-level converters (MLCs) [4]. Because the series-connected power devices in MLCs distribute the voltage stress, the voltage rating can be increased while the current rating is kept at bay. Second, the power converters are turning into off-the-shelf products, which can be brought and put into operation quickly. This implies the requirement of a simple commissioning process. Third, the efficiency requirement of PE systems is getting more stringent. In some applications, such as flexible AC transmission and photovoltaic systems, close to 100% efficiency is expected. Moreover, the computational power of the control hardware is growing significantly. In many

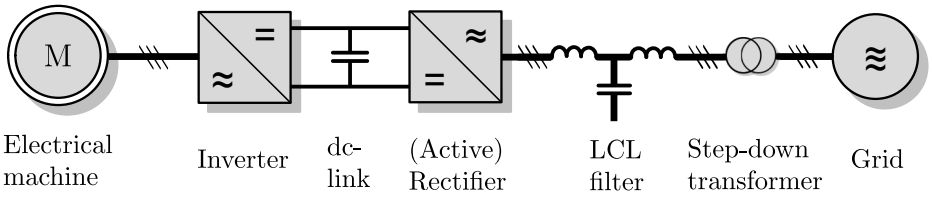

Figure 1.1: Grid-tied variable speed drive (VSD) systems.

applications, high-performance digital signal processors (DSPs), sometimes augmented by a large field-programmable gate array (FPGA), gradually replace the relatively small DSPs.

1.1.2 State-of-the-Art Schemes

A typical representative of an industrial PE system, grid-tied VSD systems are extensively used in numerous industrial applications, such as renewable power generation, energy storage, electrification, etc [3]. Fig. 1.1 shows the block diagram of such a system. It consists of an electrical machine connected to a voltage source inverter, a dc-link, and an (active) rectifier connected to the grid via an optional LCL filter and/or an optional step-down transformer. As an energy storage element, the dc-link capacitors divide the system into two parts, i.e., the machine- and grid-side converters.

The controller for such VSD systems is typically split into a machine-side and a grid-side controller. Each of them is usually subdivided into two cascaded control loops. On the grid side, the outer loop controls the dc-link voltage by regulating the active power exchange between the converter and grid. The inner loop manipulates the three-phase converter voltage to realize the commanded active and reactive power. Similarly, on the machine side, the outer loop controls the machine's speed by manipulating the torque reference, and the inner loop outputs a voltage reference, which operates the machine with the wanted electromagnetic torque and degree of magnetization.

Typically used control schemes in the inner loops are the so-called field-orient control (FOC) and voltage-oriented control (VOC), respectively, for the machine and grid side. Both schemes follow the same principle and formulate the control problem in a rotating orthogonal frame. For example, a rotating reference frame, which rotates synchronously with the machine's flux vector, is established for FOC. In this reference frame, the machine's stator current is separated into two orthogonal components, which are typically called the d- and q-component. The d-component directly relates the degree of machine magnetization, and the q-component the electromagnetic torque. Since these two components are, by definition, orthogonal, single-input single-output (SISO) linear controllers, e.g., proportional-integral (PI) controllers, are used to regulate them to their references. These linear controllers output real-valued reference voltages, which will be translated into gating signals for the converter by a modulator, e.g., a carrier-based pulse width modulator (CB-PWM) or a space vector modulator (SVM).

VOC is like the twin of FOC for the grid-side converter. It is established in a rotating orthogonal frame, which rotates synchronously with the grid voltage vector. In this reference frame, the d-component of the grid current directly relates to the active power, and the q-component the reactive power. When an LCL filter is installed—which is often necessary for attenuating switching harmonics—an additional active-damping control loop is required to stabilize the system. Besides, the converters in VSD systems are increasingly based on multi-level topologies,

such as the three-level (3L) neutral-point-clamped (NPC) topology. In such cases, balancing the converter's neutral point (NP) potential gives rise to another control problem.
The control and modulation methods mentioned above have been well-established and universally used in PE systems. However, they are facing three significant challenges. First, the switching behavior of the PEs is masked by the modulator. Thus the averaged converter output voltage is considered as the regulated variable. This approach works well when the modulation cycle is much shorter than the fundamental period. However, this condition doesn't always hold. For example, in medium-voltage VSD systems, the switching frequencies are limited to several hundred Hertz, and in high-speed motor applications, the fundamental frequencies can reach up to several thousand Hertz. In these applications, the delay introduced by the averaging and the evenly distributed switching pulses produced by the PWM seriously limit the control performance. Therefore, the switching nature of the converter should be directly addressed, and more flexible pulse patterns, e.g., optimized pulse patterns (OPPs), are preferred.
Second, multiple-input multiple-output (MIMO) control problems are decomposed into multiple SISO loops in cascaded or paralleled structures. However, these control loops are only decoupled while operating at (quasi) steady-state conditions. During transients and faults, they often lead to an adverse interaction with each other, limiting the controller bandwidth and robustness, causing large overshoots, and complicating the tuning of the control loops.
Third, the system's constraints are often addressed indirectly and coarsely via simple saturation, rate limiter, and anti-windup mechanism. As a result, relatively large safety margins need to be reserved, considering potential overshoots and limited controller bandwidth. This hinders the systems from operating at or close to their physical limits, preventing the hardware's potential from being fully exploited. Moreover, using rate limiters and anti-windup mechanisms introduces additional parameters, and thus further complicating the tuning of the controller.

1.1.3 Model Predictive Control

An alternative approach, model predictive control (MPC), has rapidly emerged in PE systems over the past decades. As a control method formulated in the time domain, MPC features a solid ability to address MIMO, high-order, and nonlinear systems straightforwardly. Moreover, MPC can easily include the constraints of the system inputs, states, and outputs in the problem formulation. These features allow MPC to address diverse control objectives with only one control loop, resulting in a simple yet versatile control structure. By doing so, favorable performance is achieved in terms of controller bandwidth and robustness, and the controller design and commissioning process is also simplified. The former allows the PE hardware to be operated at its total capacity, and the latter facilitates the production of power converter systems as off-the-shelf products.
However, solving the underlying optimization problem of MPC requires considerable effort. Especially for PE systems, where the sampling interval is usually only a few hundred, or even tens, of microseconds, solving the optimization problem in real-time is a significant challenge, and it remains a primary research direction in MPC. The tremendous increase of the computational power available in the control hardware, e.g., strong DSPs augmented with a large FPGA, has paved the way for the application of MPC in PE systems. However, it is equally important to investigate efficient solvers suitable for implementation on embedded systems and new MPC problem formulations tailored to the control problems at hand. Besides, MPC is susceptible

to model uncertainties and measurement noises. To tackle this, an observer, such as a Kalman filter (KF), can enhance the robustness of MPC schemes to parameter mismatches and other disturbances [5–7]. This, however, further increases the computational burden.

The most widely published MPC method for PEs is the direct MPC with reference tracking [8], also known as finite control set MPC (FCS-MPC) [9]. An FCS-MPC scheme for a 3L-NPC inverter was first presented in [10]. Albeit its simple structure, the presented FCS-MPC algorithm successfully controls the load current and NP potential at both steady-state and transient operation. However, the ℓ_1-norm in the objective function and the single-step prediction horizon lead to deteriorated control performance and potential closed-loop stability issues, especially when operating at low switching frequencies [8]. In order to improve the performance of FCS-MPC, it is favorable to use the ℓ_2-norm in the objective function [11], longer prediction horizons [12, 13], and shorter sampling intervals [8], which, however, pose a considerable computational challenge for a real-time implementation [14]. Besides, the direct control nature of the method, i.e., the controller directly generates the switching signals without requiring a dedicated modulation stage, gives rise to a variable switching frequency and a spread current harmonic spectrum as well as nondeterministic power losses and unequal distribution of the load, which can be undesirable in many applications [15, 16].

When the grid-side control is considered, the feature mentioned above of FCS-MPC is often unacceptable since the spread low-frequency harmonics cannot be effectively mitigated by a filter, meaning that the relevant harmonic grid standards may be violated. Therefore, indirect MPC, i.e., MPC with a dedicated modulation stage, such as CB-PWM or SVM [17], seems to be a better MPC-based derivative for the grid-side control [16, 18, 19]. Indirect MPC methods are mostly formulated as a quadratic program (QP), which can be easily solved analytically or numerically with the help of off-the-shelf solvers. For a modest computational burden, many indirect MPC methods, e.g., [18], formulate the control problem as unconstrained QPs. Albeit the unconstrained solution can be obtained easily, this under-utilizes the advantages of MPC in terms of its unique ability to systematically cope with the hard/soft constraints on manipulated variables, states, and outputs. As a result, these methods are prone to suboptimality and thus inferior performance. On the other hand, [16] imposes constraints on the modulating signal that is fed into the modulator, but it considers only nominal grid conditions, thus failing to demonstrate the full potential of MPC. In contrast, [19] accounts for faulty grid conditions, but only under symmetrical faults. Therefore, more challenging operating conditions are not addressed, such as asymmetrical grid faults where significant negative-sequence components appear in the grid voltage.

Regardless of the problem, indirect MPC dynamics are typically slower than direct control methods as the modulator limits them. To exploit the fast dynamics of direct MPC while tackling the problems of variable switching frequency and spread harmonic spectra, some direct MPC with precomputed switching sequences have been proposed [20, 21]. These methods employ switching patterns akin to CB-PWM/SVM and calculate optimal switching time instants or duty cycles for each voltage vector. However, the optimization problem in [20] is designed as an unconstrained one, thus exhibiting the disadvantages of such a formulation, as mentioned above. As for [21], the constrained optimization problem therein uses averaging in the cost function design. However, it cannot ensure zero—or even small—reference tracking error at the discrete time instants at steady-state operation. As a result, the ripple of the controlled variables is sampled and enters the control loop, thus leading to undesired low-frequency harmonics

and increased THDs.
Motivated by the shortcomings of the aforementioned MPC algorithms and the associated challenges, a direct MPC method with an implicit modulator for variable speed drive systems was proposed in [22] and refined in [23]. This method uses the gradient of the system output to predict the system's future behavior. In doing so, a simple and versatile modeling approach is employed, and the formulation of the optimal control problem as a constrained QP is enabled. This greatly facilitates the extension of the MPC scheme to different PE systems. Furthermore, the objective function is formulated such that a fixed switching frequency is ensured along with zero current ripple at the discrete time instants. As a result, low current distortions are produced with the harmonic power being concentrated at frequencies that are at odd, non-triple integer multiples of the fundamental.

1.2 Contributions

The direct MPC method in [22, 23] has to solve six constrained QPs (one for each possible switching sequence) in real time before concluding the global optimal solution. Consequently, the associated computational burden hindered the method's real-time implementation and, thus, experimental validation. To significantly reduce the computational complexity of the direct MPC method, a computationally efficient solution of the underlying MPC problem is first presented in this work, thus rendering its real-time implementation possible. The tackled challenges are twofold. First, although several open-source and commercial QP solvers are available [24, Section IV], they are commonly designed for general QP problems. Consequently, they may not be able to solve the MPC problem of interest in real-time within a short sampling interval since they do not exploit its structure. Indeed, the execution time greatly depends on various factors of the optimization problem, such as the size of the state and input vectors, the number of constraints, and the geometry of the feasible region, see [25] for a comprehensive assessment of different QP solvers. Therefore, this work develops an efficient and highly reliable gradient-based QP solver to facilitate the real-time implementation of the direct MPC algorithm. This algorithm exploits the properties of the QP problem at hand and achieves a fast and reliable convergence.
To further reduce the computational demands of the MPC algorithm, a method is introduced to deal with the second challenge of the real-time implementation, namely the need to solve a unique constrained QP for each of the six possible switching sequences within each sampling interval. Since not all switching sequences are reasonable candidate solutions at any given instant of the problem, the corresponding QPs may be ill-posed, leading to poor convergence rates and, thus, longer solving times. In order to tackle this issue, a mechanism is proposed that can detect the unsuited switching sequences with only a few computations. Thanks to this, only one or two QPs need to be solved at each sampling interval while still guaranteeing global optimality. As a result, the direct MPC scheme becomes computationally tractable without sacrificing its performance. This solver and the detection mechanism are published in [26].
Moreover, the above-mentioned direct MPC scheme is extended in this work to control a three-phase 3L-NPC inverter driving an induction machine (IM), i.e., the machine side of the grid-tied VSD system. Besides controlling the stator current, the developed control algorithm successfully and effectively balances the NP potential, even under challenging operating conditions,

such as at zero power factor (PF). In order to achieve this, the NP potential balancing is addressed in the same computational stage with the stator current control problem to allow for coordinated—and thus more effective—control. In doing so, a straightforward control structure results, thus demonstrating the high versatility of the developed algorithm and its ability to handle MIMO systems with complex and nonlinear dynamics. Moreover, the deadbeat solution is employed to reduce the number of candidate switching sequences, facilitating the real-time implementation of the proposed direct MPC strategy. As a result, the maximum number of candidate solutions remains relatively low and independent of the voltage levels of the converter. Therefore, this solution enables extending the proposed direct MPC method to multilevel converters without additional computational overhead. Furthermore, to further alleviate the computational load of the proposed MPC method, the QP algorithm developed in [26] is refined and tailored to the specific optimization problem at hand. Finally, due to the developed method's direct control principle, fast transients are achieved, limited only by the available dc-link voltage. This part of the work is published in [27].
Regarding the grid side, [23] employs the direct MPC scheme to control a grid-tied converter (GTC) with an LCL filter. However, [23] assumes strong grid and nominal operating conditions, i.e., operation under challenging operating conditions is not considered. This work extends the direct MPC method to control GTCs with LCL filters under adverse grid conditions. To this aim, a prediction model suitable for a wide range of operating conditions, including persistent disturbances—such as grid voltage harmonics—and unsymmetrical grid faults, is first derived. Subsequently, the control and modulation problems are designed as one computational entity in the form of a constrained QP. As a result, this direct control structure allows for favorable steady-state operation and superior dynamic performance. Such behavior is further enabled by the MIMO structure of the MPC algorithm as the adverse interaction between multiple control loops—which often causes oscillations during transients or even stability issues in critical operating conditions, especially when the parameters are not adequately tuned—is altogether avoided. Note that this superior performance is achieved without requiring a change of the control structure or the controller parameters depending on the grid conditions, which starkly contrasts conventional linear control schemes. This part of the work is published in [28].

1.3 Outline

This dissertation is structured as follows. Chapter 2 introduces a detailed modeling of the grid-tied VSD system, followed by a summary of its classical control and modulation schemes in Chapter 3. The proposed direct MPC scheme for the machine side is presented in Chapter 4, followed by its implementation and performance evaluation in Chapter 5. The extension of the direct MPC scheme to the grid side and its performance evaluation under adverse grid conditions are presented in Chapter 6 and 7, respectively. Finally, Chapter 8 concludes this work.

CHAPTER 2

Mathematical Model of the System

The physical system studied in this work is a variable-speed drive with a back-to-back power converter, as shown in Fig. 1.1, which is a typical representative of an industrial power electronics systems and is used on a global scale. This chapter presents a detailed description of this system, starting with a review of some fundamental concepts for modeling three-phase systems. Then, state-space models of induction machines (IM) and grid-tied converters (GTCs) with LCL filters are derived to describe the system's dynamics both during steady-state operations and transients. Finally, two- and three-level voltage source converters are described and modeled. All the definitions and models introduced in this chapter will be used throughout this dissertation.

2.1 Preliminaries

2.1.1 Three-Phase Systems

The majority of alternating-current (AC) systems are three-phase systems. Fig. 2.1 shows a simple yet representative example of such a system, where a three-phase voltage source is connected with a three-phase star-connected resistive-inductive load. For a balanced three-phase voltage source, the three instantaneous phase voltages at time t are [3]

$$v_a(t) = \sqrt{2}V_{\mathrm{ph}} \sin(\omega t) \tag{2.1a}$$

$$v_b(t) = \sqrt{2}V_{\mathrm{ph}} \sin(\omega t - \frac{2}{3}\pi) \tag{2.1b}$$

$$v_c(t) = \sqrt{2}V_{\mathrm{ph}} \sin(\omega t - \frac{4}{3}\pi)\,, \tag{2.1c}$$

where V_{ph} denotes the root-mean-square (rms) value of the phase voltage and ω the angular frequency. As shown in (2.1), the voltage waveforms of the three-phase abc have the same

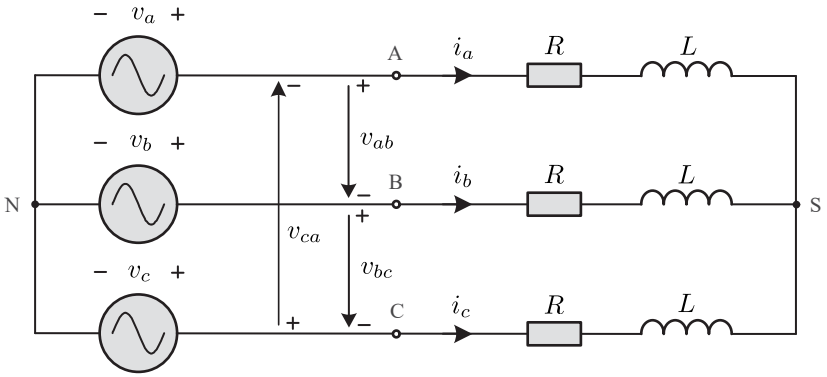

Figure 2.1: An example of balanced three-phase system [3].

amplitude and the same frequency, but their phases are shifted by $2\pi/3$ with respect to each other. Another commonly used definition is the line-to-line voltage [3]

$$v_{ab}(t) = v_a(t) - v_b(t) = \sqrt{2}V\sin(\omega t + \frac{1}{6}\pi) \tag{2.2a}$$

$$v_{bc}(t) = v_b(t) - v_c(t) = \sqrt{2}V\sin(\omega t - \frac{1}{2}\pi) \tag{2.2b}$$

$$v_{ca}(t) = v_c(t) - v_a(t) = \sqrt{2}V\sin(\omega t - \frac{7}{6}\pi)\,, \tag{2.2c}$$

which refer to the voltages between the phase terminals and have the rms value $V = \sqrt{3}V_{\text{ph}}$. For a balanced load, i.e., the resistances R and inductors L have the same value in each phase, the phase current can be easily calculated as [3]

$$i_a(t) = \sqrt{2}I_{\text{ph}}\sin(\omega t - \phi) \tag{2.3a}$$

$$i_b(t) = \sqrt{2}I_{\text{ph}}\sin(\omega t - \frac{2}{3}\pi - \phi) \tag{2.3b}$$

$$i_c(t) = \sqrt{2}I_{\text{ph}}\sin(\omega t - \frac{4}{3}\pi - \phi)\,, \tag{2.3c}$$

where $I_{\text{ph}} = V_{\text{ph}}/\sqrt{R^2 + (\omega L)^2}$ and $\phi = \tan^{-1}(\omega L/R)$. Fig. 2.2 shows the three-phase voltage and current waveforms, where $\hat{V} = \sqrt{2}V_{\text{ph}}$ and $\hat{I} = \sqrt{2}I_{\text{ph}}$ denote the peak values. Finally, the real power P, the reactive power Q, the apparent power S, and the power factor pf are given by [3]

$$P = 3V_{\text{ph}}I_{\text{ph}}\cos(\phi) \tag{2.4a}$$

$$Q = 3V_{\text{ph}}I_{\text{ph}}\sin(\phi) \tag{2.4b}$$

$$S = \sqrt{P^2 + Q^2} = 3V_{\text{ph}}I_{\text{ph}} \tag{2.4c}$$

$$\text{pf} = |\cos(\phi)| = \frac{P}{S}\,. \tag{2.4d}$$

2.1.2 Orthogonal Reference Frames

The modeling and analysis of three-phase systems are commonly done in orthogonal reference frames, whose axes are perpendicular to each other and can be stationary or rotating [3]. As

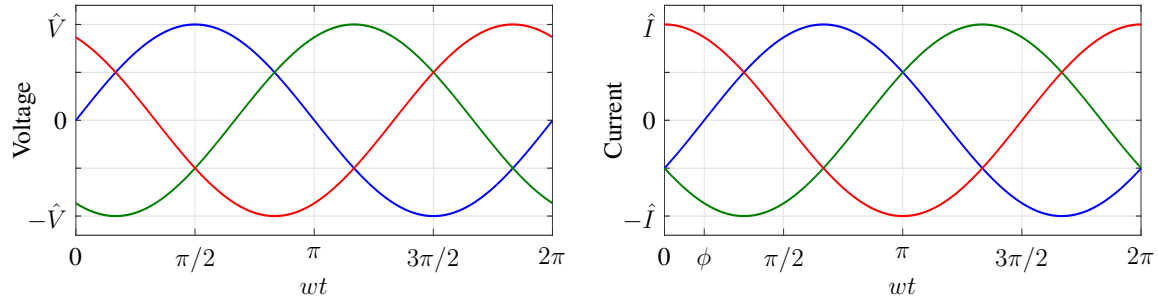

(a) Three-phase voltage. (b) Three-phase current.

Figure 2.2: Balanced three-phase voltages and currents.

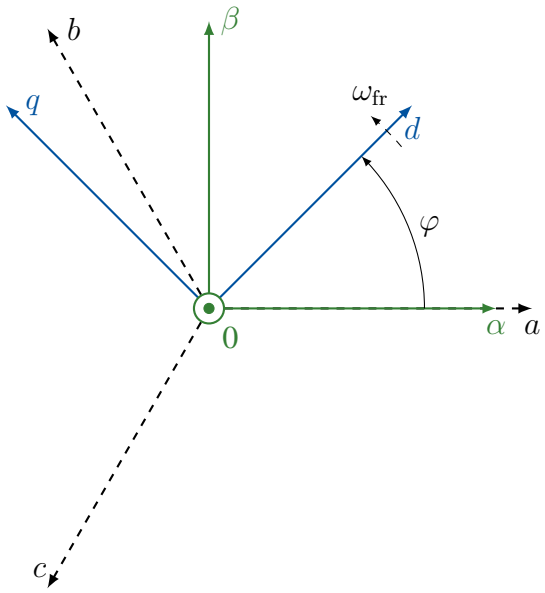

Figure 2.3: Definition of the stationary $\alpha\beta 0$ reference frame [3]

.

shown in Fig. 2.3, the stationary reference frame is established by the three axes α, β, and 0, where the α-axis is aligned with the a-axis of the three-phase abc frame. In contrast, the three axes of the rotating frame are called d, q, and 0, where the dq-axes rotate with a constant angular speed ω_{fr}.

Any variable $\boldsymbol{\xi}_{abc} = [\xi_a \ \xi_b \ \xi_c]^T$ in the three-phase abc system can be mapped into a variable $\boldsymbol{\xi}_{\alpha\beta 0} = [\xi_\alpha \ \xi_\beta \ \xi_0]^T$ in the $\alpha\beta 0$ frame, and vice versa, via the so-called Clarke and inverse Clarke transformation:

$$\boldsymbol{\xi}_{\alpha\beta 0} = \tilde{\boldsymbol{K}}\boldsymbol{\xi}_{abc} \quad \text{and} \quad \boldsymbol{\xi}_{abc} = \tilde{\boldsymbol{K}}^{-1}\boldsymbol{\xi}_{\alpha\beta 0}, \tag{2.5}$$

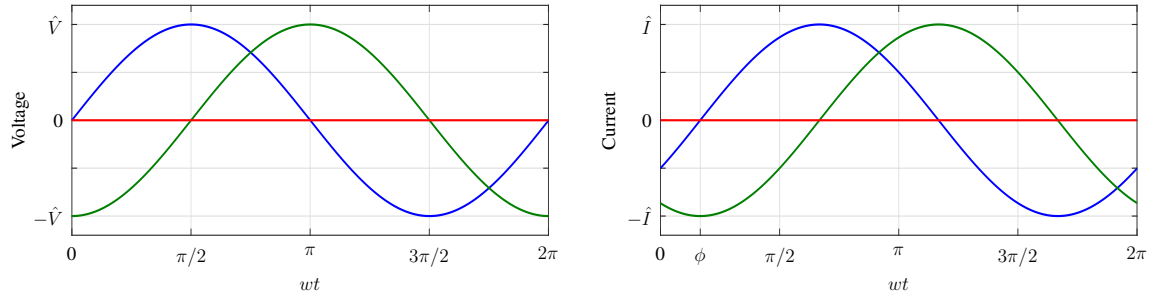

(a) Three-phase voltage.

(b) Three-phase current.

Figure 2.4: Balanced three-phase voltages and currents in the stationary $\alpha\beta 0$ reference frame.

where the transformation matrices are given by[1]

$$\tilde{\boldsymbol{K}} = \frac{2}{3}\begin{bmatrix} 1 & -\frac{1}{2} & -\frac{1}{2} \\ 0 & \frac{\sqrt{3}}{2} & -\frac{\sqrt{3}}{2} \\ \frac{1}{2} & \frac{1}{2} & \frac{1}{2} \end{bmatrix} \quad \text{and} \quad \tilde{\boldsymbol{K}}^{-1} = \begin{bmatrix} 1 & 0 & 1 \\ -\frac{1}{2} & \frac{\sqrt{3}}{2} & 1 \\ -\frac{1}{2} & -\frac{\sqrt{3}}{2} & 1 \end{bmatrix}. \tag{2.6}$$

Take the three-phase voltage and current in Fig. 2.2 as an example, they can be mapped into $\alpha\beta 0$ frame via the Clarke transformation, as shown in Fig. 2.4. The α- and β-components have the same amplitude and frequency as the corresponding waveforms in the abc reference frame, while the 0-component is zero. Indeed, the sum of the three-phase current is always zero for a star-connected three-phase system with its star point unconnected. This means the 0-component of the current is always zero regardless of the 0-component value of the voltage. Therefore, the 0-component in the Clarke transformation is often dropped by using the following (reduced) Clarke transformation [3]

$$\boldsymbol{\xi}_{\alpha\beta} = [\xi_\alpha \ \xi_\beta]^T = \boldsymbol{K}\boldsymbol{\xi}_{abc} \quad \text{and} \quad \boldsymbol{\xi}_{abc} = \boldsymbol{K}^{-1}\boldsymbol{\xi}_{\alpha\beta}, \tag{2.7}$$

with

$$\boldsymbol{K} = \frac{2}{3}\begin{bmatrix} 1 & -\frac{1}{2} & -\frac{1}{2} \\ 0 & \frac{\sqrt{3}}{2} & -\frac{\sqrt{3}}{2} \end{bmatrix} \quad \text{and} \quad \boldsymbol{K}^{-1} = \begin{bmatrix} 1 & 0 \\ -\frac{1}{2} & \frac{\sqrt{3}}{2} \\ -\frac{1}{2} & -\frac{\sqrt{3}}{2} \end{bmatrix}. \tag{2.8}$$

Finally, a variable $\boldsymbol{\xi}_{\alpha\beta}$ in the stationary $\alpha\beta$ reference frame can be mapped into a variable $\boldsymbol{\xi}_{dq} = [\xi_d \ \xi_q]^T$ in the rotating dq reference frame, and vice versa, via the so-called Park and inverse Park transformation [3]

$$\boldsymbol{\xi}_{dq} = \boldsymbol{P}(\varphi)\boldsymbol{\xi}_{\alpha\beta} \quad \text{and} \quad \boldsymbol{\xi}_{\alpha\beta} = \boldsymbol{P}^{-1}(\varphi)\boldsymbol{\xi}_{dq}, \tag{2.9}$$

with

$$\boldsymbol{P}(\varphi) = \begin{bmatrix} \cos(\varphi) & \sin(\varphi) \\ -\sin(\varphi) & \cos(\varphi) \end{bmatrix} \quad \text{and} \quad \boldsymbol{P}^{-1}(\varphi) = \boldsymbol{P}(-\varphi) = \begin{bmatrix} \cos(\varphi) & -\sin(\varphi) \\ \sin(\varphi) & \cos(\varphi) \end{bmatrix}, \tag{2.10}$$

[1]The factor $2/3$ in $\tilde{\boldsymbol{K}}$ is used to keep the amplitude of the three-phase signals preserved. Another commonly used type of Clarke transformation is the so-called power-invariant transformation, where the factor is $\sqrt{2/3}$.

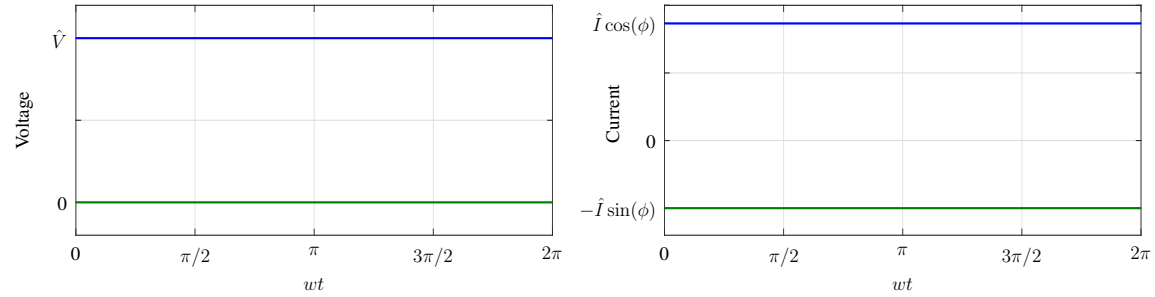

(a) Three-phase voltage. (b) Three-phase current.

Figure 2.5: Balanced three-phase voltages and currents in the rotating dq reference frame.

where φ is the angular position of the dq reference frame, as depicted in Fig. 2.3. Take the voltage and current waveforms in Fig. 2.4 as an example, and by setting the the angular speed of the reference frame $\omega_{\text{fr}} = \omega$ and the angular position $\varphi = \omega t - \pi/2$, the resulted waveforms in the dq reference frame are shown in Fig 2.5. As can be observed, the ac variables $\boldsymbol{v}_{\alpha\beta}$ and $\boldsymbol{i}_{\alpha\beta}$ are transformed into dc variables $\boldsymbol{v}_{dq}$ and $\boldsymbol{i}_{dq}$, respectively. As will be shown in the following chapter, this transformation enables simple linear PI controllers to regulate the control objects to their reference.

2.2 Indunction Machine

A three-phase induction machine (IM) is depicted in Fig. 2.6. For a squirrel-cage IM, only the stator windings are connected to an ac power source, and the alternating current in the stator winding generates an alternating magnetic field, which behaves like a rotating magnet. This rotating magnetic field induces voltage, and thus current, in the rotor windings, following Faraday's law of induction. Consequently, the interaction of the stator magnetic field and the rotor winding currents produces an electromagnetic torque and the rotational motion of the rotor.

As introduced in the last section, modeling a three-phase IM is commonly done in the stationary $\alpha\beta$ reference frame, with the α-axis aligned with the a-axis of the stator winding. All rotor quantities are referred to the stator side, i.e., like the modeling of transformers. This results in[2] [3]

$$\boldsymbol{v}_s = R_s \boldsymbol{i}_s + \frac{\mathrm{d}\boldsymbol{\lambda}_s}{\mathrm{d}t} \tag{2.11a}$$

$$\boldsymbol{0} = R_r \boldsymbol{i}_r + \frac{\mathrm{d}\boldsymbol{\lambda}_r}{\mathrm{d}t} - \begin{bmatrix} 0 & -1 \\ 1 & 0 \end{bmatrix} \omega_r \boldsymbol{\lambda}_r \,, \tag{2.11b}$$

where $\boldsymbol{v}_s$ denotes the stator voltage, $\boldsymbol{i}_s(\boldsymbol{i}_r)$ the stator (rotor) current, $\boldsymbol{\lambda}_s(\boldsymbol{\lambda}_r)$ the stator (rotor) flux linkage, $R_s(R_r)$ the stator (rotor) resistance, and ω_r is the electrical angular speed of the rotor.

[2] In the sequel of this work, the subscript $\alpha\beta$ used to denote variables in the stationary $\alpha\beta$-frame is omitted to simplify the notation. Variables in the three-phase abc- and rotating dq-frame are indicated with the corresponding subscript.

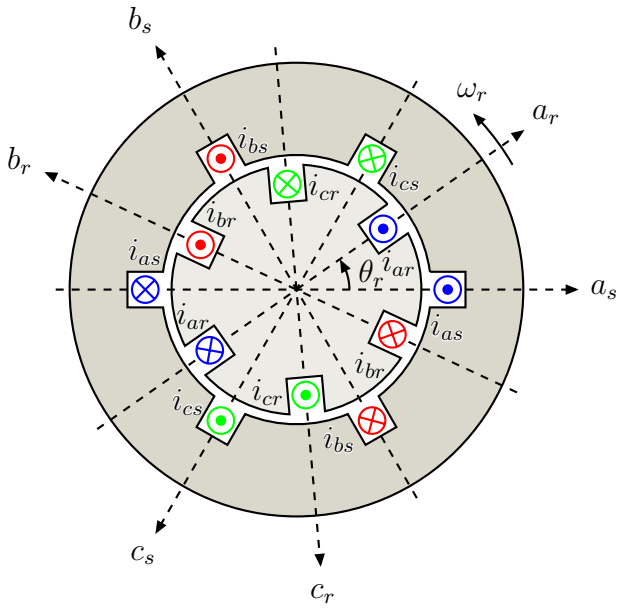

Figure 2.6: Induction machine and the three-phase abc coordinate system.

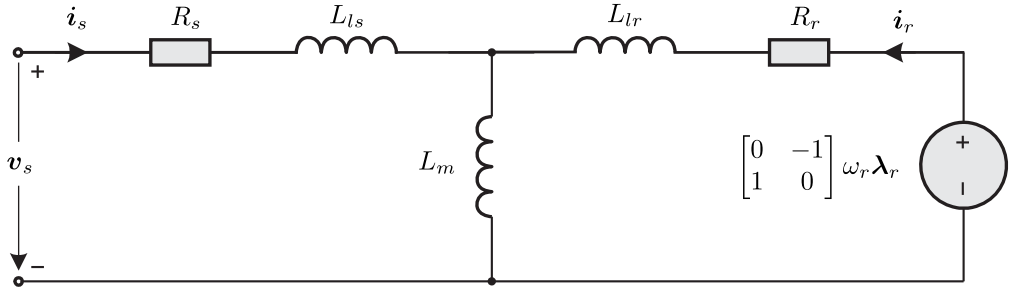

Figure 2.7: Equivalent circuit of a squirrel-cage IM in the stationary $\alpha\beta$ reference frame [3]

.

The flux linkages are calculated by

$$\boldsymbol{\lambda}_s = L_s \boldsymbol{i}_s + L_m \boldsymbol{i}_r \tag{2.12a}$$

$$\boldsymbol{\lambda}_r = L_r \boldsymbol{i}_r + L_m \boldsymbol{i}_s \,, \tag{2.12b}$$

where $L_{s(r)} = L_{ls(r)} + L_m$ is the stator (rotor) self-inductance, $L_{ls(r)}$ the stator (rotor) leakage inductance and L_m is the main (or magnetizing) inductance. Fig. 2.7 shows the equivalent circuit representation circuit of a squirrel-cage IM.
Moreover, the electromagnetic torque and rotational motion are calculated as

$$T_e = \frac{3}{2} p (\boldsymbol{\lambda}_s \times \boldsymbol{i}_s) \tag{2.13a}$$

$$M \frac{\mathrm{d}\omega_m}{\mathrm{d}t} = T_e - T_l \,, \tag{2.13b}$$

where $T_e(T_l)$ is the electromagnetic (load) torque, p the number of pole pairs, M the inertia of the rotor together with the mechanical load, and ω_m is the mechanical angular speed of the rotor.

Note that the electrical rotor speed is $\omega_r = p\omega_m$, and the expanded form of the cross product $\boldsymbol{\lambda}_s \times \boldsymbol{i}_s$ is $\lambda_{s\alpha} i_{s\beta} - \lambda_{s\beta} i_{s\alpha}$.
Equations (2.11)-(2.13) are the fundamental equation sets that govern the electrical and mechanical dynamics of IM. Based on them, other useful equations and state-space models can be derived. One commonly used state-space model is obtained by choosing the stator current $\boldsymbol{i}_s$ and rotor flux $\boldsymbol{\lambda}_r$ as states [3]:

$$\frac{\mathrm{d}\boldsymbol{i}_s}{\mathrm{d}t} = -\frac{1}{\tau_s}\boldsymbol{i}_s + (\frac{1}{\tau_r}\boldsymbol{I}_2 - \omega_r \begin{bmatrix} 0 & -1 \\ 1 & 0 \end{bmatrix})\frac{L_m}{D}\boldsymbol{\lambda}_r + \frac{L_r}{D}\boldsymbol{v}_s \tag{2.14a}$$

$$\frac{\mathrm{d}\boldsymbol{\lambda}_r}{\mathrm{d}t} = \frac{L_m}{\tau_r}\boldsymbol{i}_s + (-\frac{1}{\tau_r}\boldsymbol{I}_2 + \omega_r \begin{bmatrix} 0 & -1 \\ 1 & 0 \end{bmatrix})\boldsymbol{\lambda}_r\,, \tag{2.14b}$$

where

$$\tau_s = \frac{L_r D}{R_s L_r^2 + R_r L_m^2} \text{ and } \tau_r = \frac{L_r}{R_r} \tag{2.15}$$

are the transient stator time constant and rotor time constant, respectively. Besides, $D = L_s L_r - L_m^2$ and $\boldsymbol{I}_2$ is the two-dimensional identity matrix. For a more compact expression, the state-space model (2.14) can be grouped into the standard matrix form as

$$\frac{\mathrm{d}\boldsymbol{x}_m(t)}{\mathrm{d}t} = \boldsymbol{F}_m\boldsymbol{x}_m(t) + \boldsymbol{G}_m\boldsymbol{v}_s(t) \tag{2.16a}$$

$$\boldsymbol{y}_m(t) = \boldsymbol{C}_m\boldsymbol{x}_m(t)\,, \tag{2.16b}$$

where $\boldsymbol{x}_m = [i_{s\alpha}\ i_{s\beta}\ \lambda_{r\alpha}\ \lambda_{r\beta}]^T$ is the state vector [3] and $\boldsymbol{y}_m = [i_{s\alpha}\ i_{s\beta}]^T$ is the output vector. The matrices are

$$\boldsymbol{F}_m = \begin{bmatrix} -\frac{1}{\tau_s} & 0 & \frac{L_m}{\tau_r D} & \omega_r\frac{L_m}{D} \\ 0 & -\frac{1}{\tau_s} & -\omega_r\frac{L_m}{D} & \frac{L_m}{\tau_r D} \\ \frac{L_m}{\tau_r} & 0 & -\frac{1}{\tau_r} & -\omega_r \\ 0 & \frac{L_m}{\tau_r} & \omega_r & -\frac{1}{\tau_r} \end{bmatrix}, \quad \boldsymbol{G}_m = \begin{bmatrix} \frac{L_r}{D} & 0 \\ 0 & \frac{L_r}{D} \\ 0 & 0 \\ 0 & 0 \end{bmatrix} \tag{2.17a}$$

$$\boldsymbol{C}_m = \begin{bmatrix} 1 & 0 & 0 & 0 \\ 0 & 1 & 0 & 0 \end{bmatrix}. \tag{2.17b}$$

The exact discrete-time representation is obtained by integrating (2.16a) from $t = kT_s$ to $t = (k+1)T_s$ as [3]

$$\boldsymbol{x}_m(k+1) = \boldsymbol{A}_m\boldsymbol{x}_m(k) + \boldsymbol{B}_m\boldsymbol{v}_s(k) \tag{2.18a}$$

$$\boldsymbol{y}_m(k) = \boldsymbol{C}_m\boldsymbol{x}_m(k)\,, \tag{2.18b}$$

with

$$\boldsymbol{A}_m = \boldsymbol{e}^{\boldsymbol{F}_m T_s} \quad \text{and} \quad \boldsymbol{B}_m = \boldsymbol{F}_m^{-1}(\boldsymbol{A}_m - \boldsymbol{I}_4)\boldsymbol{G}_m \tag{2.19}$$

[3]Note that due to the slower mechanical dynamics, the angular speed of the rotor ω_r is treated as a (relatively slowly) varying parameter rather than as a state variable.

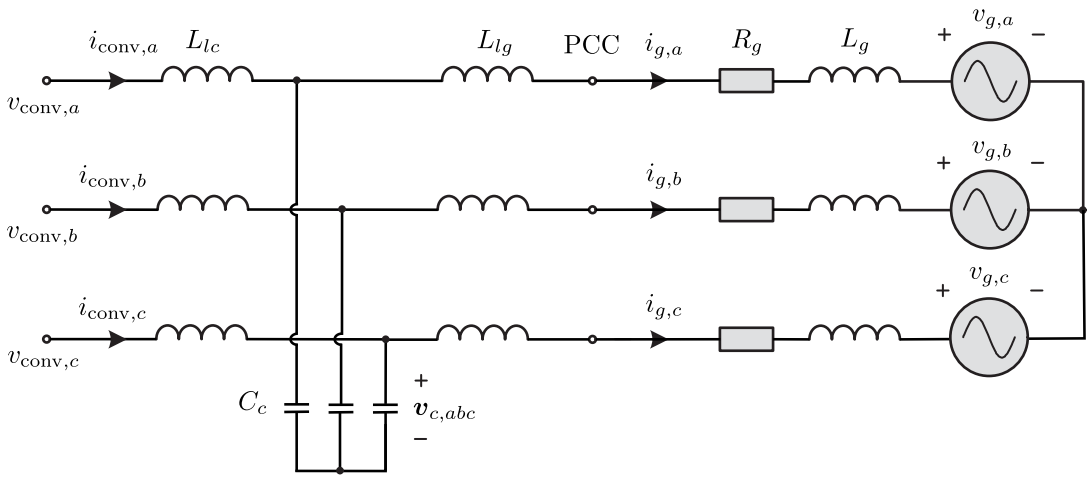

Figure 2.8: Grid-tied Converter system with an LCL filter.

where $k \in \mathbb{N} = \{0,\ 1,\ 2, \dots\}$ indicate the number of the sampling steps, T_s the sampling interval and $\boldsymbol{I}_4$ the four-dimensional identity matrix. Since the matrix exponentials usually pose computational difficulties, the forward Euler approximation is more commonly used and is usually sufficiently accurate for short sampling intervals in power electronic systems. In this case, the discrete-time system matrices are [3]

$$\boldsymbol{A}_m = \boldsymbol{I}_4 + \boldsymbol{F}_m T_s \quad \text{and} \quad \boldsymbol{B}_m = \boldsymbol{G}_m T_s \,. \tag{2.20}$$

Finally, the electromagnetic torque can be expressed in terms of the stator current and rotor flux as

$$T_e = \frac{3p}{2}\frac{L_m}{L_r}(\boldsymbol{\lambda}_r \times \boldsymbol{i}_s) \,. \tag{2.21}$$

2.3 Grid-tied Converters with LCL Filters

A grid-tied converter system with an LCL filter is depicted in Fig. 2.8. Since an accurate representation of the grid is usually not available, it is a common practice to approximately model the grid with the three-phase grid voltage $\boldsymbol{v}_g$, the grid resistance R_g and the grid inductance L_g [3]. PCC is the point of common coupling, where a converter can be connected via an (optional) LCL filter.

Let V_g denote the the rms grid line-to-line voltage and $Z_g = j\omega_g L_g + R_g$ the grid impedance. The short-circuit power is defined as [3]

$$S_{\mathrm{sc}} = 3\left(\frac{V_g}{\sqrt{3}}\right)^2 / |Z_g| = V_g^2 / |Z_g| \,, \tag{2.22}$$

which indicates the power flowing out from the grid to the PCC in case of a three-phase fault at the PCC. And the short-circuit ratio is defined as [3]

$$k_{\mathrm{sc}} = S_{\mathrm{sc}} / S_c \,, \tag{2.23}$$

where S_c is the rated power of the converter. Typically, $k_{\mathrm{sc}} \geq 20$ indicates a strong grid, which behaves like an ideal AC power source with a small impedance. Moreover, $k_{\mathrm{sc}} \leq 8$ indicates a

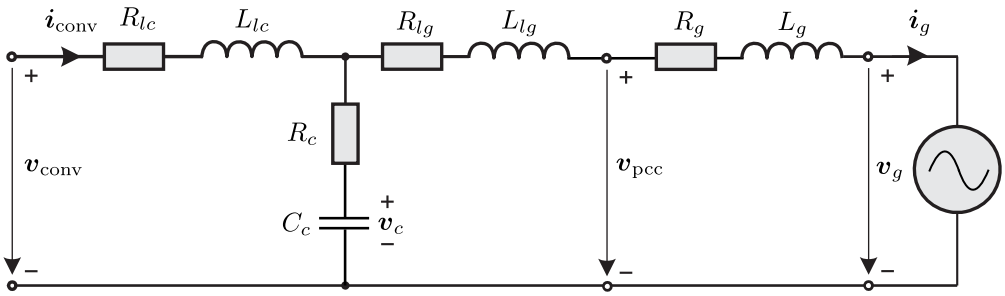

Figure 2.9: Equivalent circuit of the GTC with an LCL filter in the stationary ($\alpha\beta$) frame.

weak grid, where the non-negligible grid impedance significantly affects the system's behavior. Another characteristic quantity of the grid is the grid impedance ratio [3]

$$k_{\text{XR}} = X_g/R_g \quad \text{with} \quad X_g = \omega_g L_g \,. \tag{2.24}$$

The modeling of the grid-tied converter system is also commonly done in the stationary $\alpha\beta$ reference frame. This results in the equivalent circuit shown in Fig. 2.9, where $\boldsymbol{v}_{\text{conv}}$ ($\boldsymbol{v}_g$) and $\boldsymbol{i}_{\text{conv}}$ ($\boldsymbol{i}_g$) are the converter (grid) voltage and current, receptively, and $\boldsymbol{v}_c$ is the voltage across the filter capacitor. Besides, L_{lc} (L_{lg}) and R_{lc} (R_{lg}) are the converter (grid) side inductance and resistance of the filter, receptively, and C_c (R_c) is the capacitance (resistance) of the filter capacitor.

By applying Kirchhoff's circuit law to the equivalent circuit, the state-space model of the system is derived as

$$\frac{\mathrm{d}\boldsymbol{i}_{\text{conv}}}{\mathrm{d}t} = \frac{1}{L_{lc}}(-(R_{lc}+R_c)\boldsymbol{i}_{\text{conv}} + R_c\boldsymbol{i}_g - \boldsymbol{v}_c + \boldsymbol{v}_{\text{conv}}) \tag{2.25a}$$

$$\frac{\mathrm{d}\boldsymbol{i}_g}{\mathrm{d}t} = \frac{1}{L_{gr}}(-(R_{gr}+R_c)\boldsymbol{i}_g + R_c\boldsymbol{i}_{\text{conv}} + \boldsymbol{v}_c - \boldsymbol{v}_g) \tag{2.25b}$$

$$\frac{\mathrm{d}\boldsymbol{v}_c}{\mathrm{d}t} = \frac{1}{C_c}(\boldsymbol{i}_{\text{conv}} - \boldsymbol{i}_g) \tag{2.25c}$$

$$\frac{\mathrm{d}\boldsymbol{v}_g}{\mathrm{d}t} = \omega_g \begin{bmatrix} 0 & -1 \\ 1 & 0 \end{bmatrix} \boldsymbol{v}_g \,, \tag{2.25d}$$

where $R_{gr} = R_{lg} + R_g$ and $L_{gr} = L_{lg} + L_g$ are the grid-side equivalent resistance and reactance, respectively, and ω_g is the angular grid frequency. Similar to the modeling of IM, the state-space model (2.25) can be grouped into the standard matrix form as

$$\frac{\mathrm{d}\boldsymbol{x}_g(t)}{\mathrm{d}t} = \boldsymbol{F}_g\boldsymbol{x}_g(t) + \boldsymbol{G}_g\boldsymbol{v}_{\text{conv}}(t) \tag{2.26a}$$

$$\boldsymbol{y}_g(t) = \boldsymbol{C}_g\boldsymbol{x}_g(t) \,, \tag{2.26b}$$

where $\boldsymbol{x}_g = [\boldsymbol{i}_{\text{conv}}^T\ \boldsymbol{i}_g^T\ \boldsymbol{v}_c^T\ \boldsymbol{v}_g^T]^T$ is the state vector and $\boldsymbol{y}_g = [\boldsymbol{i}_{\text{conv}}^T\ \boldsymbol{i}_g^T\ \boldsymbol{v}_c^T]^T$ is the output vector.

The matrices are

$$\boldsymbol{F}_g = \begin{bmatrix} -\frac{R_{lc}+R_c}{L_{lc}}\boldsymbol{I}_2 & \frac{R_c}{L_{lc}}\boldsymbol{I}_2 & -\frac{1}{L_{lc}}\boldsymbol{I}_2 & \boldsymbol{0}_{2\times 2} \\ \frac{R_c}{L_{gr}}\boldsymbol{I}_2 & -\frac{R_{gr}+R_c}{L_{gr}}\boldsymbol{I}_2 & \frac{1}{L_{gr}}\boldsymbol{I}_2 & -\frac{1}{L_{gr}}\boldsymbol{I}_2 \\ \frac{1}{C_c}\boldsymbol{I}_2 & -\frac{1}{C_c}\boldsymbol{I}_2 & \boldsymbol{0}_{2\times 2} & \boldsymbol{0}_{2\times 2} \\ \boldsymbol{0}_{2\times 2} & \boldsymbol{0}_{2\times 2} & \boldsymbol{0}_{2\times 2} & \omega_g \begin{bmatrix} 0 & -1 \\ 1 & 0 \end{bmatrix} \end{bmatrix} \tag{2.27a}$$

$$\boldsymbol{G}_g = \frac{1}{L_{lc}}[\boldsymbol{I}_2 \; \boldsymbol{0}_{2\times 6}]^T \quad \text{and} \quad \boldsymbol{C}_g = [\boldsymbol{I}_6 \; \boldsymbol{0}_{6\times 2}]\,, \tag{2.27b}$$

where $\boldsymbol{I}_2$ ($\boldsymbol{I}_6$) is the two (six)-dimensional identity matrix. And, using the exact discretization, the discrete-time state-space model is derived as

$$\boldsymbol{x}_g(k+1) = \boldsymbol{A}_g\boldsymbol{x}_g(k) + \boldsymbol{B}_g\boldsymbol{v}_{\text{conv}}(k) \tag{2.28a}$$

$$\boldsymbol{y}_g(k) = \boldsymbol{C}_g\boldsymbol{x}_g(k)\,, \tag{2.28b}$$

with

$$\boldsymbol{A}_g = \boldsymbol{e}^{\boldsymbol{F}_g T_s} \quad \text{and} \quad \boldsymbol{B}_g = \boldsymbol{F}_g^{-1}(\boldsymbol{A}_g - \boldsymbol{I}_8)\boldsymbol{G}_g\,, \tag{2.29}$$

where $\boldsymbol{I}_8$ is the eight-dimensional identity matrix.

2.4 Three-Phase Voltage Source Converters

This section presents two commonly used voltage source converters, starting with the three-phase two-level converter, which has been pervasively used in various ac power electronic systems in low-power and in medium-power applications. The second topology is the three-level neutral point clamped (3L-NPC) converter, which is often considered more suitable in high-power medium-voltage applications, since the voltage stress is distributed over the series-connected power devices, and harmonics of the output voltage and current can be reduced.

2.4.1 Two-level Converter

A three-phase two-level converter is depicted in Fig. 2.10. The dc-link is usually comprised of some series-connected capacitors, and it is commonly modeled as two identical dc-link capacitors C_{dc} in series, which share equally the half of the dc-link voltage v_{dc}, and the middle point in between them is defined as the neutral point N. Besides, each leg of the three phases consists of two semiconductor switches S_x and $\bar{S}_x$, $x \in \{a,\ b,\ c\}$, with freewheeling diodes. The terminal of each phase is connected to the middle point between the two switches, and the phase voltage v_x is usually defined with respect to the dc-link neutral point N. Let $u_x \in \mathcal{U}_{2L} = \{-1,\ 1\}$ denote the switch position of phase x. The correspondence between the phase switch positions u_x, the phase voltages v_x, and the switching states S_x is shown in Table 2.1. Thus, the three-phase output voltage $\boldsymbol{v}_{abc} = [v_a\ v_b\ v_c]^T$ can be calculated from the three-phase switch position $\boldsymbol{u}_{abc} = [u_a\ u_b\ u_c]^T$ as

$$\boldsymbol{v}_{abc} = \frac{v_{\text{dc}}}{2}\boldsymbol{u}_{abc}\,. \tag{2.30}$$

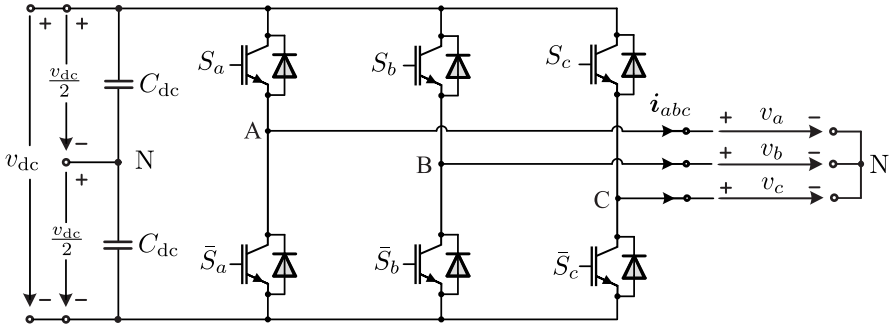

Figure 2.10: Three-phase two-level converter.

Table 2.1: Correspondence between the phase switch positions u_x, the phase voltages v_x, and the switching states S_x, $x \in \{a,\ b,\ c\}$, for 2L converters.

Switch position	phase voltage	Switching state	
u_x	v_x	S_x	$\bar{S}_x$
1	$v_{\mathrm{dc}}/2$	1	0
-1	-$v_{\mathrm{dc}}/2$	0	1

2.4.2 Neutral-Point-Clamped Three-level Converter

The model of a 3L-NPC converter is depicted in Fig. 2.11. The dc-link is comprised of two identical and series-connected capacitors, with their middle point defined as the neutral point (NP) N. Unlike the 2L converter, the NP of the 3L-NPC converter is connected with the three-phase legs, and its potential is floating. Let $v_{\mathrm{dc,up}}$ and $v_{\mathrm{dc,lo}}$ denote the voltages over the upper and lower dc-link capacitors, respectively. Then, the total dc-link voltage is [3]

$$v_{\mathrm{dc}} = v_{\mathrm{dc,up}} + v_{\mathrm{dc,lo}}\,, \tag{2.31}$$

and the NP potential

$$v_n = \frac{1}{2}(v_{\mathrm{dc,lo}} - v_{\mathrm{dc,up}})\,. \tag{2.32}$$

Moreover, each phase leg comprises four series-connected semiconductor switches S_{x1}-S_{x4} with freewheeling diodes. The middle point between S_{x1} and S_{x2}, as well as the middle point between S_{x3} and S_{x4}, is connected/clamped to the NP via the so-called clamping diodes. The terminal of each phase is connected to the middle point between S_{x2} and S_{x3}, and the phase voltage v_x is defined with respect to the neutral point N. Let $u_x \in \mathcal{U}_{3L} = \{-1,\ 0,\ 1\}$ denote the switch position of phase x. The correspondence between the phase switch positions u_x, the phase voltages v_x, and the switching states S_x is shown in Table 2.2. Thus, the three-phase output voltage $\boldsymbol{v}_{abc} = [v_a\ v_b\ v_c]^T$ can be calculated from the three-phase switch position $\boldsymbol{u}_{abc} = [u_a\ u_b\ u_c]^T$ as

$$\boldsymbol{v}_{abc} = \frac{v_{\mathrm{dc}}}{2}\boldsymbol{u}_{abc} - v_n|\boldsymbol{u}_{abc}|\,, \tag{2.33}$$

where $|\boldsymbol{u}_{abc}| = [|u_a|\ |u_b|\ |u_c|]^T$ is the component-wise absolute value of $\boldsymbol{u}_{abc}$. Moreover, the neutral point current i_n, which is defined as the current flowing out of the NP, as shown in Fig. 2.11, can be calculated as [3]

$$i_n = (1 - |u_a|)i_a + (1 - |u_b|)i_b + (1 - |u_c|)i_c. \tag{2.34}$$

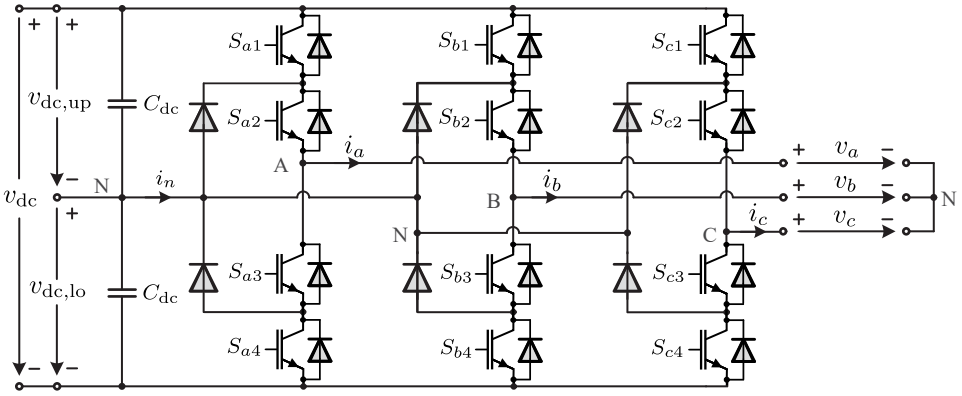

Figure 2.11: Three-phase three-level neutral point clamped converter [3].

Table 2.2: Correspondence between the phase switch positions u_x, the phase voltages v_x, and the switching states S_x, $x \in \{a,\ b,\ c\}$, for 3L-NPC converter [3].

Switch position	phase voltage	Switching state			
u_x	v_x	S_{x1}	S_{x2}	S_{x3}	S_{x4}
1	$v_{\mathrm{dc,up}}$	1	1	0	0
0	0	0	1	1	0
-1	-$v_{\mathrm{dc,lo}}$	0	0	1	1

For most of the three-phase loads, $i_a + i_b + i_c = 0$ always holds. Thus, equation (2.34) is simplified to

$$i_n = -|\boldsymbol{u}_{abc}|^T \boldsymbol{i}_{abc}, \tag{2.35}$$

where $\boldsymbol{i}_{abc} = [i_a\ i_b\ i_c]^T$ is the three-phase current. Finally, the evolvement of NP potential is described as [3]

$$\frac{\mathrm{d}v_n}{\mathrm{d}t} = -\frac{1}{2C_{\mathrm{dc}}} i_n = \frac{1}{2C_{\mathrm{dc}}} |\boldsymbol{u}_{abc}|^T \boldsymbol{i}_{abc}. \tag{2.36}$$

CHAPTER 3

Classic Control and Modulation Schemes

After decades of extensive studying on the control of power converters, linear control with pulse width modulation (PWM) has been well established and universally used in a wide range of applications. This classic control scheme usually adopts a cascaded structure to address each of the multiple control objectives individually in different control loops, as shown in Fig. 3.1. By doing so, simple single-input single-output (SISO) linear controllers, e.g., proportional-integral (PI) controllers, can be adopted to regulate the controlled variables to their references. Moreover, the real-valued outputs of the linear controllers are translated into the discrete-valued switching signals through the PWM. This chapter provides a review of this linear control scheme, starting by introducing the PWM. Then, two typical linear control schemes, i.e., field-oriented control (FOC) and voltage-oriented control (VOC), are presented, which are the most commonly used control schemes for drive systems and grid-tied converter systems, respectively.

3.1 Carrier-Based Pulse Width Modulation

Commonly used PWM schemes include carrier-based pulse width modulation (CB-PWM) and space vector modulation (SVM) [17], where the former is the simplest and most commonly used type. As will be explained later, CB-PWM with proper common-mode injection can become equivalent to SVM. This section presents the CB-PWM for both the 2L-converter and the 3L-NPC converter.

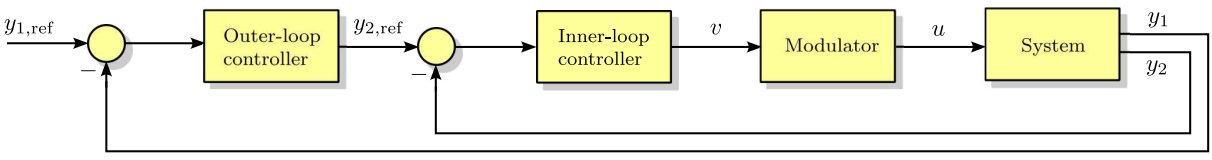

Figure 3.1: An example of the cascaded structure of linear control loops.

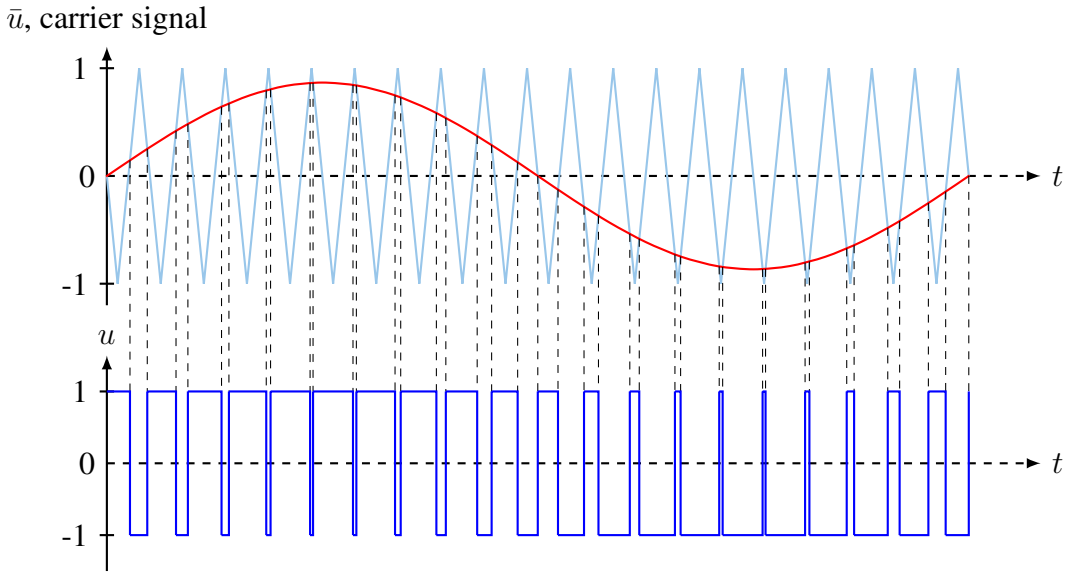

Figure 3.2: CB-PWM for 2L-converter.

3.1.1 CB-PWM for 2L-Converter

A 2L-converter can only produce the discrete voltage levels $-\frac{v_{\mathrm{dc}}}{2}$ and $\frac{v_{\mathrm{dc}}}{2}$ at its phase terminal. The function of PWM is to generate an appropriate switching signal u, such that the average value of the phase voltage within one switching cycle equals its reference. As the first step, it is a common practice to normalize the voltage reference v_{ref} by

$$\bar{u} = \frac{v_{\mathrm{ref}}}{v_{\mathrm{dc}}/2}\,, \tag{3.1}$$

where $\bar{u}$ is the modulating signal. Then, the modulating signal $\bar{u}$ is compared with a triangular carrier signal, which varies between -1 and 1 with the carrier frequency f_c, as shown in Fig. 3.2. When $\bar{u}$ is larger than the carrier signal, the switching position $u = 1$; otherwise, the switching position $u = -1$. Note that the carrier frequency f_c should be significantly higher than the fundamental frequency of the modulating signal, i.e., $f_c \gg f_1$.

Power electronic systems' control and modulation schemes are mostly digitally implemented nowadays. Thus, the reference voltage v_{ref}, as well as the modulating signal $\bar{u}$, is a sampled signal. Two regular sampling techniques are commonly used. The first one is called *symmetric sampling*, which samples the voltage reference once per carrier inverter T_c at the upper or lower triangular peaks. This results in a sampling frequency equals to the carrier frequency, i.e., $f_s = f_c$. The second one is called *asymmetric sampling*, which samples the voltage reference twice per carrier inverter at both the upper and lower triangular peaks. This results in a sampling frequency $f_s = 2f_c$.

Finally, it is a standard practice for three-phase CB-PWM to add a common-mode term to fully exploit the available dc-link voltage. One commonly used common-mode term is the min/max injection [29]

$$\bar{u}_0 = -\frac{1}{2}(\min(\bar{\boldsymbol{u}}_{abc}) + \max(\bar{\boldsymbol{u}}_{abc}))\,, \tag{3.2}$$

where $\bar{\boldsymbol{u}}_{abc} = [\bar{u}_a\ \bar{u}_b\ \bar{u}_c]$ is the three-phase modulating signal. This min/max common mode

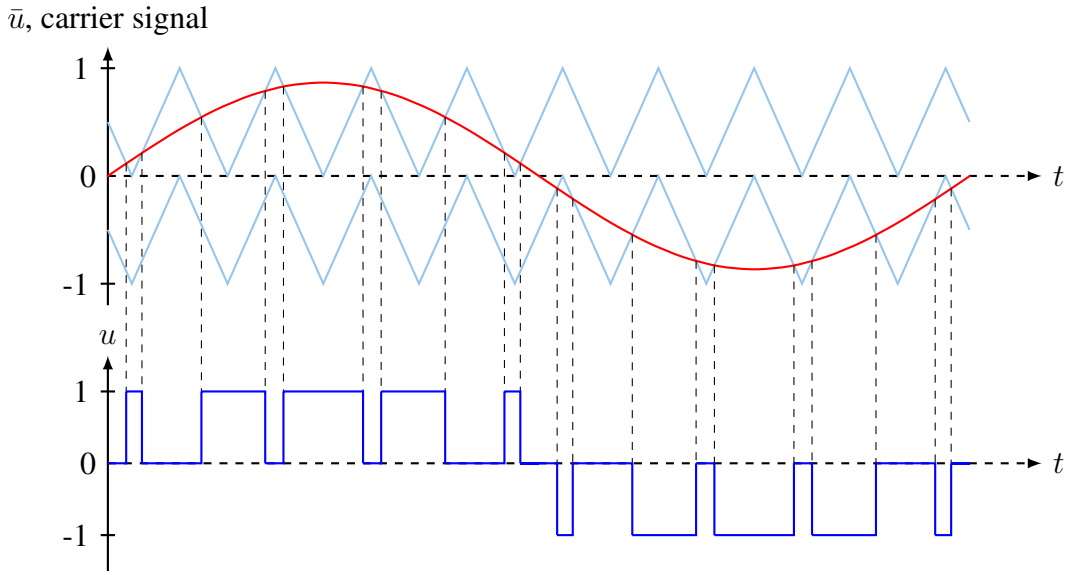

Figure 3.3: CB-PWM for 3L-NPC converter.

injection centers the three-phase modulating signal around zero and increases the linear modulation range by 15.5%. Moreover, it is shown in [29] that for 2L-converters, CB-PWM with this common mode injection is equivalent to SVM.

3.1.2 CB-PWM for 3L-NPC Converter

A 3L-NPC converter can produce the discrete voltage levels $-\frac{v_{\mathrm{dc}}}{2}$, 0 and $\frac{v_{\mathrm{dc}}}{2}$ at its phase terminal, assuming the NP potential to be zero. Similarly, the first step is normalizing the reference voltage by (3.1). Then, the modulating signal $\bar{u}$ is compared with two triangular carrier signals, of the same carrier frequency f_c and aligned in phase, as shown in Fig. 3.3. The upper triangular carrier signal varies between 1 and 0, while the lower one varies between 0 and -1. When the modulating signal $\bar{u}$ is less than both carrier signals, the switching position $u = -1$; when $\bar{u}$ is less than the upper carrier signal but greater than the lower carrier signal, the switching position $u = 0$; and when $\bar{u}$ is greater than both carrier signals, the switching position $u = 1$.
Similar to the CB-PWM for 2L-converters, a common mode term can be injected in the three-phase modulating signal $\bar{\boldsymbol{u}}_{abc}$ to fully exploit the available dc-link and make CB-PWM equivalent to SVM [29], i.e.,

$$\bar{u}_0 = \bar{u}_{0,m} + \frac{1}{2} - \frac{1}{2}(\min(\bar{\boldsymbol{u}}_{abc,m}) + \max(\bar{\boldsymbol{u}}_{abc,m}))\,, \tag{3.3}$$

where

$$\bar{u}_{0,m} = -\frac{1}{2}(\min(\bar{\boldsymbol{u}}_{abc}) + \max(\bar{\boldsymbol{u}}_{abc})) \tag{3.4a}$$

$$\bar{\boldsymbol{u}}_{abc,m} = (\bar{\boldsymbol{u}}_{abc} + \bar{u}_{0,m} + 1) \bmod 1\,. \tag{3.4b}$$

However, the common-mode component of $\bar{\boldsymbol{u}}_{abc}$ is usually used to balance the NP potential. In such cases, as will be shown in the following sections, a close-loop NP controller generates the common-mode term $\bar{u}_0$.

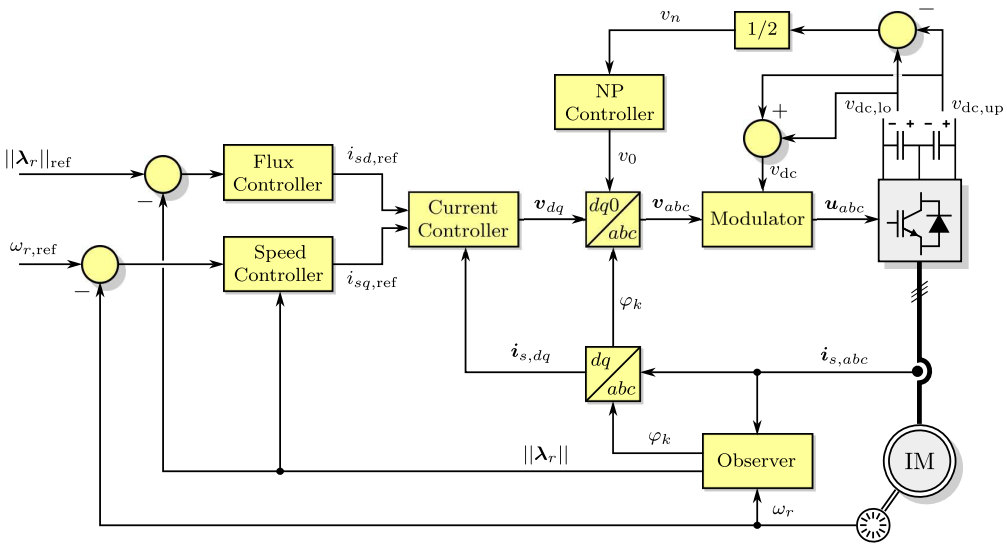

Figure 3.4: Block diagram of FOC.

3.2 Field-Oriented Control for Induction Machine

The field-oriented control (FOC) was introduced around 1970 [30]. It has become the most widely used control method for drive systems. A block diagram of the FOC is shown in Fig. 3.4. This section presents this classical control scheme by reviewing the principles and discussing some implementation issues.

3.2.1 Control Objectives and References

The foremost control objectives of IM are the electromagnetic torque and the air-gap flux. More specifically, the electromagnetic torque must be kept close to its reference. It can be either a constant or a variable generated by a speed controller so that the machine rotates at the desired speed and generates the required mechanical power. Besides, the magnitude of the air-gap flux should be maintained at a desired value since over-magnetization causes the saturation of the machine's rotor winding, and demagnetization may result in unstable operations. FOC is established in a rotating dq reference frame, which rotates synchronously with the rotor flux vector [1]. As will be explained later, the control of the flux magnitude and the electromagnetic torque are directly related to the d- and q-component of the stator current, respectively.

Let ω_s denote the synchronous angular frequency, which is the angular frequency of the stator/rotor flux. Moreover, φ_k denotes the angle of the rotor flux vector in the stationary $\alpha\beta$ frame. Firstly, all the variables in the IM state-space model (2.14) can be mapped into the

[1]Note that the rotating reference frame can also be aligned with the stator or the air-gap flux. The angular frequency of the stator flux is the same as that of the rotor flux, but their angles with respect to the stationary $\alpha\beta$ frame are different. However, since the working principle of FOC is the same regardless of which rotating frame is chosen, only the rotor-flux oriented FOC is introduced here.

rotor-flux-oriented rotating dq reference frame via the Park transformation

$$\boldsymbol{\xi}_{dq} = \boldsymbol{P}(\varphi_k)\boldsymbol{\xi}_{\alpha\beta} \quad \text{and} \quad \frac{\mathrm{d}\boldsymbol{\xi}_{dq}}{\mathrm{d}t} = \boldsymbol{P}(\varphi_k)\frac{\mathrm{d}\boldsymbol{\xi}_{\alpha\beta}}{\mathrm{d}t} - \omega_s \begin{bmatrix} 0 & -1 \\ 1 & 0 \end{bmatrix} \boldsymbol{P}(\varphi_k)\boldsymbol{\xi}_{\alpha\beta}\,. \tag{3.5}$$

This leads to

$$\frac{\mathrm{d}\boldsymbol{i}_{s,dq}}{\mathrm{d}t} = (-\frac{1}{\tau_s}\boldsymbol{I}_2 - \omega_s \begin{bmatrix} 0 & -1 \\ 1 & 0 \end{bmatrix})\boldsymbol{i}_{s,dq} + (\frac{1}{\tau_r}\boldsymbol{I}_2 - \omega_r \begin{bmatrix} 0 & -1 \\ 1 & 0 \end{bmatrix})\frac{L_m}{D}\boldsymbol{\lambda}_{r,dq} + \frac{L_r}{D}\boldsymbol{v}_{s,dq} \tag{3.6a}$$

$$\frac{\mathrm{d}\boldsymbol{\lambda}_{r,dq}}{\mathrm{d}t} = \frac{L_m}{\tau_r}\boldsymbol{i}_{s,dq} + (-\frac{1}{\tau_r}\boldsymbol{I}_2 - (\omega_s - \omega_r) \begin{bmatrix} 0 & -1 \\ 1 & 0 \end{bmatrix})\boldsymbol{\lambda}_{r,dq}\,. \tag{3.6b}$$

Since the d-axis of this rotating reference frame is aligned with the rotor flux, $\lambda_{r,q} = 0$ always holds, and the magnitude of the rotor flux $||\boldsymbol{\lambda}_r|| = \lambda_{rd}$. Therefore, (3.6b) can be rewritten into two scalar equations

$$\frac{\mathrm{d}||\boldsymbol{\lambda}_r||}{\mathrm{d}t} = \frac{L_m}{\tau_r} i_{sd} - \frac{1}{\tau_r}||\boldsymbol{\lambda}_r|| \tag{3.7a}$$

$$0 = \frac{L_m}{\tau_r} i_{sq} - (\omega_s - \omega_r)||\boldsymbol{\lambda}_r||\,. \tag{3.7b}$$

In steady state, the derivative of the rotor flux magnitude is zero, thus (3.7a) simplifies to

$$||\boldsymbol{\lambda}_r|| = L_m i_{sd}\,. \tag{3.8}$$

This means that a desired rotor flux magnitude $||\boldsymbol{\lambda}_r||_{\mathrm{ref}}$ in steady-state operation can be achieved by regulating the d-component of the stator current i_{sd} to its reference

$$i_{sd,\mathrm{ref}} = \frac{||\boldsymbol{\lambda}_r||_{\mathrm{ref}}}{L_m}\,. \tag{3.9}$$

Finally, by setting $\lambda_{rq} = 0$, the expression of the electromagnetic torque (2.21) is simplified to

$$T_e = \frac{3p}{2}\frac{L_m}{L_r}||\boldsymbol{\lambda}_r|| i_{sq}\,. \tag{3.10}$$

This implies that the electromagnetic torque is linearly related to the i_{sq}, provided that the rotor flux magnitude is constant. Therefore, one can set the reference of i_{sq} as

$$i_{sq,\mathrm{ref}} = \frac{2}{3p}\frac{L_r}{L_m}\frac{T_{e,\mathrm{ref}}}{||\boldsymbol{\lambda}_r||} \tag{3.11}$$

to obtain the desired electromagnetic torque $T_{e,\mathrm{ref}}$.

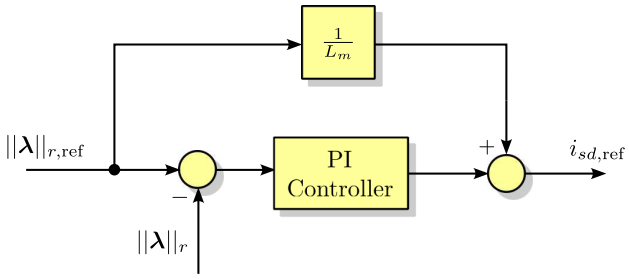

Figure 3.5: Flux control loop.

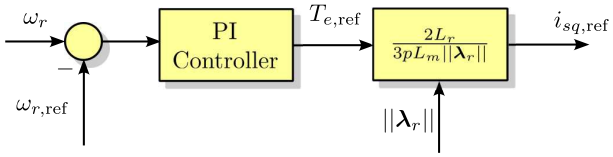

Figure 3.6: Speed control loop.

3.2.2 Linear Control in the Rotor-Flux-Oriented Reference Frame

3.2.2.1 Outer Flux and Speed Control Loops

As introduced in the last section, the stator current reference can be directly calculated from the flux and torque reference according to (3.9) and (3.11). However, in practical applications, the exact value of the machine parameters might not be available. Mismatches between the controller's parameters and the machine's actual values will result in steady-state reference tracking errors. To avoid this, PI controllers are usually adopted, as shown in Fig. 3.5, for the flux control loop. Moreover, faster reference tracking can be achieved by properly tuning the gains in PI controllers, which is favorable in many cases. For example, the machine's rotor flux usually needs to be pre-excited during the starting stage, a PI controller can significantly reduce the time required for this pre-excitation. Similarly, the PI-based speed control loop is shown in Fig. 3.6.

3.2.2.2 Inner Current Control Loops

The design of the current control loops is based on (3.6a), which can be rewritten as

$$v_{sd} = R_\sigma i_{sd} + L_\sigma \frac{\mathrm{d}i_{sd}}{\mathrm{d}t} - \omega_s L_\sigma i_{sq} - R_r \frac{L_m}{L_r^2} ||\boldsymbol{\lambda}_r|| \tag{3.12a}$$

$$v_{sq} = R_\sigma i_{sq} + L_\sigma \frac{\mathrm{d}i_{sq}}{\mathrm{d}t} + \omega_s L_\sigma i_{sq} + \omega_r \frac{L_m}{L_r} ||\boldsymbol{\lambda}_r|| \,, \tag{3.12b}$$

where

$$R_\sigma = R_s + R_r \frac{L_m^2}{L_r^2} \quad \text{and} \quad L_\sigma = (1 - \frac{L_m^2}{L_s L_r}) L_s \tag{3.13}$$

are the equivalent resistance and the total leakage inductance, respectively.
It can be observed from (3.12) that when only considering the first two items on the right-hand side of the equation, the relationship between the voltage and current of each respective axis is just a first-order differential equation. Moreover, many well-established methods exist for

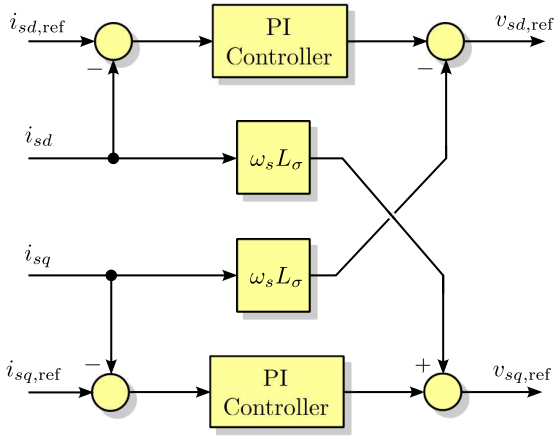

Figure 3.7: Current control loop of FOC.

designing the control for a first-order system, e.g., zero-pole placement method. Motivated by this, the third and fourth terms on the right-hand side of the equation are often either compensated with feed-forward terms or simply neglected. Then, two independent PI controllers can regulate the currents to their references. Fig. 3.7 shows a typical design of the current control loop.

3.2.3 Observers

The angular position and the magnitude of the rotor flux are usually not measurable, they need to be calculated/estimated by observers. The literature contains various (rotor) flux observer schemes, which can be grouped into two groups: the indirect method and the direct method. The following introduces two commonly used schemes from both methods.

3.2.3.1 Indirect Method

The indirect method requires only a small number of computations and is thus favorable when the computational power of the control platform is very limited. It reconstructs the synchronous angular frequency ω_s using the rotor speed ω_r and the slip (angular) frequency $\omega_{\mathrm{sl}} = \omega_s - \omega_r$. The rotor angular position φ_r and speed ω_r are measured with an incremental encoder, and the slip frequency is calculated according to (3.7b) as

$$\omega_{\mathrm{sl}} = \frac{L_m}{\tau_r ||\boldsymbol{\lambda}_r||} i_{sq} \,. \tag{3.14}$$

Then, adding ω_{sl} to ω_r yields the synchronous speed ω_s, and adding the integral of ω_{sl} to φ_r yields the angular position of the rotor flux. The magnitude of the rotor flux can be calculated with (3.7a) adopting the forward-Euler discretization as

$$||\boldsymbol{\lambda}_r||(k+1) = (1 - \frac{T_s}{\tau_r})||\boldsymbol{\lambda}_r||(k) + \frac{L_m}{\tau_r} T_s i_{sd}(k) \,. \tag{3.15}$$

Noticeably, the slip frequency and the rotor flux magnitude are calculated in an open-loop manner. Therefore, this indirect method is vulnerable to machine parameter variations.

3.2.3.2 Direct Method with Kalman Filter

The direct method estimate the rotor flux vector based on the measured stator currents and the stator voltages. Considering the model parameter uncertainties and measurement noises, a Klaman Filter (KF) is recommended to be implemented. Based on the discrete-time state-space model (2.18), the KF equations are [7]

$$\begin{aligned}
\hat{\boldsymbol{x}}_m(k+1|k) &= \boldsymbol{A}_m\hat{\boldsymbol{x}}_m(k) + \boldsymbol{B}_m\boldsymbol{v}_s(k) \\
\boldsymbol{P}(k+1|k) &= \boldsymbol{A}_m\boldsymbol{P}(k|k)\boldsymbol{A}_m^T + \boldsymbol{Q} \\
\boldsymbol{L}(k+1) &= \boldsymbol{P}(k+1|k)\boldsymbol{C}_m^T(\boldsymbol{C}_m\boldsymbol{P}(k+1|k)\boldsymbol{C}_m^T + \boldsymbol{R})^{-1} \\
\hat{\boldsymbol{x}}_m(k+1|k+1) &= \hat{\boldsymbol{x}}_m(k+1|k) \\
&\quad + \boldsymbol{L}(k+1)(\boldsymbol{y}_m(k+1) - \boldsymbol{C}_m\hat{\boldsymbol{x}}_m(k+1|k)) \\
\boldsymbol{P}(k+1|k+1) &= \boldsymbol{P}(k+1|k) - \boldsymbol{L}(k+1)\boldsymbol{C}_m\boldsymbol{P}(k+1|k)\,,
\end{aligned} \tag{3.16}$$

where $\boldsymbol{L}$ is the Kalman gain matrix, $\hat{\boldsymbol{x}}_m$ is the estimated state, $\boldsymbol{P}$ is the error covariance matrix, while $\boldsymbol{Q}$ and $\boldsymbol{R}$ are the system noise and measurement covariance matrices, respectively.

3.2.4 Neutral Point Potential Balancing

In CB-PWM, the neutral point potential balancing can be achieved by manipulating the common-mode voltage (CMV). In [31], the effect of the inverter's CMV on the average current flowing out of or into the NP is analyzed in detail, showing that balancing the NP potential can be achieved by controlling the CMV. Based on this principle, a simple closed-loop NP control based on a proportional-integral (PI) controller is introduced in [32]. However, this control loop becomes unstable when the power factor of the inverter's load approaches zero. For this reason, the NP control loop must be disabled when working in such a region. Moreover, the CMV must be appropriately saturated to avoid any modulation distortion, especially when the modulation index is high. In order to overcome these issues, a more exact analysis and calculation of the CMV required for NP potential balancing is presented in [33], and a so-called searching-optimization algorithm is provided therein, which finds the theoretical optimum CMV for controlling the NP potential. However, this algorithm is considerably complicated to implement.

3.3 Voltage-Oriented Control for Grid-tied Converter with LCL filter

Similar to the FOC for the IM, the voltage-oriented control (VOC) for grid-tied converters(GTCs) is typically based on the use of a rotating dq reference frame that rotates synchronously at the grid angular frequency ω_g. Typically, the dq frame is oriented such that the d-axis is aligned with the grid voltage vector. A block diagram of VOC is shown in Fig. 3.8. This section briefly reviews this control scheme.

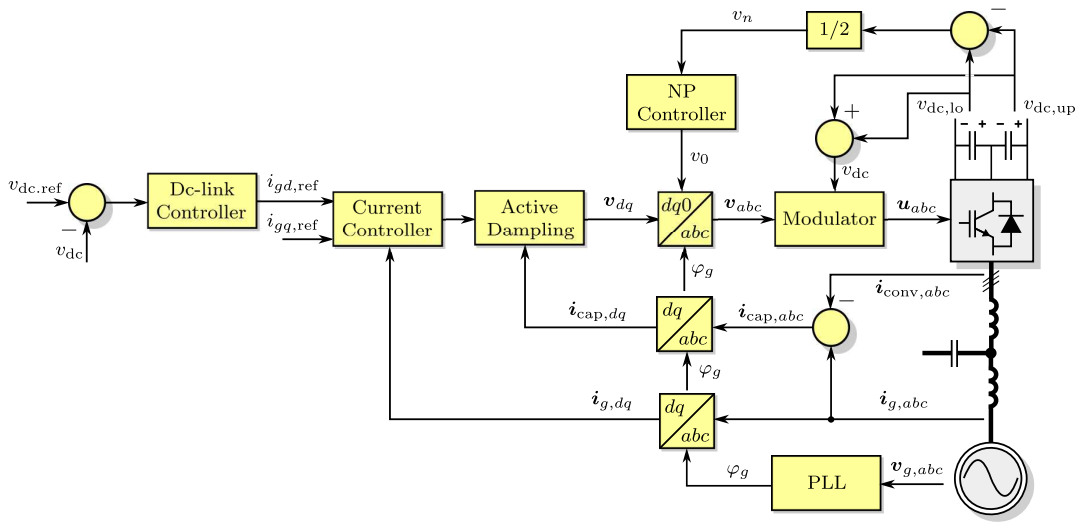

Figure 3.8: Block diagram of VOC.

3.3.1 Control Objectives and References

First, the active power P and reactive power Q exchanging at the PCC must be controlled. The former should equal the power consumed/generated by the other side of the back-to-back converter system, i.e., the IM in the grid-tied VSD system so that the dc-link voltage is kept constant. Moreover, the latter is typically regulated to 0 to obtain a unity power factor. Based on the instantaneous power theory [34], the active and reactive power exchanging at the PCC can be calculated as

$$P = \frac{3}{2}\boldsymbol{v}_{\mathrm{pcc}} \cdot \boldsymbol{i}_g = \frac{3}{2}(v_{\mathrm{pcc},\alpha} i_{g,\alpha} + v_{\mathrm{pcc},\beta} i_{g,\beta}) \tag{3.17a}$$

$$Q = \frac{3}{2}||\boldsymbol{v}_{\mathrm{pcc}} \times \boldsymbol{i}_g|| = \frac{3}{2}|v_{\mathrm{pcc},\alpha} i_{g,\beta} - v_{\mathrm{pcc},\beta} i_{g,\alpha}| \,. \tag{3.17b}$$

In the grid voltage oriented dq frame, $\boldsymbol{v}_{\mathrm{pcc},dq} = [\hat{V}_g \; 0]^T$ always holds, where $\hat{V}_g$ is the magnitude of the voltage vector[2]. Thus, the calculation of the active and reactive power is simplified to

$$P = \frac{3}{2}\hat{V}_g i_{g,d} \tag{3.18a}$$

$$Q = \frac{3}{2}|\hat{V}_g i_{g,q}| \,. \tag{3.18b}$$

This means the active and reactive power are proportional to $i_{g,d}$ and $i_{g,q}$, respectively. Therefore, a desired power exchange P_{ref} and Q_{ref} can be achieved by regulating the d- and q-component of the grid current to their references $i_{gd,\mathrm{ref}} = 2P_{\mathrm{ref}}/(3\hat{V}_g)$ and $i_{gq,\mathrm{ref}} = 2Q_{\mathrm{ref}}/(3\hat{V}_g)$, respectively.

Besides, to ensure a safe and secure network operation, international standards, e.g., the IEEE 519 grid standard [35], impose limits on the current harmonics at the PCC. Fig. 3.9 shows an example of the maximum current harmonic limits at PCC for a grid with short circuit ratio

[2]Note that only the fundamental wave are considered here. The analysis with the harmonics will be presented in later sections.

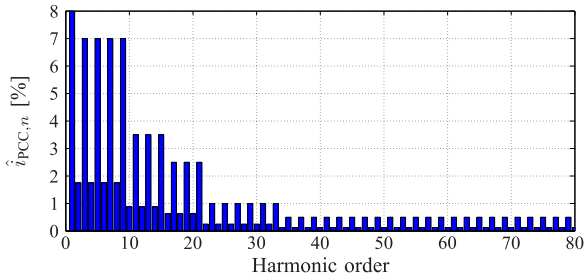

Figure 3.9: Current harmonic limits at the PCC on the IEEE 519 standard for short circuit ratio $k_{\mathrm{sc}} = 20$.

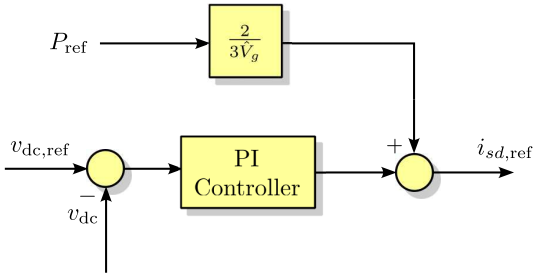

Figure 3.10: Dc-linnk voltage control loop.

$k_{\mathrm{sc}} = 20$. Generally, the smaller the short circuit ratio is, the more strict the harmonic limits are.

3.3.2 Linear Control in the Grid-Voltage-Oriented Reference Frame

3.3.2.1 Dc-link Voltage Control

The dc-link voltage control can be achieved by controlling the active power exchanged between the converter and the grid, which is directly related to the d component of the grid current, as explained in the last section. A PI controller is typically used in this control loop, as shown in Fig. 3.10. Note that $v_{\mathrm{dc}} \geq \sqrt{3}\hat{V}_g$ should be ensured to allow current controllability, and v_{dc} should not be too high in order to avoid high losses on the semiconductor switches.

3.3.2.2 Grid Current Control

In the next step, the grid current should be regulated to its reference. During the design of the current control loop, the capacitor in the LCL filter is often neglected for simplicity [36] since its influence on the current at low-frequency range is negligible. Then, the dynamic of the system is simplified as

$$\boldsymbol{v}_{\mathrm{conv}} = R_t \boldsymbol{i}_g + L_t \frac{\mathrm{d}\boldsymbol{i}_g}{\mathrm{d}t} + \boldsymbol{v}_g, \tag{3.19}$$

where $R_t = R_{lc} + R_{lg} + R_g$ and $L_t = L_{lc} + L_{lg} + L_g$ are the total resistance and inductance, respectively. Mapping the variables to the dq-frame, it yields

$$\boldsymbol{v}_{\mathrm{conv},dq} = R_t \boldsymbol{i}_{g,dq} + L_t \frac{\mathrm{d}\boldsymbol{i}_{g,dq}}{\mathrm{d}t} + \omega_g L_t \begin{bmatrix} 0 & -1 \\ 1 & 0 \end{bmatrix} \boldsymbol{i}_{g,dq} + \boldsymbol{v}_{g,dq}\,. \tag{3.20}$$

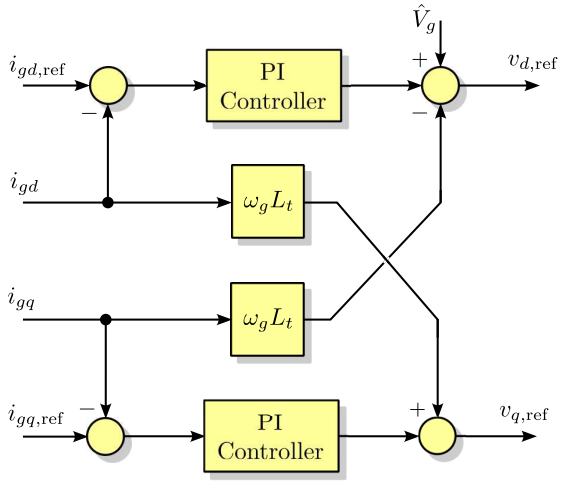

Figure 3.11: Current control loop of VOC.

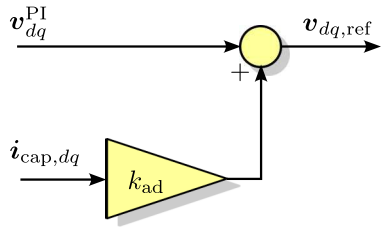

Figure 3.12: Block diagram of active damping with filter capacitor current feedback.

Following the same principle as FOC, a typical design of the current control loop in VOC is shown in Fig. 3.11, where two PI controllers are used to regulate the d- and q-component of the current to their references, respectively. Moreover, the cross-coupling and disturbance terms caused by the grid voltage are compensated with feed-forward terms.

3.3.2.3 Active Damping Methods

A proper damping solution needs to be implemented to address the resonance problem of LCL filters. A straightforward yet effective way to achieve active damping is feeding back the filter capacitor current with a proportional gain, as shown in Fig. 3.12, where $\boldsymbol{v}_{dq}^{\mathrm{PI}}$ indicates the output of the PI-based VOC shown above. For more details about active damping approaches, please see [37].

3.3.3 Grid Synchronization with Phase-Locked Loops (PLL)

The grid voltage vector's angle and magnitude are usually obtained by a phase-locked loop (PLL). The most commonly used technique for grid synchronization in a three-phase system is the so-called synchronous reference frame PLL (SRF-PLL) [38]. Fig. 3.13 shows the block diagram of SRF-PLL. The PI controller regulates the $v_{g,q}$ to zero. Thus, this dq-plane is oriented to align the grid voltage vector with the d-axis.

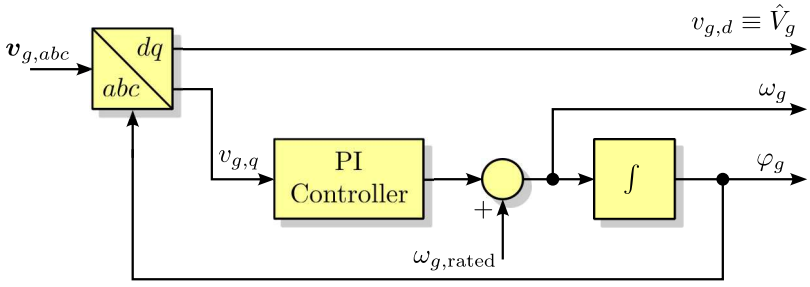

Figure 3.13: Block diagram of SRF-PLL.

3.4 Control of Grid Converters under Distorted and Unbalanced Grid Condition

In three-phase systems, the grid voltage typically contains harmonic distortions, mainly the (negative) 5th and the (positive) 7th. Those harmonic components need to be compensated by the controller so that the total harmonic distortion of the injected current at PCC will be kept within the limits. Moreover, the control algorithms of GTCs should ensure a robust and safe performance under abnormal grid conditions. For example, an important feature for grid-connected power converters is the so-called low-voltage ride-through (LVRT), which indicates the ability of power converters to stay connected to the grid throughout a (short) period of grid voltage drop.

3.4.1 PLL under distorted and unbalanced Grid Conditions

3.4.1.1 Distorted Grid Condition

Consider a grid voltage that mainly consists of the fundamental component $\boldsymbol{v}_{g^1}$, the 5th harmonic $\boldsymbol{v}_{g^{-5}}$ and the 7th harmonic $\boldsymbol{v}_{g^7}$. This voltage vector can be written as

$$\boldsymbol{v}_g = \boldsymbol{v}_{g^1} + \boldsymbol{v}_{g^{-5}} + \boldsymbol{v}_{g^7} = \hat{V}_{g^1} \begin{bmatrix} \cos(\omega_g t) \\ \sin(\omega_g t) \end{bmatrix} + \hat{V}_{g^{-5}} \begin{bmatrix} \cos(-5\omega_g t + \varphi_{-5}) \\ \sin(-5\omega_g t + \varphi_{-5}) \end{bmatrix} + \hat{V}_{g^7} \begin{bmatrix} \cos(7\omega_g t + \varphi_7) \\ \sin(7\omega_g t + \varphi_7) \end{bmatrix}. \tag{3.21}$$

Suppose the angular position of the fundamental voltage vector $\varphi_g = \omega_g t$ is detected by a PLL, then the voltage vector in (3.21) can be expressed in the dq reference frame as

$$\begin{aligned} \boldsymbol{v}_{g,dq} =& \boldsymbol{v}_{g^1,dq} + \boldsymbol{v}_{g^{-5},dq} + \boldsymbol{v}_{g^7,dq} = \hat{V}_{g^1} \begin{bmatrix} 1 \\ 0 \end{bmatrix} + \\ & \hat{V}_{g^{-5}} \cos(\varphi_{-5}) \begin{bmatrix} \cos(-6\omega_g t) \\ -\sin(-6\omega_g t) \end{bmatrix} + \hat{V}_{g^{-5}} \sin(\varphi_{-5}) \begin{bmatrix} \sin(-6\omega_g t) \\ \cos(-6\omega_g t) \end{bmatrix} + \\ & \hat{V}_{g^7} \cos(\varphi_7) \begin{bmatrix} \cos(6\omega_g t) \\ -\sin(6\omega_g t) \end{bmatrix} + \hat{V}_{g^7} \sin(\varphi_7) \begin{bmatrix} \sin(6\omega_g t) \\ \cos(6\omega_g t) \end{bmatrix}. \end{aligned} \tag{3.22}$$

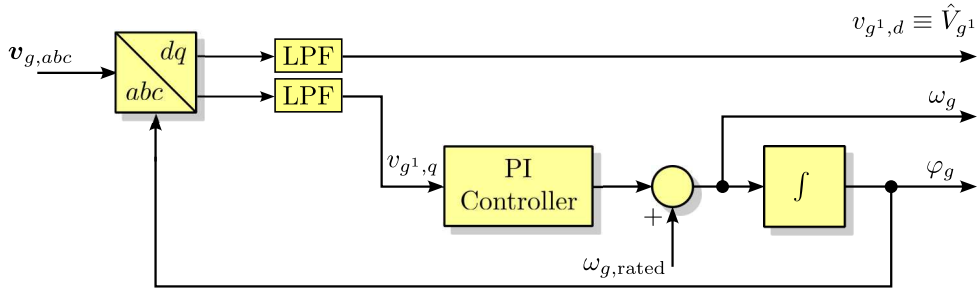

Figure 3.14: SRF-PLL with low-pass filters.

Since the amplitude of the fundamental component $\hat{V}_{g^1}$ is significantly larger than the amplitude of the harmonics i.e., $\hat{V}_{g^{-5}}$ and $\hat{V}_{g^7}$, a simple low-pass filter (LPF), such as

$$\text{LPF}(s) = \frac{\omega_f}{s + \omega_f} \quad \text{with} \quad \omega_f := \text{cut-off frequency}\,, \tag{3.23}$$

can filter out the AC components in (3.22) and extract the fundamental component, i.e., $\boldsymbol{v}_{g^1,dq} = [\hat{V}_{g^1}\ 0]^T$. Therefore, the SRF-PLL can be slightly modified by adding the LPFs, as shown in Fig. 3.14.

3.4.1.2 The Decoupling Network

Except for using the LPFs, another way to cancel out the AC components is using the decoupling Network [39]. Consider a voltage vector

$$\boldsymbol{v}_g = \boldsymbol{v}_{g^n} + \boldsymbol{v}_{g^m} = \hat{V}_{g^n} \begin{bmatrix} \cos\left(n\omega_g t + \varphi_n\right) \\ \sin\left(n\omega_g t + \varphi_n\right) \end{bmatrix} + \hat{V}_{g^m} \begin{bmatrix} \cos\left(m\omega_g t + \varphi_m\right) \\ \sin\left(m\omega_g t + \varphi_m\right) \end{bmatrix}, \tag{3.24}$$

which consists two components $\boldsymbol{v}_g^n$ and $\boldsymbol{v}_g^m$ rotating with $n\omega_g$ and $m\omega_g$, respectively. Note that n and m are integers that can be either positive or negative. Let dq^n and dq^m denote the rotating reference frames with the annular position $n\omega_g t$ and $m\omega_g t$, respectively, then the voltage vector can be expressed in these two rotating frames as

$$\boldsymbol{v}_{g,dq^n} = \boldsymbol{v}_{g^n,dq^n} + \boldsymbol{v}_{g^m,dq^n} = \hat{V}_{g^n} \begin{bmatrix} \cos\left(\varphi_n\right) \\ \sin\left(\varphi_n\right) \end{bmatrix} + \hat{V}_{g^m} \begin{bmatrix} \cos\left((m-n)\omega_g t + \varphi_m\right) \\ \sin\left((m-n)\omega_g t + \varphi_m\right) \end{bmatrix} \tag{3.25a}$$

$$\boldsymbol{v}_{g,dq^m} = \boldsymbol{v}_{g^n,dq^m} + \boldsymbol{v}_{g^m,dq^m} = \hat{V}_{g^n} \begin{bmatrix} \cos\left((n-m)\omega_g t + \varphi_n\right) \\ \sin\left((n-m)\omega_g t + \varphi_n\right) \end{bmatrix} + \hat{V}_{g^m} \begin{bmatrix} \cos\left(\varphi_m\right) \\ \sin\left(\varphi_m\right) \end{bmatrix}. \tag{3.25b}$$

As shown in (3.25), $\boldsymbol{v}_{g^n}$ appears as a constant term in the rotating dq^n frame, while the $\boldsymbol{v}_{g^m}$ appears as an alternating term with a frequency of $(m-n)\omega$. The decoupling network can effectively extract these two components. Indeed, (3.25) can be written as

$$\boldsymbol{v}_{g,dq^n} = \boldsymbol{v}_{g^n,dq^n} + \boldsymbol{P}((n-m)\varphi_g)\boldsymbol{v}_{g^m,dq^m} \tag{3.26a}$$

$$\boldsymbol{v}_{g,dq^m} = \boldsymbol{P}((m-n)\varphi_g)\boldsymbol{v}_{g^n,dq^n} + \boldsymbol{v}_{g^m,dq^m}\,, \tag{3.26b}$$

where the matrix $\boldsymbol{P}$ is the park transformation matrix and $\varphi_g = \omega_g t$ is the angular position of the fundamental voltage vector. An example of the decoupling network is shown in Fig. 3.15.

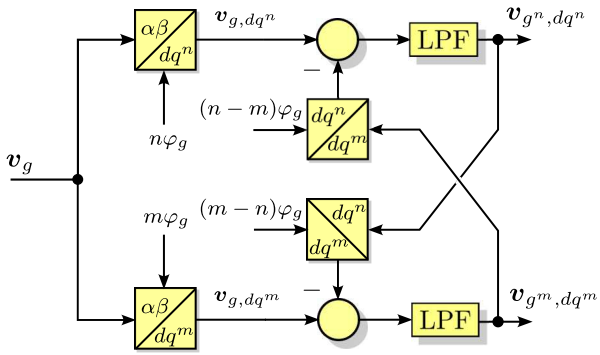

Figure 3.15: Decoupling network.

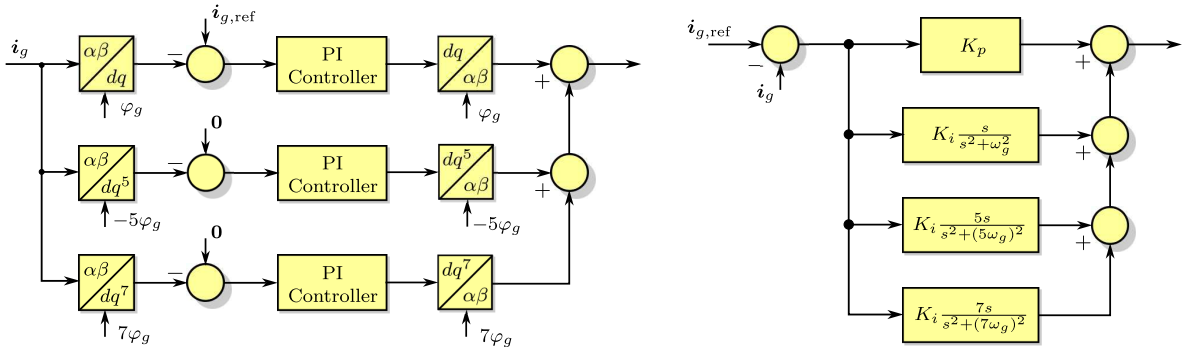

(a) PI. (b) PR.

Figure 3.16: Harmonic compensation with PI and PR controllers.

3.4.1.3 PLL for Unbalanced Grid

During grid faults, the three-phase grid voltage contains positive and negative sequence voltage vectors [40]. Considering only the fundamental wave, the grid voltage vector can be written as

$$\boldsymbol{v}_g = \boldsymbol{v}_{g^1} + \boldsymbol{v}_{g^{-1}} = \hat{V}_{g^1} \begin{bmatrix} \cos(\omega_g t) \\ \sin(\omega_g t) \end{bmatrix} + \hat{V}_{g^{-1}} \begin{bmatrix} \cos(-\omega_g t + \varphi_{-1}) \\ \sin(-\omega_g t + \varphi_{-1}) \end{bmatrix}. \tag{3.27}$$

The positive- and negative-sequence can be effectively extracted by using the decoupling network, as shown in Fig. 3.15, letting $n = 1$ and $m = -1$. Then, the positive-sequence component $\boldsymbol{v}_{g^1,dq^1}$ is used in the SPF-PLL to detect the angular position φ_g.

3.4.2 Harmonic Compensation using PI or PR Controllers

In the conventional linear control schemes, the grid harmonics can be compensated by additional PI controllers in the rotating reference frames synchronized with harmonic voltages, as shown in Fig. 3.16(a). Alternatively, the harmonic compensation can also be achieved in the stationary frame using PR controllers tuned to resonate at the harmonic frequencies, as shown in Fig. 3.16(b). Moreover, it is worth noting that PI controllers in a rotating dq-frame are actually equivalent to PR controllers in the stationary $\alpha\beta$-frame. A proof for that is presented in [41].

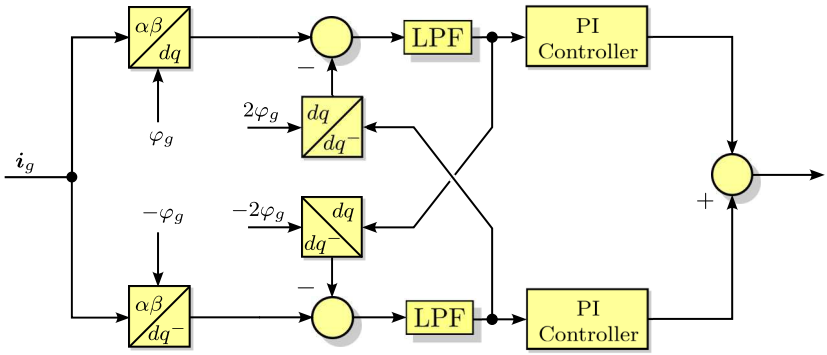

Figure 3.17: Decoupled double synchronous reference frame current controller.

3.4.3 Current Control under Grid Faults

During grid faults, unbalanced grid voltages—including both the positive- and negative-sequences—appear at the point of common coupling (PCC). An intuitive control scheme under such grid conditions is to use two control loops in two rotating reference frames synchronized with the positive- and negative-voltages, respectively [42], as shown in Fig. 3.17. By doing so, the grid current's positive- and negative-sequence components can be controlled, and the (instantaneous) active/reactive power at the PCC can be regulated. However, the current's positive- and negative-sequence components cannot be fully decoupled, especially during transients. A decoupling network with LPFs or notch filters (NFs) [42] can be used to attenuate the interaction between the two current components, but this significantly reduces the control bandwidth and even causes instability when the damping factor of the NFs or the cut-off frequencies of the LPFs is not properly tuned [41].

CHAPTER 4

Fixed Switching Frequency Direct Model Predictive Control for Drive Systems

A direct MPC scheme that operates the converter with a fixed switching frequency was initially proposed in [22] for variable speed drive systems with two-level three-phase voltage source inverters. This MPC method achieves fast transient responses that characterize direct controllers, as well as a similar or superior steady-state performance than that of modulator-based schemes. Later, this MPC method is refined and extended to GTCs with LCL filters [23] and three-level NPC inverters [27], demonstrating the high versatility of the developed algorithm along with its ability to handle MIMO systems with complex and nonlinear dynamics. This chapter presents the main principles and characteristics of this direct MPC method.

4.1 Direct MPC for Two-Level Inverters with Induction Machines

The first case study is a drive system consisting of a two-level inverter and an induction machine, as shown in Fig. 4.1.

4.1.1 Controller Model

The mathematical models of the two-level inverter and the IM are shown in Chapter 2. As discussed there, the model of the drive system in continuous-time state space representation is written as

$$\frac{\mathrm{d}\boldsymbol{x}_m(t)}{\mathrm{d}t} = \boldsymbol{F}_m \boldsymbol{x}_m(t) + \tilde{\boldsymbol{G}}_m \boldsymbol{K} \boldsymbol{u}_{abc}(t) \tag{4.1a}$$

$$\boldsymbol{y}_m(t) = \boldsymbol{C}_m \boldsymbol{x}_m(t)\,, \tag{4.1b}$$

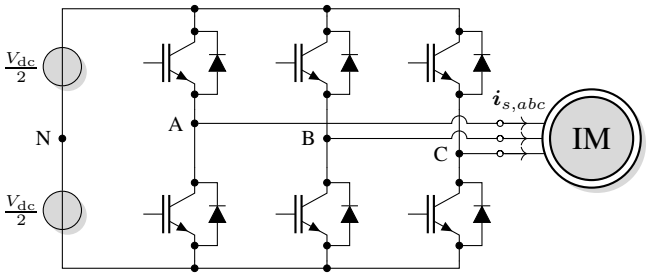

Figure 4.1: Two-level three-phase voltage source inverter driving an IM.

where the state vector is $\boldsymbol{x}_m = [i_{s\alpha}\ i_{s\beta}\ \psi_{r\alpha}\ \psi_{r\beta}]^T$, the three-phase switch position and the stator current are the system input and output, respectively, i.e., $\boldsymbol{u}_{abc} = [u_a\ u_b\ u_c]^T$ and $\boldsymbol{y} = [i_{s\alpha}\ i_{s\beta}]^T$. Moreover, matrices $\boldsymbol{F}_m$, $\tilde{\boldsymbol{G}}_m = \frac{v_{\rm dc}}{2}\boldsymbol{G}_m$, and $\boldsymbol{C}_m$ are the system, input, and output matrices, and they are defined in Chapter 2.
The discrete-time state-space model of the system can be derived by using forward Euler discretization as

$$\boldsymbol{x}_m(k+1) = \boldsymbol{A}_m\boldsymbol{x}_m(k) + \tilde{\boldsymbol{B}}_m\boldsymbol{K}\boldsymbol{u}_{abc}(k) \tag{4.2a}$$
$$\boldsymbol{y}_m(k) = \boldsymbol{C}_m\boldsymbol{x}_m(k)\,, \tag{4.2b}$$

with $k \in \mathbb{N}$, $\boldsymbol{A}_m = \boldsymbol{I} + \boldsymbol{F}_m T_s$, and $\tilde{\boldsymbol{B}}_m = \tilde{\boldsymbol{G}} T_s$, where $\boldsymbol{I}$ is the identity matrix of appropriate dimensions, and T_s the sampling interval.

4.1.2 Control Problem

The current references are generated by the outer loop, as introduced in Chapter 3, thus the MPC focuses on the inner current-loop control. The main objectives of the MPC controller are twofold, i.e., keeping the switching frequency of the converter constant and tracking the stator current with minimized ripple.
To achieve the first objective, each phase of the converter is allowed to switch once within the sampling intervals. Let t_i, $i \in \{1,2,3\}$, denote the switching instants that are placed in an ascending order within one sampling interval T_s, i.e., $0 \leq t_1 \leq t_2 \leq t_3 \leq T_s$. Thus, each sampling interval is divided into four sub-intervals $[0, t_1)$, $[t_1, t_2)$, $[t_2, t_3)$ and $[t_3, T_s)$, which are the application times of four switch positions. Specifically, at the beginning of the current sampling $t_0 \equiv 0$, and until t_1, the last switch position applied in the previous T_s is applied, i.e., $\boldsymbol{u}_{abc}(t_0) = \boldsymbol{u}_{abc}(t_0^-)$. At time instant t_1, a switching transition is performed in one of the three phases, implying that the switch position $\boldsymbol{u}_{abc}(t_1)$ is applied. Following, at time instant t_2, the switch position $\boldsymbol{u}_{abc}(t_2)$ is applied such that one of the two thus far inactive phases is switched. Finally, the only inactive phase left is forced to switch at time instant t_3 by applying switch position $\boldsymbol{u}_{abc}(t_3)$. As can be understood, by following this principle, the three phases of the system can switch in six possible combinations, see the left-hand side of Table 4.1. For example, phase a may switch first, followed by consecutive changes in phases b and c, or vice versa, etc.
The above concept can be extended to longer prediction horizons, which are adopted here due to the improvements they bring in the steady-state performance [43]. However, as shown in [23],

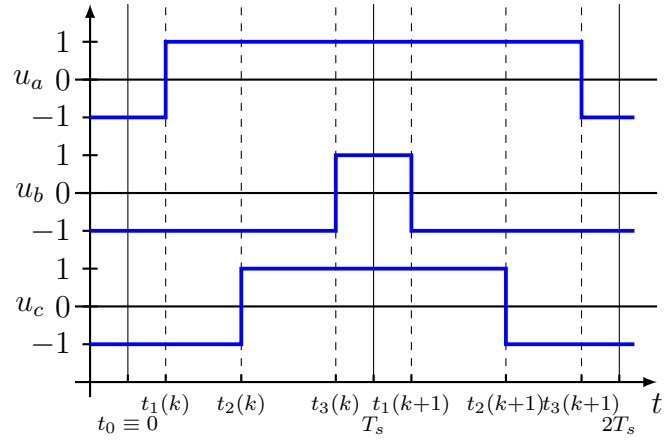

(a) Three-phase switch position.

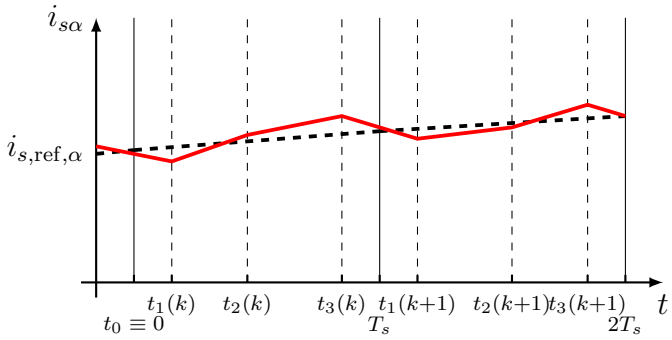

(b) Stator current (α-component).

Figure 4.2: Example of the evolution of $i_{s\alpha}$ over two sampling intervals by applying the depicted switching sequence.

to keep the number of possible switching sequences constant and equal to six—instead of increasing it exponentially with the horizon steps N_p, i.e., 6^{N_p}—the switching sequences are mirrored with respect to the discrete time steps in a consecutive fashion, similar to, e.g., the SVM switching pattern [17]. Considering that a two-step horizon ($N_p = 2$) is implemented in this work, this means that the switching sequence in the second prediction interval mirrors that of the first prediction interval with respect to T_s, as illustrated in Fig. 4.2(a). Table 4.1 summarizes all possible switching sequences over a two-step prediction, and an example of the switching sequence number 2 is shown in Fig. 4.2(a).

To describe the above, the vector of switching time instants $\boldsymbol{t}$ and the vector of switch positions (i.e., the switching sequence) $\boldsymbol{U}$ are introduced. These are defined as

$$\boldsymbol{t} = \begin{bmatrix} \boldsymbol{t}^T(k) & \boldsymbol{t}^T(k+1) \end{bmatrix}^T \tag{4.3a}$$

$$\boldsymbol{U} = \begin{bmatrix} \boldsymbol{U}^T(k) & \boldsymbol{U}^T(k+1) \end{bmatrix}^T, \tag{4.3b}$$

Table 4.1: Possible switching sequences for a two-step horizon.

Number of sequence	Phase with the switching transition					
	1^{st} sampling interval			2^{nd} sampling interval		
	First	Second	Third	First	Second	Third
1	a	b	c	c	b	a
2	a	c	b	b	c	a
3	b	a	c	c	a	b
4	b	c	a	a	c	b
5	c	a	b	b	a	c
6	c	b	a	a	b	c

where

$$\boldsymbol{t}(\ell) = \begin{bmatrix} t_1(\ell) & t_2(\ell) & t_3(\ell) \end{bmatrix}^T \tag{4.4a}$$

$$\boldsymbol{U}(\ell) = \begin{bmatrix} \boldsymbol{u}_{abc}^T(t_0(\ell))\, \boldsymbol{u}_{abc}^T(t_1(\ell))\, \boldsymbol{u}_{abc}^T(t_2(\ell))\, \boldsymbol{u}_{abc}^T(t_3(\ell)) \end{bmatrix}^T. \tag{4.4b}$$

with $\ell \in \{k, k+1\}$. It is important to point out that, as explained above, it is implied that $\boldsymbol{U}(k+1) = [\boldsymbol{u}_{abc}^T(t_3(k))\ \boldsymbol{u}_{abc}^T(t_2(k))\ \boldsymbol{u}_{abc}^T(t_1(k))\ \boldsymbol{u}_{abc}^T(t_0(k))]^T$, i.e., $\boldsymbol{u}_{abc}(t_0(k+1)) = \boldsymbol{u}_{abc}(t_3(k))$, $\boldsymbol{u}_{abc}(t_1(k+1)) = \boldsymbol{u}_{abc}(t_2(k))$, $\boldsymbol{u}_{abc}(t_2(k+1)) = \boldsymbol{u}_{abc}(t_1(k))$, and $\boldsymbol{u}_{abc}(t_3(k+1)) = \boldsymbol{u}_{abc}(t_0(k))$. Note, however, that the switching times may be asymmetric, thus $t_1(k)$ is not necessarily equal to $2T_s - t_3(k+1)$, etc.

The second control objective is the minimization of the (approximate) rms stator current error, since this corresponds to the minimization of the stator current total harmonic distortion (THD) [44, Appendix A]. As explained in [22] and [23], this goal can be mapped into the objective function

$$J = \sum_{\ell=k}^{k+1} \left(\sum_{i=1}^{3} \|\boldsymbol{i}_{s,\text{ref}}(t_i(\ell)) - \boldsymbol{i}_s(t_i(\ell))\|_2^2 + \left\|\boldsymbol{\Lambda}\big(\boldsymbol{i}_{s,\text{ref}}(T_s(\ell)) - \boldsymbol{i}_s(T_s(\ell))\big)\right\|_2^2 \right), \tag{4.5}$$

where the current tracking error is penalized at the switching instants and at the discrete time steps. Note that the diagonal, positive definite matrix $\boldsymbol{\Lambda} \succ 0 \in \mathbb{R}^{2\times 2}$ is introduced to penalize more heavily the tracking error at the discrete time steps. As explained in [23, Section III], by doing so, symmetry in the applied switching sequences is enforced, which enables the elimination of undesired low-frequency harmonics.

4.1.3 Control Method

To find the optimal switching time instants $\boldsymbol{t}^*$, the current error, as quantified by (4.5), needs to be computed for all six possible switching sequences $\boldsymbol{U}$, as mentioned in Section 4.1.2. To do so, the evolution of the stator current $\boldsymbol{i}_s$ within all the subintervals of the prediction horizon

needs to be computed for each $\boldsymbol{U}$. Given that the sampling interval T_s is much smaller than the fundamental period T_1, i.e., $T_s \ll T_1$, it is assumed that the derivative of the stator current when applying a switching transition is constant within T_s. Such an assumption implies that the stator current trajectories within the subintervals of the horizon can be described by their corresponding gradients, i.e.,

$$\boldsymbol{m}(t_i(\ell)) = \frac{\mathrm{d}\boldsymbol{i}_s(t_i(\ell))}{\mathrm{d}t} = \boldsymbol{C}_m(\boldsymbol{F}_m\boldsymbol{x}_m(t_0(k)) + \tilde{\boldsymbol{G}}_m\boldsymbol{K}\boldsymbol{u}_{abc}(t_i(\ell)))\,, \tag{4.6}$$

where $i \in \{0,1,2,3\}$ and $\ell = k, k+1$. Note that because of the assumption of constant gradients within T_s, (4.6) computes the gradients at the switching instants $t_1(\ell)$, $t_2(\ell)$, and $t_3(\ell)$ based on the measured/estimated state, i.e., $\boldsymbol{x}(t_0(k))$.
Utilizing the gradients provided by (4.6), the stator current at the switching instants and discrete time steps can be calculated as

$$\boldsymbol{i}_s(t_i(\ell)) = \boldsymbol{i}_s(t_{i-1}(\ell)) + \boldsymbol{m}(t_{i-1}(\ell))(t_i(\ell) - t_{i-1}(\ell))\,, \tag{4.7}$$

with $i \in \{1,2,3,4\}$ and $t_4 = T_s$.
On the same principle, the current reference is assumed to evolve in a piecewise linear fashion within the horizon, with a constant gradient for each prediction step, given by

$$\boldsymbol{m}_{\mathrm{ref}}(\ell) = \frac{\boldsymbol{i}_{s,\mathrm{ref}}(\ell+1) - \boldsymbol{i}_{s,\mathrm{ref}}(\ell)}{T_s}\,. \tag{4.8}$$

Hence, the current reference over the horizon is

$$\boldsymbol{i}_{s,\mathrm{ref}}(t) = \boldsymbol{i}_{s,\mathrm{ref}}(\ell) + \boldsymbol{m}_{\mathrm{ref}}(\ell)\,t\,. \tag{4.9}$$

An example of the stator current evolution and the corresponding reference on the α-axis is shown in Fig. 4.2(b).
Finally, based on expressions (4.6) to (4.9), and after some algebraic manipulations, function (4.5) can be written in vector form as

$$J = \|\boldsymbol{r} - \boldsymbol{M}\boldsymbol{t}\|_2^2\,, \tag{4.10}$$

where the vector $\boldsymbol{r} \in \mathbb{R}^{8N_p}$ and matrix $\boldsymbol{M} \in \mathbb{R}^{8N_p \times 3N_p}$, with $N_p = 2$, are

$$\boldsymbol{r} = \begin{bmatrix} \boldsymbol{i}_{s,\mathrm{ref}}(t_0) - \boldsymbol{i}_s(t_0) \\ \boldsymbol{i}_{s,\mathrm{ref}}(t_0) - \boldsymbol{i}_s(t_0) \\ \boldsymbol{i}_{s,\mathrm{ref}}(t_0) - \boldsymbol{i}_s(t_0) \\ \Lambda(\boldsymbol{i}_{s,\mathrm{ref}}(T_s) - \boldsymbol{i}_s(t_0) - \boldsymbol{m}(t_3(k))T_s) \\ \boldsymbol{i}_{s,\mathrm{ref}}(T_s) - \boldsymbol{i}_s(t_0) \\ \boldsymbol{i}_{s,\mathrm{ref}}(T_s) - \boldsymbol{i}_s(t_0) \\ \boldsymbol{i}_{s,\mathrm{ref}}(T_s) - \boldsymbol{i}_s(t_0) \\ \Lambda(\boldsymbol{i}_{s,\mathrm{ref}}(2T_s) - \boldsymbol{i}_s(t_0) - \boldsymbol{m}(t_3(k+1))2T_s) \end{bmatrix} \tag{4.11}$$

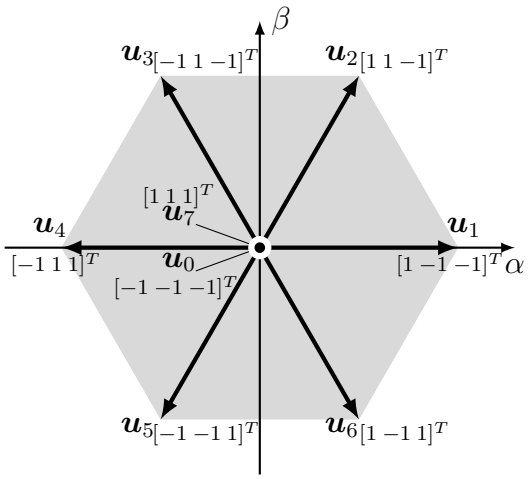

Figure 4.3: Two-level inverter switch positions in the stationary ($\alpha\beta$) plane.

and

$$\boldsymbol{M} = \begin{bmatrix} \boldsymbol{m}_{t_0} & \mathbf{0}_2 & \mathbf{0}_2 & \mathbf{0}_2 & \mathbf{0}_2 & \mathbf{0}_2 \\ \boldsymbol{m}_0 & \boldsymbol{m}_{t_1} & \mathbf{0}_2 & \mathbf{0}_2 & \mathbf{0}_2 & \mathbf{0}_2 \\ \boldsymbol{m}_0 & \boldsymbol{m}_1 & \boldsymbol{m}_{t_2} & \mathbf{0}_2 & \mathbf{0}_2 & \mathbf{0}_2 \\ \boldsymbol{\Lambda m}_0 & \boldsymbol{\Lambda m}_1 & \boldsymbol{\Lambda m}_2 & \mathbf{0}_2 & \mathbf{0}_2 & \mathbf{0}_2 \\ \boldsymbol{m}_0 & \boldsymbol{m}_1 & \boldsymbol{m}_2 & \boldsymbol{m}_{\bar{t}_0} & \mathbf{0}_2 & \mathbf{0}_2 \\ \boldsymbol{m}_0 & \boldsymbol{m}_1 & \boldsymbol{m}_2 & \boldsymbol{m}_{\bar{0}} & \boldsymbol{m}_{\bar{t}_1} & \mathbf{0}_2 \\ \boldsymbol{m}_0 & \boldsymbol{m}_1 & \boldsymbol{m}_2 & \boldsymbol{m}_{\bar{0}} & \boldsymbol{m}_{\bar{1}} & \boldsymbol{m}_{\bar{t}_2} \\ \boldsymbol{\Lambda m}_0 & \boldsymbol{\Lambda m}_1 & \boldsymbol{\Lambda m}_2 & \boldsymbol{\Lambda m}_{\bar{0}} & \boldsymbol{\Lambda m}_{\bar{1}} & \boldsymbol{\Lambda m}_{\bar{2}} \end{bmatrix} \tag{4.12}$$

with

$$\begin{aligned} \boldsymbol{m}_{t_i} &= \boldsymbol{m}(t_i(k)) - \boldsymbol{m}_{\mathrm{ref}}(k) \\ \boldsymbol{m}_{\bar{t}_i} &= \boldsymbol{m}(t_i(k+1)) - \boldsymbol{m}_{\mathrm{ref}}(k+1) \\ \boldsymbol{m}_i &= \boldsymbol{m}(t_i(k)) - \boldsymbol{m}(t_{i+1}(k)) \\ \boldsymbol{m}_{\bar{i}} &= \boldsymbol{m}(t_i(k+1)) - \boldsymbol{m}(t_{i+1}(k+1)) \end{aligned}$$

where $i \in \{0,\ 1,\ 2\}$ and $t_0(k+1) = T_s$.

4.1.4 Control Algorithm

Taking into account the control principles developed in Sections 4.1.2 and 4.1.3, the direct MPC algorithm is summarized in the following.
In a first step, the *seven* unique stator current gradients are computed based on the measured/estimated state vector $\boldsymbol{x}(t_0)$ and the possible *eight* switch positions $\boldsymbol{u}_{abc}$, i.e.,

$$\boldsymbol{m}_w = \boldsymbol{C}_m(\boldsymbol{F}_m \boldsymbol{x}_m(t_0) + \tilde{\boldsymbol{G}}_m \boldsymbol{u}_w)\,, \tag{4.13}$$

Algorithm 1 Fixed Switching Frequency Direct MPC

Given $\boldsymbol{u}_{abc}(t_0^-)$, $\boldsymbol{i}_{s,\mathrm{ref}}(t_0)$ and $\boldsymbol{x}_m(t_0)$
1: Compute the corresponding gradient vectors $\boldsymbol{m}_w$, $w \in \{0, 1, \ldots, 6\}$
2: Enumerate the possible switching sequences $\boldsymbol{U}_z$, $z \in \{1, 2, \ldots, 6\}$, based on $\boldsymbol{u}_{abc}(t_0^-)$
3: For each $\boldsymbol{U}_z$:
Detect if $\boldsymbol{U}_z$ is unsuited;
If not, solve the QP (4.14). This yields $\boldsymbol{t}_z$ and J_z.
4: Solve optimization problem (4.15). This yields $\boldsymbol{t}^*$ and $\boldsymbol{U}^*$.
Return $\boldsymbol{t}^*(k)$ and $\boldsymbol{U}^*(k)$.

where $w \in \{0, 1, \ldots, 6\}$. Note that in (4.13), $\boldsymbol{u}_w = \boldsymbol{K}\boldsymbol{u}_{abc,w}$ stands for the unique voltage vectors in the $\alpha\beta$-plane (six active and one zero vector), see Fig. 4.3, where $\boldsymbol{u}_j$, $j \in \{1, 2, \ldots, 6\}$, are the active vectors, and $\boldsymbol{u}_0/\boldsymbol{u}_7$ the zero vector.

Subsequently, the controller enumerates the six possible switching sequences $\boldsymbol{U}_z$, $z \in \{1, 2, \ldots, 6\}$, shown in Table 4.1. For each one of them, an optimization problem of the form

$$\begin{aligned} \underset{\boldsymbol{t} \in \mathbb{R}^6}{\text{minimize}} \quad & \|\boldsymbol{r} - \boldsymbol{M}\boldsymbol{t}\|_2^2 \\ \text{subject to} \quad & 0 \leq t_1(k) \leq t_2(k) \leq t_3(k) \leq T_s \\ & \leq t_1(k+1) \leq t_2(k+1) \leq t_3(k+1) \leq 2T_s \end{aligned} \tag{4.14}$$

is formulated. According to [22] and [23], the QP (4.14) has to be solved six times—once for each $\boldsymbol{U}_z$—based on an off-the-self QP solver [24, Section IV] to yield $\boldsymbol{t}_z$ and the associated cost J_z. However, a more computational efficient method is solving (4.14) by the QP solver proposed in Section 5.1. Moreover, as explained in that section, the developed solver can detect unsuited $\boldsymbol{U}_z$ with a simple one-step projection method, meaning that at most two QPs (4.14) need to be solved in real time. As a result, the computational burden of the direct MPC algorithm is kept modest, thus facilitating its real-time implementation.

In a last step, the pair of switching sequence and time instants that is globally optimal, i.e., $\{\boldsymbol{U}^*, \boldsymbol{t}^*\}$, is chosen by solving the following trivial optimization problem

$$\underset{z \in \{1,2,\ldots,6\}}{\text{minimize}} \quad J_z\,. \tag{4.15}$$

According to the receding horizon policy [3], only the switch positions that correspond to the first T_s are applied to the converter at the corresponding time instants, i.e.,

$$\begin{aligned} \boldsymbol{U}^*(k) &= \begin{bmatrix} \boldsymbol{u}_{abc}^{*T}(t_0(k)) \boldsymbol{u}_{abc}^{*T}(t_1^*(k)) \boldsymbol{u}_{abc}^{*T}(t_2^*(k)) \boldsymbol{u}_{abc}^{*T}(t_3^*(k)) \end{bmatrix}^T \\ \boldsymbol{t}^*(k) &= \begin{bmatrix} t_1^*(k) & t_2^*(k) & t_3^*(k) \end{bmatrix}^T . \end{aligned}$$

The block diagram of the proposed direct MPC scheme is shown in Fig. 4.4, and the pseudocode is provided in Algorithm 1.

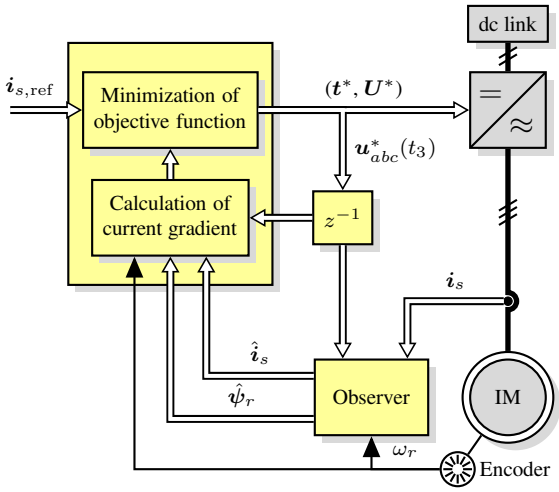

Figure 4.4: Fixed switching frequency direct MPC for a two-level three-phase voltage source inverter driving an IM.

4.2 Direct MPC for Three-Level NPC Inverters with Induction Machines

The second case study is a drive system with a 3L-NPC voltage source inverter driving an IM, as shown in Fig. 4.5.

4.2.1 Controller Model

The model of the 3L-NPC is shown in Chapter 2. As discussed there, each phase x, with $x \in \{a, b, c\}$, has three switch positions, i.e., $u_x \in \mathcal{U}_{3L} = \{-1,\ 0,\ 1\}$. And the three-phase output voltage $\boldsymbol{v}_{abc} = [v_a\ v_b\ v_c]^T$ can be calculated from the three-phase switch position $\boldsymbol{u}_{abc} = [u_a\ u_b\ u_c]^T$ as

$$\boldsymbol{v}_{abc} = \frac{v_{\mathrm{dc}}}{2}\boldsymbol{u}_{abc} - v_n|\boldsymbol{u}_{abc}|\,, \tag{4.16}$$

where $|\boldsymbol{u}_{abc}| = [|u_a|\ |u_b|\ |u_c|]^T$ is the component-wise absolute value of $\boldsymbol{u}_{abc}$ and $v_n = \frac{1}{2}(v_{\mathrm{dc,lo}} - v_{\mathrm{dc,up}})$ is the neutral point potential. The dynamic of the neutral potential v_n can be described as

$$\frac{\mathrm{d}v_n}{\mathrm{d}t} = \frac{1}{2C_{\mathrm{dc}}}|\boldsymbol{u}_{abc}|^T\boldsymbol{i}_{abc}. \tag{4.17}$$

Combining the IM state space model (2.16) with (4.17) and (4.16) yields that state-space representation of the drive system, i.e.,

$$\frac{\mathrm{d}\boldsymbol{x}(t)}{\mathrm{d}t} = \boldsymbol{F}(\boldsymbol{u}_{abc}(t))\boldsymbol{x}(t) + \boldsymbol{G}\boldsymbol{u}_{abc}(t) \tag{4.18a}$$

$$\boldsymbol{y}(t) = \boldsymbol{C}\boldsymbol{x}(t)\,, \tag{4.18b}$$

where the state vector is $\boldsymbol{x} = [\boldsymbol{x}_m^T\ v_n]^T$, the three-phase switch position $\boldsymbol{u}_{abc}$ is the system input, and the system output consists of the stator current and the NP potential, i.e., $\boldsymbol{y} = [\boldsymbol{y}_m^T\ v_n]^T$.

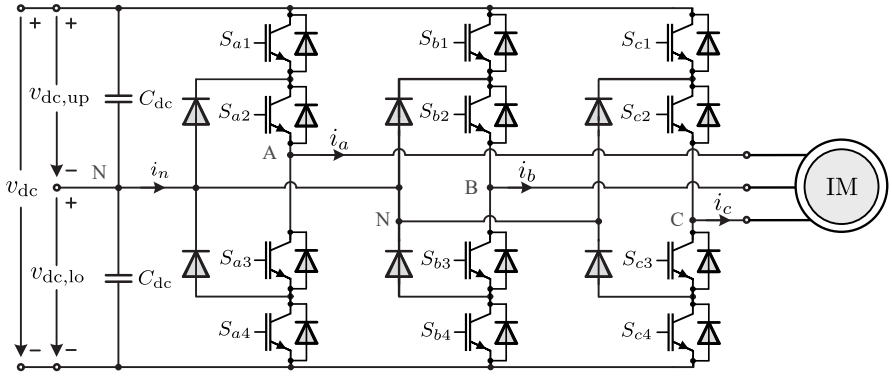

Figure 4.5: Three-level three-phase neutral point clamped (NPC) voltage source inverter driving an induction motor (IM).

The system matrix $\boldsymbol{F}(\boldsymbol{u}_{abc}(t))$, the input matrix $\boldsymbol{G}$, and the output matrix $\boldsymbol{C}$ are

$$\boldsymbol{F}(\boldsymbol{u}_{abc}(t)) = \begin{bmatrix} \boldsymbol{F}_m & \begin{bmatrix} -\frac{X_r}{D}\boldsymbol{K}|\boldsymbol{u}_{abc}| \\ \boldsymbol{0}_{2\times 1} \end{bmatrix} \\ \begin{bmatrix} \frac{1}{2X_{\mathrm{dc}}}|\boldsymbol{u}_{abc}|^T\boldsymbol{K}^{-1} & \boldsymbol{0}_{1\times 2} \end{bmatrix} & 0 \end{bmatrix}, \tag{4.19}$$

and

$$\boldsymbol{G} = \frac{v_{\mathrm{dc}}}{2}\boldsymbol{G}_m\boldsymbol{K},\ \boldsymbol{C} = \begin{bmatrix} \boldsymbol{C}_m & \boldsymbol{0}_{2\times 1} \\ \boldsymbol{0}_{1\times 4} & 1 \end{bmatrix}. \tag{4.20}$$

Finally, by using forward Euler discretization,[1] the discrete-time state-space model of the system is derived as

$$\boldsymbol{x}(k+1) = \boldsymbol{A}\boldsymbol{x}(k) + \boldsymbol{B}\boldsymbol{u}_{abc}(k) \tag{4.21a}$$

$$\boldsymbol{y}(k) = \boldsymbol{C}\boldsymbol{x}(k)\,, \tag{4.21b}$$

with $k \in \mathbb{N}$, $\boldsymbol{A} = \boldsymbol{I} + \boldsymbol{F}(\boldsymbol{u}_{abc}(t))T_s$, and $\boldsymbol{B} = \boldsymbol{G}T_s$, where $\boldsymbol{I}$ is the identity matrix of appropriate dimensions, and T_s the sampling interval.

4.2.2 Objective Function

The control objectives are threefold. First, the stator current should be regulated along its reference with as little distortion as possible and as quickly as possible so that short settling times are achieved. Second, the NP potential of the 3L-NPC inverter should be balanced under all operating conditions. Finally, operation at a constant switching frequency is desired such that the losses produced in the inverter are constant.

Following the same principle explained in the Section 4.1, The first two objectives can be achieved by minimizing the objective function

$$\begin{aligned} J = \sum_{i=1}^{3} &\|\boldsymbol{y}_{\mathrm{ref}}(t_i(k)) - \boldsymbol{y}(t_i(k))\|_Q^2 \\ &+ \left\|\boldsymbol{\Lambda}\big(\boldsymbol{y}_{\mathrm{ref}}(T_s(k)) - \boldsymbol{y}(T_s(k))\big)\right\|_Q^2\,, \end{aligned} \tag{4.22}$$

[1] When a higher accuracy is required, e.g., at low sampling frequencies, the exact discretization can be used for the IM state-space model (2.16), see [3, Section 7.2.3] for more details.

where $\boldsymbol{y}_{\text{ref}} = [i_{s\alpha,\text{ref}} \;\; i_{s\beta,\text{ref}} \;\; v_{n,\text{ref}}]^T$ is the output reference vector, and $\boldsymbol{Q} \succ 0 \in \mathbb{R}^{3\times3}$ the penalty matrix. Here, the penalty matrix is defined as $\boldsymbol{Q} = \text{diag}(1,\ 1,\ \lambda_n)$ with $\lambda_n > 0$ being the weighting factor that adjusts the priority of the NP potential balancing. Moreover, the diagonal positive definite matrix $\boldsymbol{\Lambda} \succ 0$ is introduced to more heavily penalize the output error at the end of the sampling interval. Note that $\boldsymbol{y}_{\text{ref}}(T_s(k)) \equiv \boldsymbol{y}_{\text{ref}}(k+1)$ and $\boldsymbol{y}(T_s(k)) \equiv \boldsymbol{y}(k+1)$. By doing so, the output error at the sampling instants is always kept close to zero, which effectively eliminates the undesired low-frequency harmonics [23]. Note that the number of prediction horizon is chosen as $N_p = 1$ for a lower computational burden.
Similarly, to ensure a fixed switching frequency, each phase leg is forced to switch exactly once per sampling interval T_s. And the vectors of switching time instants $\boldsymbol{t}$ and switch positions $\boldsymbol{U}$ are introduced as

$$\begin{aligned} \boldsymbol{t} &= [t_1 \;\; t_2 \;\; t_3]^T \\ \boldsymbol{U} &= [\boldsymbol{u}_{abc}^T(t_0) \;\; \boldsymbol{u}_{abc}^T(t_1) \;\; \boldsymbol{u}_{abc}^T(t_2) \;\; \boldsymbol{u}_{abc}^T(t_3)]^T . \end{aligned} \tag{4.23}$$

where

$$0 \le t_1 \le t_2 \le t_3 \le T_s \, . \tag{4.24}$$

Given that the sampling interval T_s is much smaller than the fundamental period T_1, i.e., $T_s \ll T_1$, the corresponding output gradients, given by

$$\begin{aligned} \boldsymbol{m}(t_i(k)) &= \frac{\boldsymbol{y}(k+1) - \boldsymbol{y}(k)}{T_s} \\ &= \frac{\boldsymbol{C}((\boldsymbol{A} - \boldsymbol{I})\boldsymbol{x}(k) + \boldsymbol{B}\boldsymbol{u}_{abc}(t_i(k)))}{T_s} . \end{aligned} \tag{4.25}$$

can be utilized to predict the evolution of the system output. This yields

$$\boldsymbol{y}(t_{i+1}(k)) = \boldsymbol{y}(t_i(k)) + \boldsymbol{m}(t_i(k))(t_{i+1}(k) - t_i(k)) \, , \tag{4.26}$$

with $i \in \{0, 1, 2, 3\}$ and $t_4 = T_s$.
In the same manner, the output reference is assumed to evolve linearly within one sampling interval, i.e., it evolves with the gradient

$$\boldsymbol{m}_{\text{ref}}(k) = \frac{\boldsymbol{y}_{\text{ref}}(k+1) - \boldsymbol{y}_{\text{ref}}(k)}{T_s} \, , \tag{4.27}$$

Hence, the output reference over this sampling interval is

$$\boldsymbol{y}_{\text{ref}}(t) = \boldsymbol{y}_{\text{ref}}(k) + \boldsymbol{m}_{\text{ref}}(k)\, t \, . \tag{4.28}$$

An example of the evolution of the stator current for a given switching sequence (the depicted sequence is $a \to c \to b$) and its reference are shown in Fig. 4.6. Note that the current reference is generated by an outer loop, and the reference of the NP potential $v_{n,\text{ref}}$ is zero.
Based on the above, the objective function can be written in the following vector form

$$J = \|\boldsymbol{r} - \boldsymbol{M}\boldsymbol{t}\|_{\tilde{\boldsymbol{Q}}}^2 \, , \tag{4.29}$$

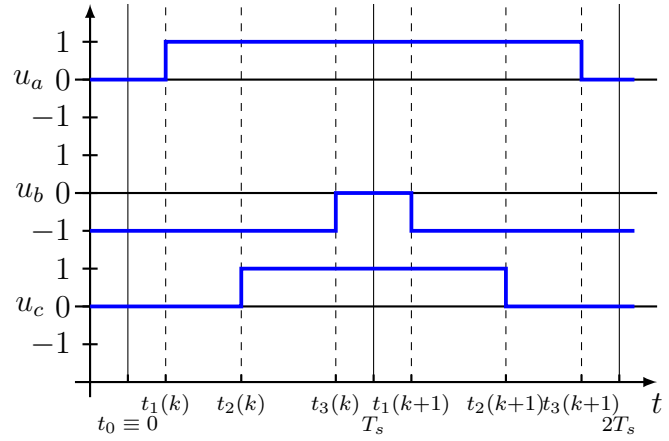

(a) Three-phase switching sequence.

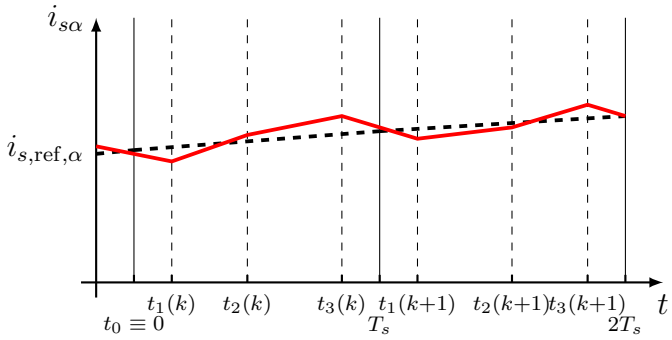

(b) Stator current (α-component).

Figure 4.6: Example of one switching sequence and the corresponding stator current.

where $\tilde{\boldsymbol{Q}} = \mathrm{diag}(\boldsymbol{Q}, \ldots, \boldsymbol{Q})$, while the vector $\boldsymbol{r} \in \mathbb{R}^{12}$ and the matrix $\boldsymbol{M} \in \mathbb{R}^{12\times 3}$ are

$$\boldsymbol{r} = \begin{bmatrix} \boldsymbol{y}_{s,\mathrm{ref}}(t_0) - \boldsymbol{y}_s(t_0) \\ \boldsymbol{y}_{s,\mathrm{ref}}(t_0) - \boldsymbol{y}_s(t_0) \\ \boldsymbol{y}_{s,\mathrm{ref}}(t_0) - \boldsymbol{y}_s(t_0) \\ \boldsymbol{\Lambda}(\boldsymbol{y}_{s,\mathrm{ref}}(T_s) - \boldsymbol{y}_s(t_0) - \boldsymbol{m}(t_3)T_s) \end{bmatrix} \tag{4.30}$$

and

$$\boldsymbol{M} = \begin{bmatrix} \boldsymbol{m}_{t_0} & \boldsymbol{0}_3 & \boldsymbol{0}_3 \\ \boldsymbol{m}_0 & \boldsymbol{m}_{t_1} & \boldsymbol{0}_3 \\ \boldsymbol{m}_0 & \boldsymbol{m}_1 & \boldsymbol{m}_{t_2} \\ \boldsymbol{\Lambda}\boldsymbol{m}_0 & \boldsymbol{\Lambda}\boldsymbol{m}_1 & \boldsymbol{\Lambda}\boldsymbol{m}_2 \end{bmatrix} \tag{4.31}$$

with

$$\boldsymbol{m}_{t_i} = \boldsymbol{m}(t_i) - \boldsymbol{m}_{\mathrm{ref}} \tag{4.32}$$

$$\boldsymbol{m}_i = \boldsymbol{m}(t_i) - \boldsymbol{m}(t_{i+1}) \tag{4.33}$$

where $i \in \{0,\ 1,\ 2\}$.

Table 4.2: Single-phase switching transitions and initial switch position.

Polarity of $u^*_{\mathrm{db},x}$	Sign of Δu_x	Switching transition for u_x	Initial switch position $u_x(t_0)$
≥ 0	$+$	$0 \rightarrow 1$	0
≥ 0	$-$	$1 \rightarrow 0$	1
< 0	$+$	$-1 \rightarrow 0$	-1
< 0	$-$	$0 \rightarrow -1$	0

4.2.3 Selection of Candidate Switching Sequences

Even though there are only six chronological orders with which the three phases can switch, as shown in Table 4.1, the possible combinations of switch positions for a 3L-NPC converter are 48.[2] This implies that an equal number of optimization problems (one for each combination) is required to be solved in real time. Such a task, however, is impossible with the available computational resources. Hence, a method to reduce the possible combinations needs to be adopted. To this end, a strategy to define the feasible switch positions within each T_s as well as the initial switch position is introduced, as explained in the following.

Before assessing the possible switching sequences (see Table 4.1), the initial switch position at each sampling interval i.e., $\boldsymbol{u}_{abc}(t_0)$, needs to be determined. To do so, the type of switching transition, defined as $\Delta\boldsymbol{u}_{abc}(k) = \boldsymbol{u}_{abc}(t_3) - \boldsymbol{u}_{abc}(t_0) \in \{-1, 1\}^3$, needs to be examined.[3] In line with the switching pattern of CB-PWM or SVM, the sign of each single-phase transition $\Delta u_x(k)$, $x \in \{a, b, c\}$, is the same for all three phases in one sampling interval T_s, and it alternates between consecutive T_s. For example, if the sign of $\Delta\boldsymbol{u}_{abc}(k)$ is set to be positive in the first T_s, then it is negative in the next T_s, again positive in the third T_s, and so on.

Following, to unequivocally determine $\boldsymbol{u}_{abc}(t_0)$, the deadbeat solution is employed. This is done by considering *only* the IM dynamics [45]. In doing so, the deadbeat solution is given by[4]

$$\boldsymbol{v}_{\mathrm{db},abc} = \boldsymbol{K}^{-1}\big((\boldsymbol{C}_m\boldsymbol{B}_m)^{-1}(\boldsymbol{y}_{m,\mathrm{ref}}(k+1) - \boldsymbol{C}_m\boldsymbol{A}_m\boldsymbol{x}_m(k)\big)\,. \tag{4.34}$$

The sign of each entry of $\boldsymbol{v}_{\mathrm{db},abc}$ determines the feasible switch positions. Hence, the combination of the polarity of $v_{\mathrm{db},x}$ and sign of Δu_x defines the initial switch position in phase x. For example, if $v_{\mathrm{db},x} \geq 0$ the feasible switch positions in phase x are either 0 or 1 as a non-negative output voltage is required. If $\Delta u_x > 0$, it means that $u_x(t_0) = 0$ as a transition from 0 to 1 is required in phase x within T_s. If, on the other hand, $\Delta u_x < 0$, then it holds that $u_x(t_0) = 1$ as phase x needs to switch from 1 to 0. Following the same principle, the feasible switch positions—and eventually $u_x(t_0)$—for the case of $v_{\mathrm{db},x} < 0$ are defined. The switching transitions and initial single-phase switch position are summarized in Table 4.2. Moreover, Fig. 4.6 provides an illustrative example of the discussed concept. Therein, it is assumed that

[2]This corresponds to the case where $\boldsymbol{u}_{abc}(t_0) = [0\ 0\ 0]^T$. In such a case, each single-phase switch position can become either 1 or -1 within one T_s. As a result, there are $2^3 = 8$ switching sequences for a given order with which the phases switch. As there are six different chronological orders for the phases to switch (see Table 4.1), the maximum number of candidate switching sequences is $8 \times 6 = 48$.

[3]Directly switching a phase leg from -1 to 1, or vice versa, is forbidden to avoid a potential shoot-through.

[4]Note that the discrete state-space model of the IM can be obtained with forward Euler discretization, i.e., $\boldsymbol{A}_m = \boldsymbol{I} + \boldsymbol{F}_m T_s$ and $\boldsymbol{B}_m = \boldsymbol{G}_m T_s$.

Algorithm 2 Fixed Switching Frequency Direct MPC

Given $\boldsymbol{y}_{\mathrm{ref}}(k)$, $\boldsymbol{y}_{\mathrm{ref}}(k+1)$ and $\boldsymbol{x}(k)$
1: Compute the deadbeat solution $\boldsymbol{v}_{\mathrm{db},abc}$ according to (4.34)
2: Enumerate the possible switching sequences $\boldsymbol{U}_z$, $z \in \{1, 2, \ldots, 6\}$, based on $\boldsymbol{v}_{\mathrm{db},abc}$ and the sign of the switching transitions $\Delta \boldsymbol{u}_{abc}$
3: For each $\boldsymbol{U}_z$:
Detect if $\boldsymbol{U}_z$ is unsuited;
If not, solve the QP (4.36). This yields $\boldsymbol{t}_z$ and J_z.
4: Solve optimization problem (4.37). This yields $\boldsymbol{t}^*$ and $\boldsymbol{U}^*$.
Return $\boldsymbol{t}^*(k)$ and $\boldsymbol{U}^*(k)$.

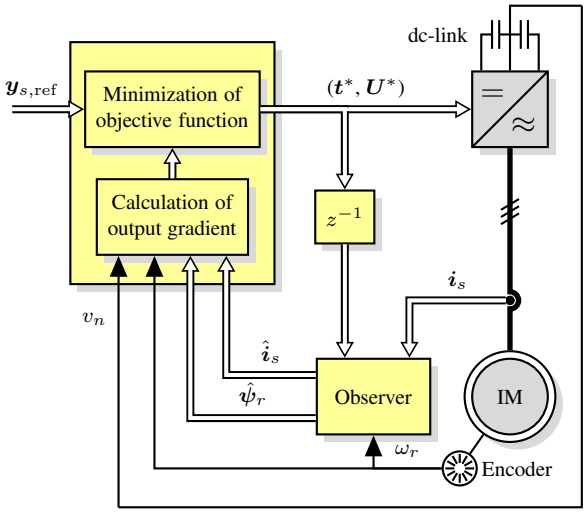

Figure 4.7: Fixed switching frequency direct MPC for a three-phase NPC inverter driving an IM.

$v_{\mathrm{db},a}, v_{\mathrm{db},c} \geq 0$, whereas $v_{\mathrm{db},b} < 0$. Furthermore, the sign of $\Delta \boldsymbol{u}_{abc}(k)$ for the first sampling interval is assumed to be positive, implying a negative sign for the second T_s.
Finally, with the information of the initial switch position $\boldsymbol{u}_{abc}(t_0)$ and possible switching transitions, the feasible set of switching sequences is constructed by enumerating the six possible sequences shown in Table 4.1. Let $z \in \{1, 2, \ldots, 6\}$ denote the number of sequence, the feasible set consists of only six candidate switching sequences

$$\boldsymbol{U}_z = [\boldsymbol{u}_{abc}^T(t_0)\ \boldsymbol{u}_{abc,z}^T(t_1)\ \boldsymbol{u}_{abc,z}^T(t_2)\ \boldsymbol{u}_{abc}^T(t_3)]^T\,. \tag{4.35}$$

4.2.4 Optimization Problem

To find the optimal switching instants $\boldsymbol{t}^*$ and switching sequence $\boldsymbol{U}^*$, the optimization problem for each switching sequence $\boldsymbol{U}_z$, with $z \in \{1, 2, \ldots, 6\}$, is solved in real time, i.e.,

$$\begin{aligned} \underset{\boldsymbol{t} \in \mathbb{R}^3}{\text{minimize}} \quad & \|\boldsymbol{r} - \boldsymbol{M}\boldsymbol{t}\|_{\tilde{\boldsymbol{Q}}}^2 \\ \text{subject to} \quad & 0 \leq t_1(k) \leq t_2(k) \leq t_3(k) \leq T_s\,. \end{aligned} \tag{4.36}$$

In a last step the (globally) optimal switching instants $\boldsymbol{t}^*$ and sequence $\boldsymbol{U}^*$ is found by comparing the cost J_z of each switching sequence, i.e., the following problem is solved

$$\underset{z \in \{1,2,\ldots,6\}}{\text{minimize}} \quad J_z \,. \tag{4.37}$$

Finally, the optimal switching sequence $\boldsymbol{U}^*$ is applied to the inverter at the corresponding optimal switching instants $\boldsymbol{t}^*$.
The proposed direct MPC scheme is summarized in the pseudocode provided in Algorithm 2, while the block diagram is shown in Fig. 4.7. Finally it should be mentioned that a Kalman filter (KF) is implemented to deal with model uncertainties and measurement noises.

CHAPTER 5

Implementation of the Direct MPC Method for Drive Systems

In order to render the real-time implementation of the direct MPC method possible, a computational efficient solution of the underlying MPC problem is proposed in [26], where an efficient and highly reliable gradient-based QP solver is developed. Moreover, a mechanism is proposed that can detect the unsuited switching sequences with only a few computation. As a result, the direct MPC scheme becomes computationally feasible for real-time implementations. This chapter presents the proposed gradient-based QP solver and the performance of the direct MPC scheme evaluated with experimental tests.

5.1 Gradient Methods for Direct MPC

Gradient projection methods have shown to be very efficient for QPs, especially when the constraints are simple. In particular, they have been widely used for QPs where the variables of interest are only box-constrained [46]. For general QPs, projecting the variables onto the feasible region may require significant computations. However, the constraints in many MPC problems for power electronic systems are simple and regular (i.e., global), thus the projection onto the problem-specific feasible region can be efficiently performed by fully exploiting its geometry. In this section, we propose a computationally efficient projection method for the QP problem of the direct MPC discussed in Chapter 4. The flowchart that summarizes the proposed gradient-based direct MPC scheme and the QP solver is shown in Fig. 5.1.

5.1.1 Reformulation of the Feasible Set

The feasible set of the QP problem (4.36) is a so-called truncated monotone cone. The projection of a variable onto a truncated monotone cone is complicated, see [47] and references

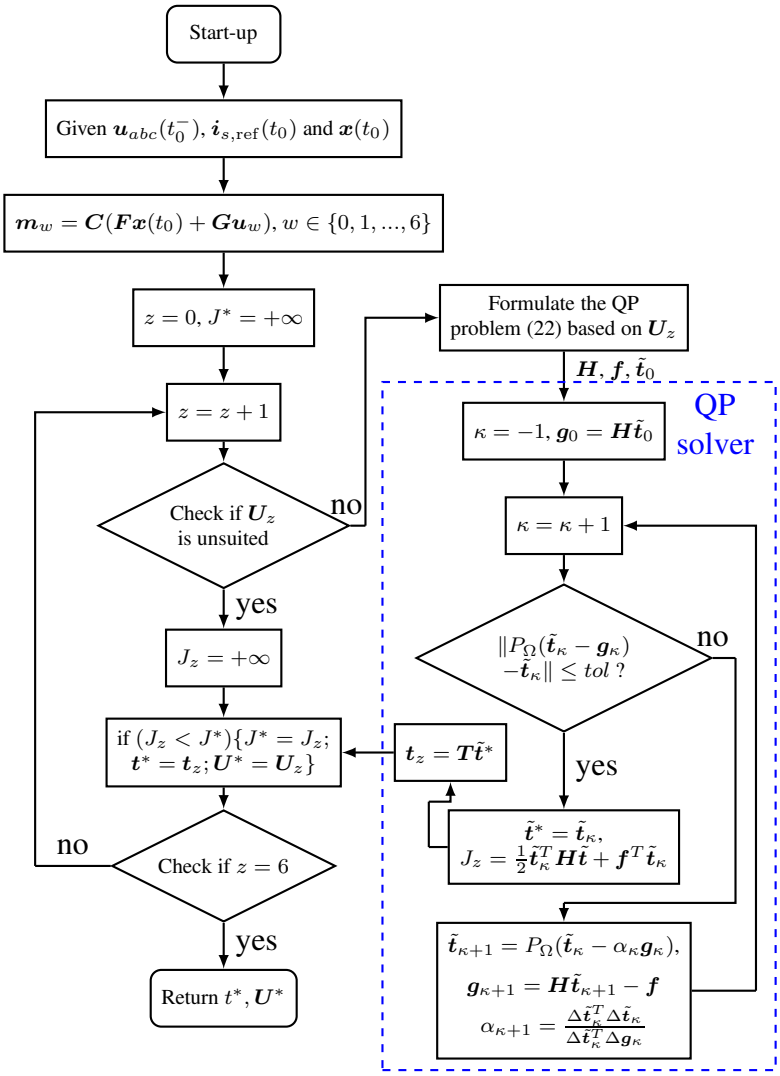

Figure 5.1: Flowchart of the proposed fixed switching frequency direct MPC scheme.

therein. Although some algorithms exist, they rely on complex approaches, such as multiparametric programming [47], or involve computationally intensive operations, such as the computation of pseudo-inverses of matrices [48].

To address this and to achieve a computationally efficient projection, the feasible set is first reformulated by introducing the new variables $\tilde{t}_i = t_i - t_{i-1}$, with $i \in \{1, 2, 3, 4\}$ and $t_4 = T_s$. Note that $\tilde{t}_i$ is essentially the application time of the switch position $\boldsymbol{u}_{abc}(t_{i-1})$. In doing so, the feasible set can be described by simple bound constraints and one equality constraint, i.e., $\tilde{t}_i \geq 0$, and $\sum_{i=1}^{4} \tilde{t}_i = T_s$. This concept can be applied to all variables involved in the long-horizon direct MPC problem.

Based on the above, the vector of application times is defined as

$$\tilde{\boldsymbol{t}} = \begin{bmatrix} \tilde{\boldsymbol{t}}^T(k) & \tilde{\boldsymbol{t}}^T(k+1) \end{bmatrix}^T \tag{5.1}$$

where

$$\tilde{\boldsymbol{t}}(\ell) = \begin{bmatrix} \tilde{t}_1(\ell) & \tilde{t}_2(\ell) & \tilde{t}_3(\ell) & \tilde{t}_4(\ell) \end{bmatrix}^T. \tag{5.2}$$

With (5.1), function (4.10) is rewritten as

$$J = \|\tilde{\boldsymbol{r}} - \tilde{\boldsymbol{M}}\tilde{\boldsymbol{t}}\|_2^2\,, \tag{5.3}$$

where the vector $\tilde{\boldsymbol{r}}$ and matrix $\tilde{\boldsymbol{M}}$ are

$$\tilde{\boldsymbol{r}} = \begin{bmatrix} \boldsymbol{i}_{s,\mathrm{ref}}(t_0) - \boldsymbol{i}_s(t_0) \\ \boldsymbol{i}_{s,\mathrm{ref}}(t_0) - \boldsymbol{i}_s(t_0) \\ \boldsymbol{i}_{s,\mathrm{ref}}(t_0) - \boldsymbol{i}_s(t_0) \\ \boldsymbol{\Lambda}(\boldsymbol{i}_{s,\mathrm{ref}}(t_0) - \boldsymbol{i}_s(t_0)) \\ \boldsymbol{i}_{s,\mathrm{ref}}(t_0) - \boldsymbol{i}_s(t_0) \\ \boldsymbol{i}_{s,\mathrm{ref}}(t_0) - \boldsymbol{i}_s(t_0) \\ \boldsymbol{i}_{s,\mathrm{ref}}(t_0) - \boldsymbol{i}_s(t_0) \\ \boldsymbol{\Lambda}(\boldsymbol{i}_{s,\mathrm{ref}}(t_0) - \boldsymbol{i}_s(t_0)) \end{bmatrix} \tag{5.4}$$

and

$$\tilde{\boldsymbol{M}} = \begin{bmatrix} \tilde{\boldsymbol{m}}_0 & \boldsymbol{0}_2 & \boldsymbol{0}_2 & \boldsymbol{0}_2 & \boldsymbol{0}_2 & \boldsymbol{0}_2 & \boldsymbol{0}_2 & \boldsymbol{0}_2 \\ \tilde{\boldsymbol{m}}_0 & \tilde{\boldsymbol{m}}_1 & \boldsymbol{0}_2 & \boldsymbol{0}_2 & \boldsymbol{0}_2 & \boldsymbol{0}_2 & \boldsymbol{0}_2 & \boldsymbol{0}_2 \\ \tilde{\boldsymbol{m}}_0 & \tilde{\boldsymbol{m}}_1 & \tilde{\boldsymbol{m}}_2 & \boldsymbol{0}_2 & \boldsymbol{0}_2 & \boldsymbol{0}_2 & \boldsymbol{0}_2 & \boldsymbol{0}_2 \\ \tilde{\boldsymbol{m}}_{0_{\boldsymbol{\Lambda}}} & \tilde{\boldsymbol{m}}_{1_{\boldsymbol{\Lambda}}} & \tilde{\boldsymbol{m}}_{2_{\boldsymbol{\Lambda}}} & \tilde{\boldsymbol{m}}_{3_{\boldsymbol{\Lambda}}} & \boldsymbol{0}_2 & \boldsymbol{0}_2 & \boldsymbol{0}_2 & \boldsymbol{0}_2 \\ \tilde{\boldsymbol{m}}_0 & \tilde{\boldsymbol{m}}_1 & \tilde{\boldsymbol{m}}_2 & \tilde{\boldsymbol{m}}_3 & \tilde{\boldsymbol{m}}_0 & \boldsymbol{0}_2 & \boldsymbol{0}_2 & \boldsymbol{0}_2 \\ \tilde{\boldsymbol{m}}_0 & \tilde{\boldsymbol{m}}_1 & \tilde{\boldsymbol{m}}_2 & \tilde{\boldsymbol{m}}_3 & \tilde{\boldsymbol{m}}_{\bar{0}} & \tilde{\boldsymbol{m}}_{\bar{1}} & \boldsymbol{0}_2 & \boldsymbol{0}_2 \\ \tilde{\boldsymbol{m}}_0 & \tilde{\boldsymbol{m}}_1 & \tilde{\boldsymbol{m}}_2 & \tilde{\boldsymbol{m}}_3 & \tilde{\boldsymbol{m}}_{\bar{0}} & \tilde{\boldsymbol{m}}_{\bar{1}} & \tilde{\boldsymbol{m}}_{\bar{2}} & \boldsymbol{0}_2 \\ \tilde{\boldsymbol{m}}_{0_{\boldsymbol{\Lambda}}} & \tilde{\boldsymbol{m}}_{1_{\boldsymbol{\Lambda}}} & \tilde{\boldsymbol{m}}_{2_{\boldsymbol{\Lambda}}} & \tilde{\boldsymbol{m}}_{3_{\boldsymbol{\Lambda}}} & \tilde{\boldsymbol{m}}_{\bar{0}_{\boldsymbol{\Lambda}}} & \tilde{\boldsymbol{m}}_{\bar{1}_{\boldsymbol{\Lambda}}} & \tilde{\boldsymbol{m}}_{\bar{2}_{\boldsymbol{\Lambda}}} & \tilde{\boldsymbol{m}}_{\bar{3}_{\boldsymbol{\Lambda}}} \end{bmatrix} \tag{5.5}$$

with

$$\tilde{\boldsymbol{m}}_i = \boldsymbol{m}(t_i(k)) - \boldsymbol{m}_{\mathrm{ref}}(k)) \tag{5.6}$$

$$\tilde{\boldsymbol{m}}_{i_{\boldsymbol{\Lambda}}} = \boldsymbol{\Lambda}\tilde{\boldsymbol{m}}_i \tag{5.7}$$

$$\tilde{\boldsymbol{m}}_{\bar{i}} = \boldsymbol{m}(t_i(k+1)) - \boldsymbol{m}_{\mathrm{ref}}(k+1)) \tag{5.8}$$

$$\tilde{\boldsymbol{m}}_{\bar{i}_{\boldsymbol{\Lambda}}} = \boldsymbol{\Lambda}\tilde{\boldsymbol{m}}_{\bar{i}}\,, \tag{5.9}$$

where $i \in \{0, 1, 2, 3\}$. After expanding (5.3) as

$$J = \tilde{\boldsymbol{t}}^T\tilde{\boldsymbol{M}}^T\tilde{\boldsymbol{M}}\tilde{\boldsymbol{t}} - 2\tilde{\boldsymbol{r}}^T\tilde{\boldsymbol{M}}\tilde{\boldsymbol{t}} + \tilde{\boldsymbol{r}}^T\tilde{\boldsymbol{r}} \tag{5.10}$$

and by omitting the constant term $\tilde{\boldsymbol{r}}^T\tilde{\boldsymbol{r}}$, the reformulated optimization problem can be stated as

$$\begin{aligned} \underset{\tilde{\boldsymbol{t}} \in \mathbb{R}^8}{\text{minimize}} \quad & \frac{1}{2}\tilde{\boldsymbol{t}}^T\boldsymbol{H}\tilde{\boldsymbol{t}} - \boldsymbol{f}^T\tilde{\boldsymbol{t}} \\ \text{subject to} \quad & \tilde{\boldsymbol{t}} \succeq \boldsymbol{0} \\ & \sum_{i=1}^{4} \tilde{t}_i(\ell) = T_s,\ \forall \ell = k, k+1\,, \end{aligned} \tag{5.11}$$

where $\boldsymbol{H} = 2\tilde{\boldsymbol{M}}^T\tilde{\boldsymbol{M}}$ is a symmetric, positive (semi)definite matrix, $\boldsymbol{f} = 2\tilde{\boldsymbol{M}}^T\tilde{\boldsymbol{r}}$, $\boldsymbol{0}$ is a zero vector of appropriate dimensions, and $\succeq$ denotes componentwise inequality. Note that after the QP problem (5.11) has been solved, the switching time instants $\boldsymbol{t}$ can be simply calculated as

$$\boldsymbol{t} = \boldsymbol{T}\tilde{\boldsymbol{t}}\,, \tag{5.12}$$

where the transformation matrix $\boldsymbol{T}$ is

$$\boldsymbol{T} = \begin{bmatrix} \tilde{\boldsymbol{I}} & \boldsymbol{0}_3 & \boldsymbol{0}_{3\times 3} & \boldsymbol{0}_3 \\ \boldsymbol{0}_{3\times 3} & \boldsymbol{0}_3 & \tilde{\boldsymbol{I}} & \boldsymbol{0}_3 \end{bmatrix}. \tag{5.13}$$

5.1.2 Projection onto the Feasible Region

An important step in gradient methods for constrained QP problems is the projection of the variables of interest onto the feasible region. Let the feasible region of (5.11) be defined as

$$\Omega \coloneqq \{\tilde{\boldsymbol{t}} \mid \tilde{\boldsymbol{t}} \succeq \boldsymbol{0}, \sum_{i=1}^{4} \tilde{t}_i = \sum_{i=5}^{8} \tilde{t}_i = T_s, \tilde{\boldsymbol{t}} \in \mathbb{R}^8\}\,.$$

The projection of any vector $\boldsymbol{z}$ onto Ω is the minimizer of the problem

$$\underset{\tilde{\boldsymbol{\tau}} \in \Omega}{\text{minimize}} \quad \|\tilde{\boldsymbol{\tau}} - \boldsymbol{z}\|_2^2\,. \tag{5.14}$$

The proposed projection algorithm is based on constructing the associated Lagrangian of (5.14), i.e.,

$$\mathcal{L}(\tilde{\boldsymbol{\tau}}, \lambda_1, \lambda_2, \boldsymbol{\mu}) = \frac{1}{2}\tilde{\boldsymbol{\tau}}^T\tilde{\boldsymbol{\tau}} - \boldsymbol{z}^T\tilde{\boldsymbol{\tau}} - \lambda_1(\boldsymbol{a}_1^T\tilde{\boldsymbol{\tau}} - T_s) - \lambda_2(\boldsymbol{a}_2^T\tilde{\boldsymbol{\tau}} - T_s) - \boldsymbol{\mu}^T\tilde{\boldsymbol{\tau}}\,, \tag{5.15}$$

where $\lambda_1, \lambda_2 \in \mathbb{R}$ and $\boldsymbol{\mu} \in \mathbb{R}^8$ are the so-called Lagrangian multipliers. Moreover, $\boldsymbol{a}_1 = [\boldsymbol{1}_4^T\ \boldsymbol{0}_4^T]^T$ and $\boldsymbol{a}_2 = [\boldsymbol{0}_4^T\ \boldsymbol{1}_4^T]^T$ are the vectors of the equality constraints, where $\boldsymbol{0}$ and $\boldsymbol{1}$ are vectors with all components being zero and one, respectively, and of dimension indicated by their subscript. The first-order necessary conditions, which are known as the Karush-Kuhn-Tucker (KKT) conditions, state that if $\tilde{\boldsymbol{\tau}}^*$, i.e., the projection point, is a local solution of (5.14), then there is a set of Lagrangian multipliers $\{\boldsymbol{\mu}^*, \lambda_1^*, \lambda_2^*\}$, such that the following conditions are satisfied at $(\tilde{\boldsymbol{\tau}}^*, \lambda_1^*, \lambda_2^*, \boldsymbol{\mu}^*)$ [46]

$$\tilde{\boldsymbol{\tau}}^* - \boldsymbol{z} - \lambda_1^*\boldsymbol{a}_1 - \lambda_2^*\boldsymbol{a}_2 - \boldsymbol{\mu}^* = \boldsymbol{0}\,, \tag{5.16a}$$

$$\tilde{\boldsymbol{\tau}}^* \succeq \boldsymbol{0},\ \boldsymbol{\mu}^* \succeq \boldsymbol{0}\,, \tag{5.16b}$$

$$\tilde{\boldsymbol{\tau}}^* \odot \boldsymbol{\mu}^* = \boldsymbol{0}\,, \tag{5.16c}$$

$$\boldsymbol{a}_1^T\tilde{\boldsymbol{\tau}}^* = T_s,\ \boldsymbol{a}_2^T\tilde{\boldsymbol{\tau}}^* = T_s\,, \tag{5.16d}$$

where $\odot$ denotes the componentwise product. For the convex QP (5.14) satisfaction of the KKT conditions (5.16) suffices for $\tilde{\boldsymbol{\tau}}^*$ to be a global solution [49]. In the following, it is shown how $\tilde{\boldsymbol{\tau}}^*$ can be found by solving the KKT conditions (5.16).

First, it is noted that (5.16) can be split into two decoupled sets of equations[1]

$$\tilde{\boldsymbol{\tau}}^*_{(4\zeta-3:4\zeta)} - \boldsymbol{z}_{(4\zeta-3:4\zeta)} - \lambda^*_\zeta \mathbf{1}_4 - \boldsymbol{\mu}^*_{(4\zeta-3:4\zeta)} = \mathbf{0}\,, \tag{5.17a}$$

$$\tilde{\boldsymbol{\tau}}^*_{(4\zeta-3:4\zeta)} \succeq \mathbf{0},\ \boldsymbol{\mu}^*_{(4\zeta-3:4\zeta)} \succeq \mathbf{0}\,, \tag{5.17b}$$

$$\tilde{\boldsymbol{\tau}}^*_{(4\zeta-3:4\zeta)} \odot \boldsymbol{\mu}^*_{(4\zeta-3:4\zeta)} = \mathbf{0}\,, \tag{5.17c}$$

$$\sum_{i=4\zeta-3}^{4\zeta} \tilde{\tau}^*_i = T_s\,, \tag{5.17d}$$

where the value of $\zeta \in \{1, 2\}$ indicates the prediction horizon step. Therefore, the two equation sets (5.17) can be solved separately. By taking $\zeta = 1$ as an example, (5.17a) can be expanded to four scalar equations as

$$\tilde{\tau}_i = z_i + \lambda_1 + \mu_i,\ i \in \{1, 2, 3, 4\}\,. \tag{5.18}$$

Combining (5.18) with (5.17b) and (5.17c), it yields

$$(\tilde{\tau}_i,\ \mu_i) = \begin{cases} (0,\ -\lambda_1 - z_i) & \text{if} \quad \lambda_1 < -z_i \\ (z_i + \lambda_1,\ 0) & \text{otherwise}\,. \end{cases} \tag{5.19}$$

If there exists λ_1 such that $\sum_{i=1}^4 \tilde{\tau}^*_i = T_s$—denoted as λ^*_1—it follows that the KKT conditions (5.16) with $\zeta = 1$ are satisfied. As a result, the solution $\tilde{\boldsymbol{\tau}}^*_{(1:4)}$ can be obtained directly from (5.19). Specifically, based on (5.19), $\sum_{i=1}^4 \tilde{\tau}_i$ can be written as a piecewise linear continuous function of λ_1

$$f(\lambda_1) = \sum_{i=1}^4 \tilde{\tau}_i = \begin{cases} 0 & \text{if } \lambda_1 < -\tilde{z}_1 \\ \tilde{z}_1 + \lambda_1 & \text{if } -\tilde{z}_1 \le \lambda_1 < -\tilde{z}_2 \\ \vdots & \\ \sum_{i=1}^4 \tilde{z}_i + 4\lambda_1 & \text{if } -\tilde{z}_4 \le \lambda_1\,, \end{cases} \tag{5.20}$$

where $\tilde{\boldsymbol{z}}$ includes the elements of $\boldsymbol{z}$ sorted in a descending order. Since $f(\lambda_1)$ is either constant or increasing monotonically and linearly with λ_1, λ^*_1 can be found by examining the value of $f(\lambda_1)$ at its breakpoints $\tilde{\lambda}_i$. From (5.20), it is evident that $f(\lambda_1)$ has four breakpoints, i.e., $\tilde{\lambda}_i = -\tilde{z}_i$ for $i \in \{1, 2, 3, 4\}$. Once a $\tilde{\lambda}_j$ is found such that $f(\tilde{\lambda}_{j-1}) \le T_s$ and $f(\tilde{\lambda}_j) \ge T_s$, then λ^*_1 is in the interval $[\tilde{\lambda}_{j-1}, \tilde{\lambda}_j]$ and can be obtained by linear interpolation. If λ^*_1 is not found after all the breakpoints are examined, then λ^*_1 is located in the interval $[\tilde{\lambda}_4, +\infty)$ and it is equal to $\lambda^*_1 = (T_s - \sum_{i=1}^4 \tilde{z}_i)/4$.

Once λ^*_1 and $\tilde{\boldsymbol{\tau}}^*_{(1:4)}$ are obtained, λ^*_2 and $\tilde{\boldsymbol{\tau}}^*_{(5:8)}$ can be found by setting $\zeta = 2$ and following the same procedure. The proposed projection algorithm is summarized in Algorithm 3.

[1]The notation $\tilde{\boldsymbol{\tau}}^*_{(4\zeta-3:4\zeta)}$, $\boldsymbol{z}_{(4\zeta-3:4\zeta)}$, and $\boldsymbol{\mu}^*_{(4\zeta-3:4\zeta)}$ indicates the entries from $4\zeta - 3$ up to 4ζ of $\tilde{\boldsymbol{\tau}}^*$, $\boldsymbol{z}$, and $\boldsymbol{\mu}^*$, respectively.

Algorithm 3 Projection onto Ω

function $\tilde{\boldsymbol{\tau}}^* = P_\Omega(\boldsymbol{z})$
  for $\zeta = 1,\ 2$ **do**
    $\tilde{\boldsymbol{z}} = \mathrm{sort}(\boldsymbol{z}_{(4\zeta-3:4\zeta)}, \mathrm{descend})$
    $\tilde{\boldsymbol{\lambda}} = -\tilde{\boldsymbol{z}}$
    $f(\tilde{\lambda}_1) = 0$
    for $j = 2$ to 4 **do**
      $f(\tilde{\lambda}_j) = \sum_{i=1}^{j} \tilde{z}_i + j\tilde{\lambda}_j$
      if $f(\tilde{\lambda}_j) \geq T_s$ **then**
        $\lambda_\zeta^* = \tilde{\lambda}_{j-1} + (\tilde{\lambda}_j - \tilde{\lambda}_{j-1})\frac{(T_s - f(\tilde{\lambda}_{j-1}))}{(f(\tilde{\lambda}_j) - f(\tilde{\lambda}_{j-1}))}$
        break
      else
        if $j = 4$ **then**
          $\lambda_\zeta^* = (T_s - \sum_{i=1}^{4} \tilde{z}_i)/4$
          break
        end if
      end if
    end for
    $\tilde{\boldsymbol{\tau}}^*_{(4\zeta-3:4\zeta)} = \max\{\mathbf{0}_4, \boldsymbol{z}_{(4\zeta-3:4\zeta)} + \lambda_\zeta^* \mathbf{1}_4\}$
  end for
  return $\tilde{\boldsymbol{\tau}}^*$
end function

5.1.3 Gradient Projection Method for Direct MPC

5.1.3.1 Steepest Descent Method with BB step

To find the solution $\tilde{\boldsymbol{t}}^*$ of problem (5.11), many commonly used gradient projection methods search along the steepest descent direction from the current point $\tilde{\boldsymbol{t}}_\kappa$, i.e.,

$$\tilde{\boldsymbol{t}}_{\kappa+1} = \tilde{\boldsymbol{t}}_\kappa - \alpha_\kappa \boldsymbol{g}_\kappa \,, \tag{5.21}$$

where $\boldsymbol{g}_\kappa = \boldsymbol{H}\tilde{\boldsymbol{t}}_\kappa - \boldsymbol{f}$ is the gradient vector at $\tilde{\boldsymbol{t}}_\kappa$, $\alpha_\kappa \in \mathbb{R}^+$ is the step size, and $\kappa \in \mathbb{N}$ denotes the κ^{th} step of the solution process. Following, $\tilde{\boldsymbol{t}}_{\kappa+1}$ is projected onto the feasible region Ω by invoking Algorithm 3, i.e., $\tilde{\boldsymbol{\tau}}^*_{\kappa+1} = P_\Omega(\tilde{\boldsymbol{t}}_{\kappa+1})$, where P_Ω refers to the projection function provided in Algorithm 3. Subsequently, the process continues from point $\tilde{\boldsymbol{\tau}}^*_{\kappa+1}$ by considering it as the next starting point in (5.21), i.e., $\tilde{\boldsymbol{t}}_{\kappa+1} \equiv \tilde{\boldsymbol{\tau}}^*_{\kappa+1}$.

As can be understood, an important factor that affects the rate of convergence of the gradient method is the step size α_κ. In the classic steepest descent method this is chosen by exact line search, i.e., by searching for the optimal point along the steepest descent direction. However, it has been shown that the rate of convergence of the classical method is slow and it gets worse as the QP problem becomes ill-posed. As an alternative, Barzilai and Borwein proposed a strategy—known as the BB method—for choosing the step size [50], which offers several advantages over the classical method, such as less computational effort, fast convergence, and less sensitivity to ill conditioning [51, 52]. According to the BB step [50], the step size in (5.21) is

Algorithm 4 QP Algorithm for Direct MPC

function $\boldsymbol{t}^* = \text{GRADPROJ}(\boldsymbol{H}, \boldsymbol{f}, \boldsymbol{t}_0, \alpha_0, tol)$
  $\boldsymbol{g}_0 = \boldsymbol{H}\boldsymbol{t}_0 - \boldsymbol{f}$
  for $\kappa = 0,\ 1,\ \ldots$ **do**
    if $\|P_\Omega(\boldsymbol{t}_\kappa - \boldsymbol{g}_\kappa) - \boldsymbol{t}_\kappa\| \leq tol$ **then**
      $\boldsymbol{t}^* = \boldsymbol{t}_\kappa$
      break
    end if
    $\boldsymbol{\tau}^*_{\kappa+1} = P_\Omega(\boldsymbol{t}_\kappa - \alpha_\kappa \boldsymbol{g}_\kappa)$
    $\boldsymbol{t}_{\kappa+1} = \boldsymbol{\tau}^*_{\kappa+1}$
    $\boldsymbol{g}_{\kappa+1} = \boldsymbol{H}\tilde{\boldsymbol{t}}_{\kappa+1} - \boldsymbol{f}$
    $\alpha_{\kappa+1} = (\Delta \boldsymbol{t}_\kappa^T \Delta \boldsymbol{t}_\kappa)/(\Delta \boldsymbol{t}_\kappa^T \Delta \boldsymbol{g}_\kappa)$
  end for
  return $\boldsymbol{t}^*$
end function

chosen as

$$\alpha_{\kappa+1} = \frac{\Delta \tilde{\boldsymbol{t}}_\kappa^T \Delta \tilde{\boldsymbol{t}}_\kappa}{\Delta \tilde{\boldsymbol{t}}_\kappa^T \Delta \boldsymbol{g}_\kappa}\,, \tag{5.22}$$

where $\Delta \tilde{\boldsymbol{t}}_\kappa = \tilde{\boldsymbol{t}}_{\kappa+1} - \tilde{\boldsymbol{t}}_\kappa$ and $\Delta \boldsymbol{g}_\kappa = \boldsymbol{g}_{\kappa+1} - \boldsymbol{g}_\kappa$. With (5.21) and (5.22), the algorithm continuous in an iterative manner until it fulfills an optimization criterion. Specifically, the process terminates when $\|P_\Omega(\tilde{\boldsymbol{t}}_\kappa - \boldsymbol{g}_\kappa) - \tilde{\boldsymbol{t}}_\kappa\|$ is within a predetermined tolerance.

Based on the above, the complete algorithm for solving (5.11) is summarized in Algorithm 4. The arguments of the algorithm are the Hessian matrix $\boldsymbol{H}$, and the vector $\boldsymbol{f}$, as defined in (5.11) as well as the initial point $\tilde{\boldsymbol{t}}_0 \in \Omega$, the initial step α_0, and the value of the tolerance tol. The initial point can be chosen according to a warm-start strategy, e.g., based on the previously computed solution $\tilde{\boldsymbol{t}}^*(k+1)$. Moreover, in this work, as shown in Section 5.1.4, $\tilde{\boldsymbol{t}}_0$ is also utilized for detecting unsuited switching sequences $\boldsymbol{U}$. As for the initial step size α_0, it marginally affects the convergence of the algorithm, since it is updated in every iteration of the search process according to (5.22). On the other hand, the tolerance tol can considerably affect the rate of convergence, since a very small value can result in a slow convergence. However, the exact solution is not necessary since the model itself is not ideal. Hence, in this work, tol is set to 10^{-6}, which means that the optimal switching application times $\tilde{\boldsymbol{t}}^*$ are acceptable within a tolerance of $1\,\mu$s. Considering that the sampling interval for the examined case study is a few hundreds of microseconds, a solution with $1\,\mu$s tolerance is accurate enough.

Finally, it is worth mentioning that the BB methods are inherently non-monotonic, which means that the value of the objective function may increase at some iterations. To tackle this, a line search is required to prove the convergence, and some studies, e.g., [53], have reported some cases that the BB methods without line search fail to converge. However, this happens rarely and only in large-scale problems. For small-scale QPs, as the one presented in (5.11), the employed BB method always converges efficiently without requiring a line search. For more details about the line search strategy, see [51] and references therein.

Algorithm 5 QP Algorithm for Direct MPC

function $\boldsymbol{t}_z = \text{GRADPROJ}(\boldsymbol{H},\ \boldsymbol{f}, \boldsymbol{t}_0, L, \mu, tol)$
  $q = \mu / L$
  $\boldsymbol{y}_0 = \boldsymbol{t}_0$
  $\alpha_0 = (\sqrt{(L-\mu)^2 + 4L} - (L-\mu))/2$
  for $\kappa = 0,\ 1,\ \ldots$ **do**
    $\boldsymbol{t}_{\kappa+1} = P_\Omega(\boldsymbol{y}_\kappa - (\boldsymbol{H}\boldsymbol{y}_\kappa - \boldsymbol{f})/L)$
    if $\|\boldsymbol{t}_{\kappa+1} - \boldsymbol{t}_\kappa\| \leq tol$ **then**
      $\boldsymbol{t}_z = \boldsymbol{t}_{\kappa+1}$
      break
    end if
    $\alpha_{\kappa+1} = (\sqrt{(\alpha_\kappa^2 - q)^2 + 4\alpha_\kappa^2} - (\alpha_\kappa^2 - q))/2$
    $\beta_\kappa = (\alpha_\kappa(1-\alpha_\kappa))/(\alpha_\kappa^2 + \alpha_{\kappa+1})$
    $\boldsymbol{y}_{\kappa+1} = \boldsymbol{t}_{\kappa+1} + \beta_\kappa(\boldsymbol{t}_{\kappa+1} - \boldsymbol{t}_\kappa)$
  end for
  return $\boldsymbol{t}_z$
end function

5.1.3.2 Nesterov Fast Gradient Method

The main advantage of the BB method lies in its robustness to ill-posed QPs. However, when Hessian matrix $\boldsymbol{H}$ is well conditioned, i.e., its condition number—which is defined as the largest eigenvalue of the Hessian matrix divided by its smallest eigenvalue—is relatively small, the Nesterov fast gradient method [54, 55] results in a more efficient convergence. Algorithm 5 shows the pseudocode of the modified QP algorithm, where the so-called Lipschitz constant L and convexity parameter μ are the maximum and minimum eigenvalues of the Hessian matrix $\boldsymbol{H}$, respectively. Moreover, the vector $\boldsymbol{f}$ is defined as $\boldsymbol{f} = 2\boldsymbol{M}^T\boldsymbol{r}$. Besides, P_Ω denotes the operation that projects any variable onto the feasible region Ω, $\boldsymbol{t}_0 \in \Omega$ is the initial point, and $tol \in \mathbb{R}^+$ is the tolerance.

5.1.4 Detection of Unsuited Switching Sequences

As explained in Chapter 4, the direct MPC scheme enumerates the feasible switching sequences and selects the one that minimizes (4.37). According to the control principle presented in Section 4.1.2, each switching sequence in one sampling interval T_s consists of four switch positions; two of them correspond to zero vectors in the $\alpha\beta$-plane—applied at the beginning and end of T_s—and the other two to adjacent active vectors—applied in between, see Fig. 4.2(a). However, not all active vectors positively affect the tracking of the stator current reference. Such active vectors, and consequently the corresponding switching sequences, can be detected quickly by the proposed gradient projection method, as explained below.[2]

[2] An alternative to determine the "suitable" switching sequence is to utilize the deadbeat solution of the control problem, i.e., the modulating signal that a deadbeat controller would use. In doing so, the triangular sector in which the modulating signal lies would provide the desired switching sequence, see Fig. 4.3. However, such an approach can lead to suboptimal solutions [8, Section VII], thus the proposed method is preferred since it guarantees optimality.

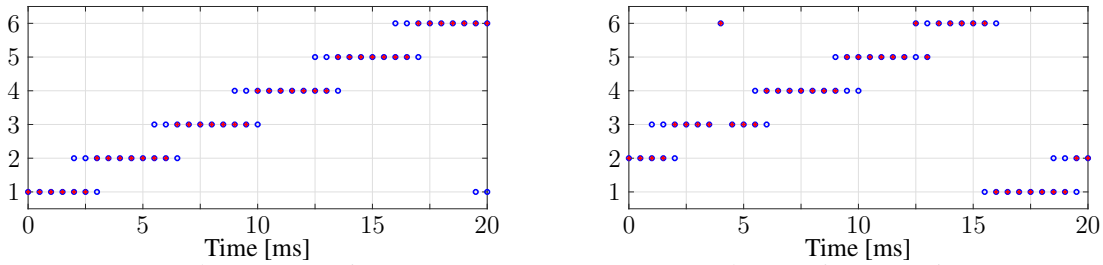

(a) Steady-state operation. (b) Transient operation.

Figure 5.2: Switching sequences selected by the detection method (blue circles) and the globally optimal switching sequence (red cross).

To do so, consider one-step MPC and let the initial point be $\tilde{\boldsymbol{t}}_0 = [T_s/2\ 0\ 0\ T_s/2]$. The steepest descent direction can be obtained by calculating its gradient vector $\boldsymbol{g}_0 = \boldsymbol{H}\tilde{\boldsymbol{t}}_0 - \boldsymbol{f}$. If this direction points to the region where $\tilde{\boldsymbol{t}}$ has negative duration time for an active vector, i.e., the second and third entries of $\tilde{\boldsymbol{t}}$, it can be concluded that this active vector will adversely affect the system performance if applied to the inverter, thus the associated switching sequence is suboptimal.
To allow the gradient projection to reach the region where $\tilde{t}_i < 0$, the bound constraints are neglected so that the *relaxed* feasible region is defined as

$$\Omega_0 \coloneqq \{\tilde{\boldsymbol{t}} \mid \sum_{i=1}^{4} \tilde{t}_i = T_s, \tilde{\boldsymbol{t}} \in \mathbb{R}^4\}\,.$$

Then, one step is taken from the initial point $\tilde{\boldsymbol{t}}_0$ in the steepest descent direction and projected onto the relaxed region, i.e., $\tilde{\boldsymbol{t}}_1 = P_{\Omega_0}(\tilde{\boldsymbol{t}}_0 - \boldsymbol{g}_0)$, where $P_{\Omega_0}(\boldsymbol{z})$ is the function that projects any vector $\boldsymbol{z}$ onto Ω_0. If the duration of an active vector in $\tilde{\boldsymbol{t}}_1$ is negative, the associated switching sequence is discarded. The projection $P_{\Omega_0}(\boldsymbol{z})$, is computed as

$$\underset{\tilde{\boldsymbol{\tau}} \in \Omega_0}{\text{minimize}} \quad \|\tilde{\boldsymbol{\tau}} - \boldsymbol{z}\|_2^2\,, \tag{5.23}$$

which can be easily solved by exploring its KKT conditions, i.e.,

$$\tilde{\boldsymbol{\tau}}^* - \boldsymbol{z} - \lambda^* \mathbf{1}_4 = \mathbf{0}\,, \tag{5.24a}$$

$$\sum_{i=1}^{4} \tilde{\tau}_i^* = T_s\,. \tag{5.24b}$$

Specifically, since (5.24a) can be written as $\tilde{\tau}_i^* = z_i + \lambda^*$, $i \in \{1,2,3,4\}$, by inserting it into (5.24b), the solution of (5.23) is given by $\lambda^* = (T_s - \sum_{i=1}^{4} z_i)/4$ and $\tilde{\boldsymbol{\tau}}^* = \lambda^* \mathbf{1}_4 + \boldsymbol{z}$. Hence, $\tilde{\boldsymbol{t}}_1$ can be found with a simple one-step projection, enabling a fast and accurate detection of unsuited switching sequences.
The validity of the described method is examined in simulation for both steady-state and transient operation for the drive system shown in Fig. 4.1 with the parameters given in Tables 5.1 and 5.2. Fig. 5.2(a) shows for one fundamental period the switching sequences $\boldsymbol{U}_z$, $z \in \{1,2,\ldots,6\}$, (see Table 4.1) considered as candidate solutions (shown as blue circles) by the

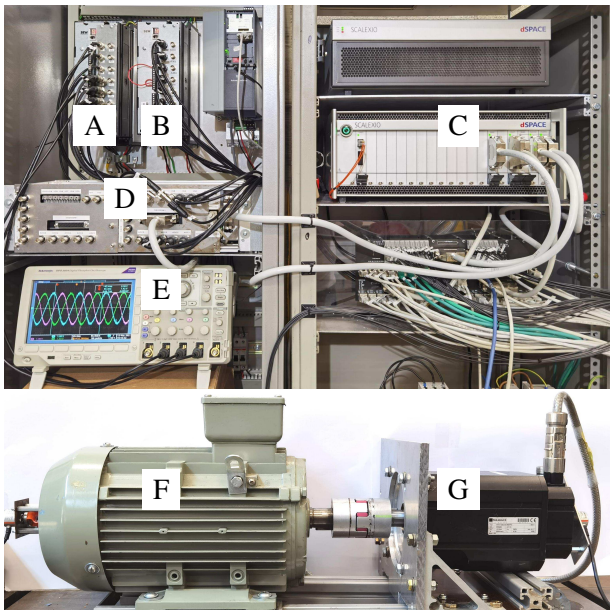

Figure 5.3: Experimental setup of the electrical drive test bench. A: SEW inverter for induction machine (IM), B: SEW inverter for load permanent magnet synchronous machine (PMSM), C: dSPACE SCALEXIO real-time control system, D: Interface, E: Oscilloscope, F: IM, G: PMSM.

aforementioned method in steady-state operation. In the same figure, the optimal switching sequence $\boldsymbol{U}^*$ found after solving all six QPs for all possible switching sequences is also indicated (shown with a red cross). Moreover, the same data are depicted in Fig. 5.2(b) for transient operation, namely for a torque reference step-down—from $T_{e,\mathrm{ref}} = 1$ to 0 per unit (p.u.)—and step-up—from $T_{e,\mathrm{ref}} = 0$ to 1 p.u.—change at $t = 4$ ms and $t = 13$ ms, respectively. As can be seen, the detection method selects one or two "suitable" switching sequences, with the globally optimal sequence always included.

5.2 Performance Evaluation for Two-Level Inverters with IM

The performance of the proposed direct MPC scheme is examined in the laboratory with a three-phase two-level inverter driving an IM, as shown in Fig. 4.1. The inverter is supplied by a stiff dc source. The real-time control platform is a dSPACE SCALEXIO system, consisting of a 4 GHz Intel XEON processor and a Xilinx Kintex-7 field-programmable gate array (FPGA). Two three-phase two-level SEW MDX inverters are used to control the IM and the load machine. The experimental setup is shown in Fig. 5.3. The rated values of the IM and the parameters of the system are given in Tables 5.1 and 5.2, respectively. Note that all results are shown in the p.u. system.

Table 5.1: Rated values of the induction machine.

Parameter	Symbol	SI Value
Rated voltage	V_R	380 V
Rated current	I_R	5.73 A
Rated stator frequency	f_{sR}	50 Hz
Rated rotor speed	ω_{mR}	2880 rpm
Rated power	P_R	3 kW

Table 5.2: System parameters in the SI and the p.u. system.

Parameter	SI (p.u.) symbol	SI (p.u.) value
Stator resistance	R_s (R_s)	$1.509\,\Omega$ (0.0394)
Rotor resistance	R_r (R_r)	$1.235\,\Omega$ (0.0323)
Stator leakage inductance	L_{ls} (X_{ls})	7.0 mH (0.0574)
Rotor leakage inductance	L_{lr} (X_{lr})	7.0 mH (0.0574)
Mutual inductance	L_m (X_m)	232.5 mH (1.9077)
Number of pole pairs	p	1
Dc-link voltage	$V_{\rm dc}$ ($V_{\rm dc}$)	$650\,V$ (2.0950)

5.2.1 Steady-State Operation

The steady-state performance of the drive system controlled by the direct MPC scheme is examined while the IM is operating at rated torque and nominal speed, i.e., the fundamental frequency is $f_1 = 50$ Hz, and the electromagnetic torque reference is set equal to $T_{e,\rm ref} = 1$ p.u., as shown in Fig. 5.4. Considering that the relationship between the switching frequency $f_{\rm sw}$ and the sampling interval T_s is given by

$$f_{\rm sw} = \frac{1}{2T_s}\,, \tag{5.25}$$

the sampling interval is chosen as $T_s = 123.4\,\mu$s so that a switching frequency $f_{\rm sw}$ of 4050 Hz results. Fig. 5.4(a) shows the three phase stator current measured by the oscilloscope with a sampling frequency of 50 kHz, while its harmonic spectrum is shown in Fig. 5.4(b). The current THD is 5.80%, relatively low considering the small total leakage reactance of 0.11 p.u. The current harmonics are mainly the sideband harmonics caused by the switching nature of the converter. Besides, some pronounced harmonics can be observed at low frequencies, especially around 1000 Hz, i.e., the $17^{\rm th}$ and $19^{\rm th}$ harmonic. Such harmonics are mainly caused by the slotting and saturation effects in the IM [56]. Finally, Figs. 5.4(c) and 5.4(d) show the stator flux magnitude and electromagnetic torque, respectively. These values are estimated in dSPACE, based on the machine model and the observer discussed in Chapter 2.

For comparison purposes, field-oriented control (FOC) with proportional-integral (PI) controllers and SVM is also implemented. The operating conditions and switching frequency are the same as those of direct MPC, while the PI parameters are tuned according to the modulus optimum method. As can be seen in Fig. 5.5(a), the stator current is very similar to that of the direct MPC scheme, but with a slightly higher ripple. This is reflected in the harmonic spec-

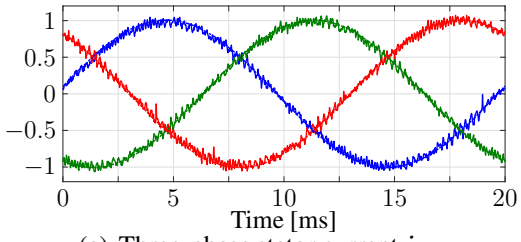

(a) Three-phase stator current $\boldsymbol{i}_{s,abc}$.

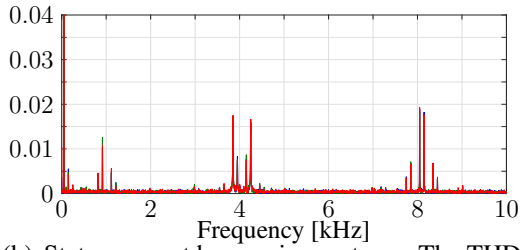

(b) Stator current harmonic spectrum. The THD is 5.80%.

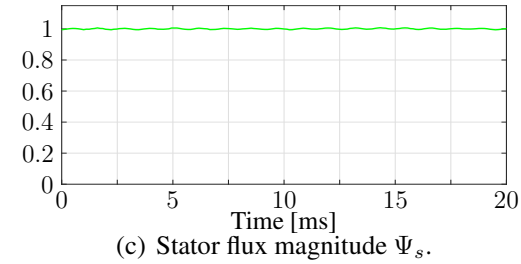

(c) Stator flux magnitude Ψ_s.

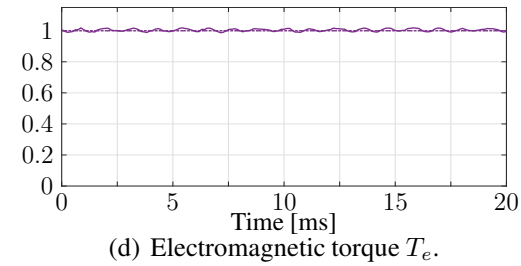

(d) Electromagnetic torque T_e.

Figure 5.4: Experimental results of direct MPC at steady-state operation, $f_{\text{sw}} = 4050\,\text{Hz}$.

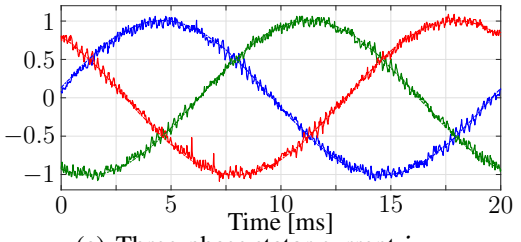

(a) Three-phase stator current $\boldsymbol{i}_{s,abc}$.

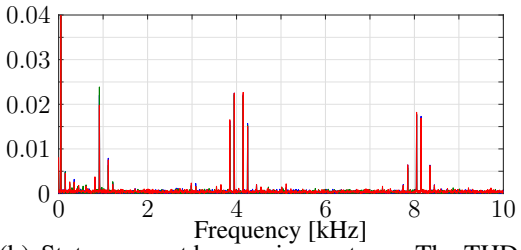

(b) Stator current harmonic spectrum. The THD is 6.18%.

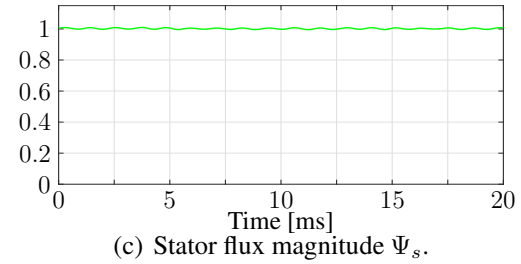

(c) Stator flux magnitude Ψ_s.

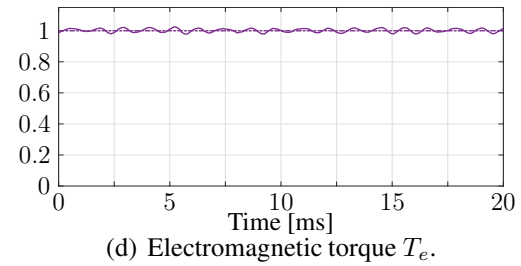

(d) Electromagnetic torque T_e.

Figure 5.5: Experimental results of FOC at steady-state operation, $f_{\text{sw}} = 4050\,\text{Hz}$.

trum (see Fig. 5.5(b)), where higher current distortions can be observed, with the current THD being equal to 6.19%. This is mainly due to fact that the harmonics caused by the slotting and saturation effects are more pronounced with FOC. This can be explained by the fact that the PI-based FOC has less control bandwidth so it cannot effectively remove these relatively high-order harmonics. Conversely, MPC can suppress—to some extent—those harmonics caused by the nonlinearities of the IM.

Furthermore, to gain more insight into how the direct MPC scheme manipulates the converter switch positions, the notion of the three-phase equivalent modulating signal $\boldsymbol{d}_{abc}$ is introduced. To this end, the single-phase equivalent modulating signal is defined as $d_x = T_{\text{on},x}/T_s$, with $x \in \{a, b, c\}$, where $T_{\text{on},x}$ is the time interval within one T_s that $u_x = 1$. The three-phase

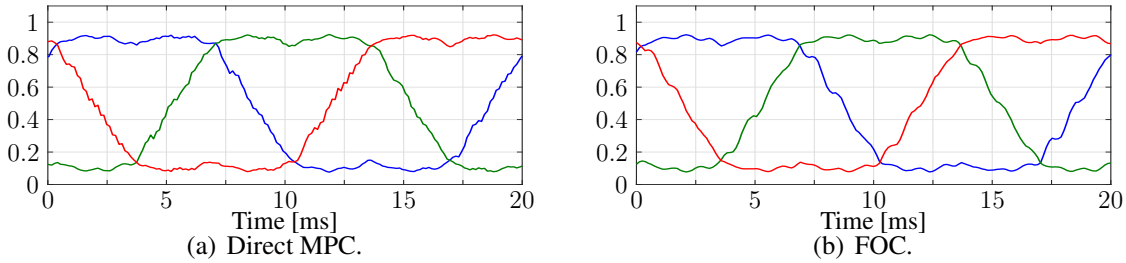

(a) Direct MPC. (b) FOC.

Figure 5.6: Three phase equivalent modulating signal of direct MPC and modulating signal of FOC at nominal steady-state operation, $f_{\text{sw}} = 4050\,\text{Hz}$.

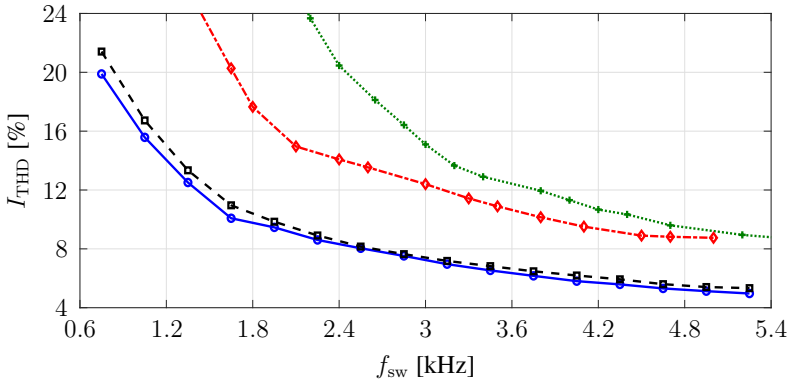

Figure 5.7: Trade-off between current THD and switching frequency for the proposed direct MPC (blue, solid line), FOC (black, dashed line), FCS-MPC1 (green, dotted line), and FCS-MPC2 (red, dash-dotted line).

equivalent modulating signal is shown in Fig. 5.6 for the proposed MPC scheme. In the same figure the modulating signal of FOC with SVM is depicted. As can be observed in Fig. 5.6, the direct MPC scheme, although it does not employ a modulator, achieves a very similar equivalent modulating signal.

Finally, to further elucidate the performance of the proposed controller, Fig. 5.7 depicts the current THD for switching frequencies in the range $f_{\text{sw}} \in [750, 5250]\,\text{Hz}$. As before, the current THD produced by FOC is also shown. Moreover, to clearly highlight the benefits of the proposed direct MPC strategy, the current THD achieved with two conventional FCS-MPC methods is also reported. Specifically, the first FCS-MPC method (referred to as FCS-MPC1) has the objective function

$$J = \|\boldsymbol{i}_{s,\text{ref}}(k+1) - \boldsymbol{i}_s(k+1)\|_1\,,$$

i.e., it does not penalize the control action and uses the ℓ_1-norm, while the switching frequency is adjusted by modifying the sampling interval T_s. The objective function of the second FCS-MPC method (FCS-MPC2) is based on the ℓ_2-norm, penalizes the control effort, and uses the sampling interval $T_s = 50\,\mu\text{s}$, i.e.,[3]

$$J = \|\boldsymbol{i}_{s,\text{ref}}(k+1) - \boldsymbol{i}_s(k+1)\|_2^2 + \lambda_u \|\Delta \boldsymbol{u}_{abc}(k)\|_2^2\,.$$

[3]The reader is referred to [8] for insights into the discussed designs of FCS-MPC.

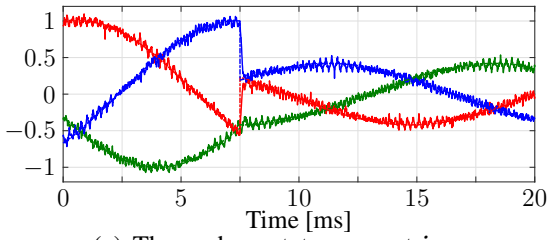

(a) Three-phase stator current $\boldsymbol{i}_{s,abc}$.

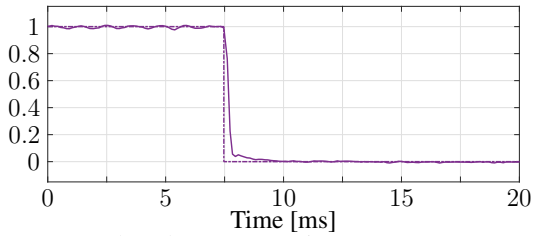

(b) Electromagnetic torque T_e.

Figure 5.8: Experimental results of direct MPC during a torque reference step-down transient.

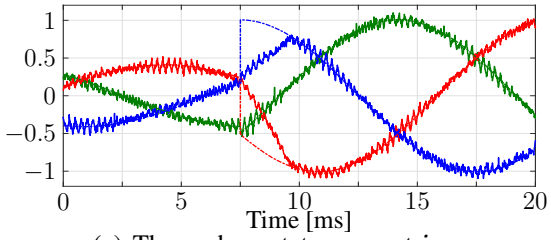

(a) Three-phase stator current $\boldsymbol{i}_{s,abc}$.

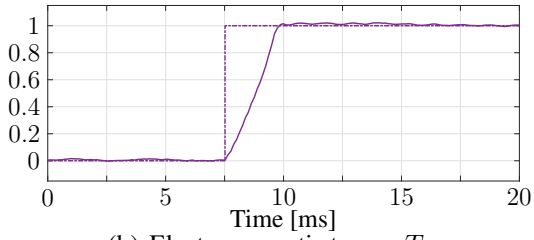

(b) Electromagnetic torque T_e.

Figure 5.9: Experimental results of direct MPC during a torque reference step-up transient.

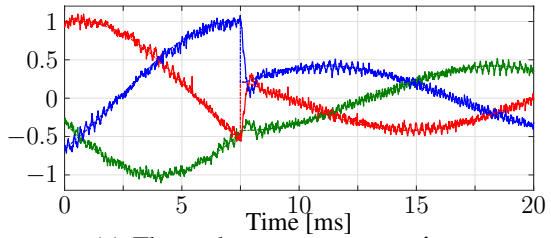

(a) Three-phase stator current $\boldsymbol{i}_{s,abc}$.

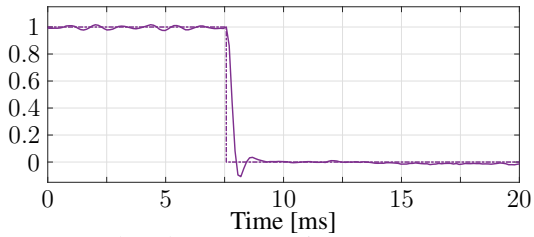

(b) Electromagnetic torque T_e.

Figure 5.10: Experimental results of FOC during a torque reference step-down transient.

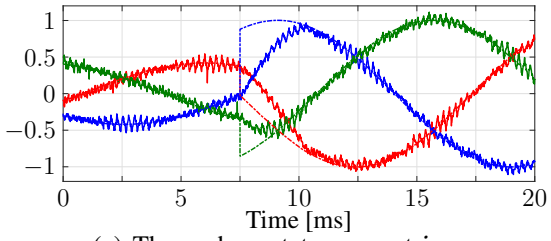

(a) Three-phase stator current $\boldsymbol{i}_{s,abc}$.

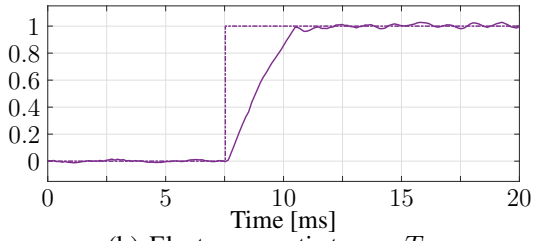

(b) Electromagnetic torque T_e.

Figure 5.11: Experimental results of FOC during a torque reference step-up transient.

As can be seen, Fig. 5.7 clearly shows the superior steady-state performance of the proposed direct MPC scheme since it achieves the lowest values of current THD I_{THD} over the whole range of the examined switching frequencies.

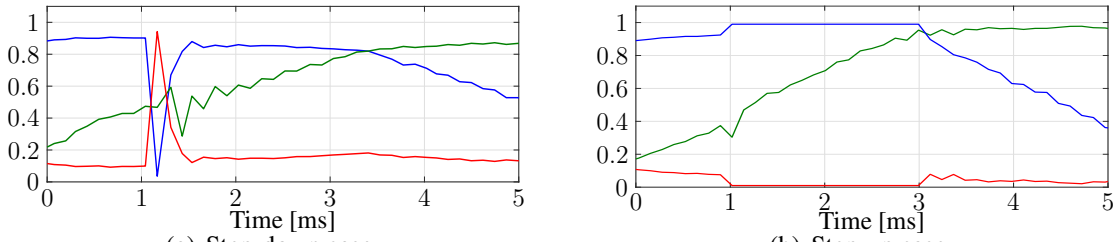

(a) Step-down case. (b) Step-up case.

Figure 5.12: Three-phase equivalent modulating signal of direct MPC at torque reference steps.

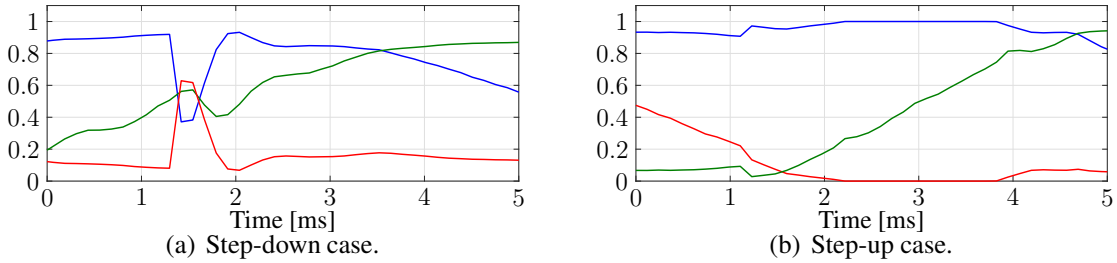

(a) Step-down case. (b) Step-up case.

Figure 5.13: Three-phase modulating signals of FOC at torque step reference steps.

5.2.2 Transient Behavior

While operating at the same switching frequency as before (i.e., $f_{\mathrm{sw}} = 4050\,\mathrm{Hz}$), the transient behavior of the examined direct MPC scheme is tested during torque reference steps from $T_{e,\mathrm{ref}} = 1$ to $0\,\mathrm{p.u.}$ as well as from $T_{e,\mathrm{ref}} = 0$ to $1\,\mathrm{p.u.}$. These cases are shown in Figs. 5.8 and 5.9, respectively. As a comparison, Figs. 5.10 and 5.11 show the performance of FOC for the same scenarios. For the torque reference step-down case, the proposed direct MPC scheme smoothly regulates the current—and thus the torque—to the new reference within two sampling intervals, without any over- and/or undershoots, see Fig. 5.8. FOC, on the other hand, suffers from a visible undershoot in the torque, see Fig. 5.10. As for the torque reference step-up case, the proposed direct MPC strategy achieves a significantly faster settling time of about $2\,\mathrm{ms}$ as compared to the $3\,\mathrm{ms}$ required by FOC, see Figs. 5.9 and 5.11, respectively.

For more insight into the dynamic behavior of the presented direct MPC algorithm, Fig. 5.12 shows the equivalent modulating signal during the torque reference step changes in detail. In a same fashion, Fig. 5.13 depicts the modulating signal with FOC. At the torque reference step-down case, the direct MPC method instantly pushes the application times of the switch positions close to their limits and reverses the polarity of the equivalent modulating signal, see Fig. 5.12(a), so that the converter applies the switch positions that result in as fast a response as possible for the optimal amount of time. As for the torque step-up case, the MPC strategy fully utilizes the available dc-link voltage (see Fig. 5.12(b)) so that the settling time is only limited by the physical limits of the system. We conclude that the proposed direct MPC algorithm inherits the favorable dynamic behavior that characterizes direct control schemes. As for the PI-based FOC, it also tries to reverse the polarity of the modulating signal during the step-down scenario, but it does not manage to do it as aggressively as MPC, see Fig. 5.13(a). Moreover, during the step-up case, shown in Fig. 5.13(b), FOC tries to fully utilize the available dc-link voltage. In doing so, the modulating signal is saturated due to the employed anti-windup mech-

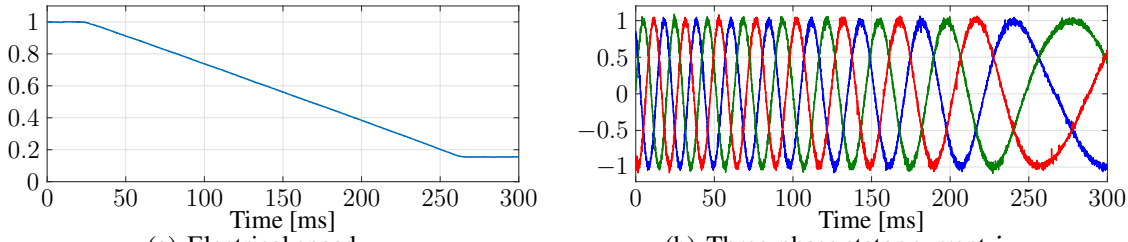

(a) Electrical speed ω_s. (b) Three-phase stator current $\boldsymbol{i}_{s,abc}$.

Figure 5.14: Speed reference ramp (from 1 to 0.15 p.u.) with direct MPC.

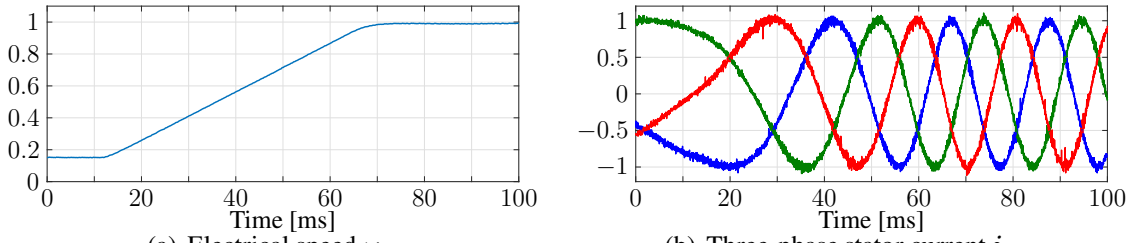

(a) Electrical speed ω_s. (b) Three-phase stator current $\boldsymbol{i}_{s,abc}$.

Figure 5.15: Speed reference ramp (from 0.15 to 1 p.u.) with direct MPC.

anism with saturation, but in a less aggressive manner due to the integrating element of the controller. Moreover, due to the fact that the controller (i.e., FOC) and modulator (i.e., SVM) are two decoupled entities that act independently from each other, the best possible dynamic performance is not guaranteed because the voltage synthesized by SVM is different from the voltage commanded by FOC [57]. As a result, the dynamics of FOC are slower, as also shown in Fig. 5.11.

Another scenario for evaluating the transient behavior of a controller is operation under speed changes. Since the focus of this work is on the inner current control loop designed in the framework of MPC, the load machine is used to impose a speed ramp of around 0.85 p.u., while keeping the current reference of the IM constant. As shown in Figs. 5.14 and 5.15, the MPC algorithm achieves good reference current tracking during these speed ramps.

5.2.3 Computational Burden

The main computational burden of the direct MPC scheme relates to the solution of the QP problem(s). Table 5.3 summarizes the average and maximum number of iterations n_{it} required by the proposed QP algorithm to conclude to the optimal solution of one QP, along with the corresponding turnaround time $t_{\mathrm{ta,QP}}$ on dSPACE. In the same table, the turnaround time of the whole control scheme $t_{\mathrm{ta,tot}}$ is also shown. This time includes, besides the time required to solve the QP(s), the time needed for the analog-to-digital conversion (ADC), the uplink and downlink communication as well as the generation of the gating signals. As can be seen, the average number of iterations to solve one QP is 39.7 and the maximum 98. Considering that the optimization variable $\tilde{\boldsymbol{t}}$ of each QP problem is eight-dimensional, while eight boundary conditions exist along with two equality constrains, the required number of iterations is modest. Moreover, since each iteration of the proposed QP algorithm requires little computational effort, the maximum turnaround time of the proposed QP algorithm, i.e., $t_{\mathrm{ta,QP}}$, is as little as $42.6\,\mu$s.

Table 5.3: Number of iterations required by the QP algorithm and the turnaround times on dSPACE, where $t_{\mathrm{ta,QP}}$ corresponds to solving one QP, and $t_{\mathrm{ta,tot}}$ to executing the whole control algorithm.

	Number of iterations n_{it}	Turnaround time $t_{\mathrm{ta,QP}}$ (µs)	Turnaround time $t_{\mathrm{ta,tot}}$ (µs)
Average	39.7	16.9	28.7
Maximum	98	42.6	71.3

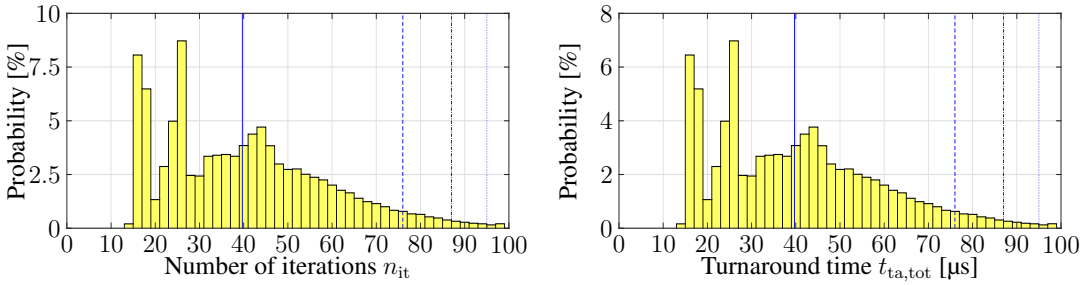

(a) Probability distribution of the number of iteration steps required by the QP algorithm.

(b) Probability distribution of the turnaround time $t_{\mathrm{ta,tot}}$.

Figure 5.16: Probability distribution of the number of iteration steps required by the QP algorithm and the turnaround time $t_{\mathrm{ta,tot}}$. The average number of iterations is indicated by the solid vertical line. The 95, 98, and 99 percentiles are shown as dashed, dashed-dotted, and dotted vertical lines, respectively.

Table 5.4: The maximum turnaround time $t_{\mathrm{ta,max}}$ of the four discussed control algorithms running on dSPACE.

	FOC	FCS-MPC1	FCS-MPC2	Direct MPC
Turnaround time $t_{\mathrm{ta,max}}$ (µs)	16.6	16.9	17.1	71.3

Furthermore, since the unsuited switching sequences can be effectively detected with only a few computations, the maximum turnaround time of the whole control scheme, i.e., $t_{\mathrm{ta,tot}}$, is only 71.3 µs. In addition, the probability distribution of the number of iterations n_{it} and the turnaround time $t_{\mathrm{ta,tot}}$ are shown in Figs. 5.16(a) and 5.16(b), respectively. As shown, in more than 98% cases, the turnaround time $t_{\mathrm{ta,tot}}$ is less than 50 µs. This indicates that the proposed QP solver manages to solve the necessary number of QPs in real time very quickly and within the available time, as defined by the chosen sampling interval of $T_s = 123.4$ µs, thanks the fast projection algorithm and the BB method discussed in Section 5.1.

Finally, the maximum (i.e., worst-case scenario) turnaround times $t_{\mathrm{ta,max}}$ of the four discussed control algorithms, i.e., the proposed direct MPC scheme, FOC, FCS-MPC1 and FCS-MPC2, are summarized in Table 5.4. As can be seen, the superior performance of the proposed algorithm comes at a cost of increased computational demands. It is worth mentioning, however, that, if needed, the turnaround time of the proposed control scheme can be significantly reduced, e.g., by decreasing the horizon to one step and/or by manipulating the maximum number of iteration steps, as can be deduced from Fig. 5.16(a). Nevertheless, such a reduction in the com-

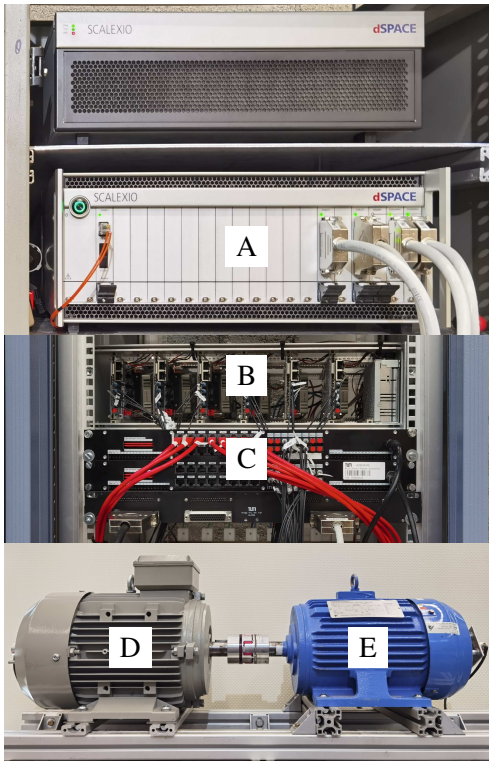

Figure 5.17: Setup of the electrical drives test bench. A: dSPACE SCALEXIO real-time control system, B: Back-to-back 3L-NPC converters, C: Interface, D: IM, E: PMSM

Table 5.5: Rated values of the induction machine.

Parameter	Symbol	SI Value
Rated voltage	V_R	400 V
Rated current	I_R	8.73 A
Rated stator frequency	f_{sR}	50 Hz
Rated rotor speed	ω_{mR}	1430 rpm
Rated power	P_R	4 kW

putational cost would occur at the expense of performance, i.e., a somewhat increased stator current THD.

5.3 Performance Evaluation for 3L-NPC Inverters with IM

The performance of the proposed direct MPC scheme is examined in the laboratory with a three-phase 3L-NPC inverter driving an IM, as shown in Fig. 4.5. The inverter is supplied by a stiff dc source and the NP is floating. The real-time control platform is a dSPACE SCALEXIO system, consisting of a 4 GHz Intel XEON processor and a Xilinx Kintex-7 field-programmable gate array (FPGA). The controller is implemented on the processor, and the data acquisition and generation of the switching signals are done on the FPGA. The experimental setup is shown in

Table 5.6: System parameters in the SI and the p.u. system.

Parameter	SI (p.u.) symbol	SI (p.u.) value
Stator resistance	R_s (R_s)	$2.94\,\Omega$ (0.11)
Rotor resistance	R_r (R_r)	$0.67\,\Omega$ (0.024)
Stator leakage inductance	L_{ls} (X_{ls})	8.45 mH (0.096)
Rotor leakage inductance	L_{lr} (X_{lr})	8.45 mH (0.096)
Mutual inductance	L_m (X_m)	195.25 mH (2.26)
Number of pole pairs	p	2
Dc-link voltage	V_{dc} (V_{dc})	650 V (1.99)
Dc-link capacitance	C_{dc} (X_{dc})	1.6 mF (13.43)

Fig. 5.17. The rated values of the IM and the parameters of the system are given in Tables 5.5 and 5.6, respectively. For the examined scenarios, the weighting matrices are chosen as $\boldsymbol{Q} = \mathrm{diag}(1, 1, 5)$ and $\boldsymbol{\Lambda} = \mathrm{diag}(10, 10, 10)$. Finally, all results are shown in the p.u. system.

5.3.1 Steady-State Operation

The steady-state performance throughout this section is examined while the IM is operating at nominal speed and rated torque, implying a fundamental frequency of $f_1 = 50\,\mathrm{Hz}$ and electromagnetic torque $T_e = 1$ p.u. Moreover, the sampling frequency is chosen as $f_s = 2700\,\mathrm{Hz}$ such that a device switching frequency of $f_{\mathrm{sw}} = 700\,\mathrm{Hz}$ results.[4]

Fig. 5.18 shows the performance of the drive system controlled by the proposed direct MPC. As shown in 5.18(a), the three-phase stator current $\boldsymbol{i}_{s,abc}$, measured by an oscilloscope with a sampling frequency of $50\,\mathrm{kHz}$, tracks its reference with no steady-state error and low harmonic distortions. The stator current harmonic spectrum is shown in 5.18(b), while the total harmonic distortion (THD) is 3.60%, which is relatively low for a low-voltage machine at the examined switching frequency. In addition, the harmonic power is mainly concentrated at the odd non-triplen multiples of the fundamental frequency, which are caused by the switching nature of the inverter. Besides, some low-frequency harmonics can also be observed, which are caused by the slotting and saturation effects in the IM. Moreover, the NP potential of the inverter is well balanced, with the deviation being kept always within 3%, as shown in Fig. 5.18(d).

For comparison purposes, FOC with PI controllers and CB-PWM is also implemented. The CB-PWM is with asymmetric sampling and a suitable common-mode signal is injected to achieve equivalence with SVM [17]. As for the parameters of the PIs, they are tuned according to the modulus optimum method [58]. Furthermore, the NP potential is balanced by manipulating the CMV in the three-phase modulation signal. The CMV reference is generated by a simple PI-based closed-loop controller presented in [32]. The operating conditions, sampling frequency, and thus switching frequency, are the same as those of direct MPC. As shown in Fig. 5.19,

[4]The proposed direct MPC method ensures that there is one switching transition in each phase leg per T_s. This means that T_s is akin to the modulation half-cycle of CB-PWM/SVM. Considering a three-level NPC converter, this implies that there are $T_1/(2T_s) + 1$ switching transitions in one fundamental period T_1. As two consecutive switching transitions give rise to one pulse, the switching frequency relates to T_s (f_s) according to $f_{\mathrm{sw}} = 1/(4T_s) + 1/(2T_1) = f_s/4 + f_1/2$.

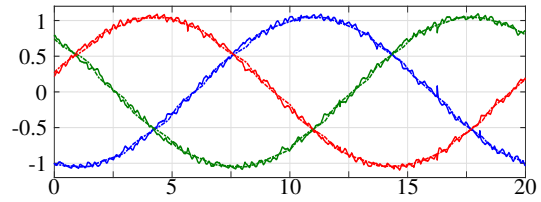

(a) Three-phase stator current $\boldsymbol{i}_{s,abc}$.

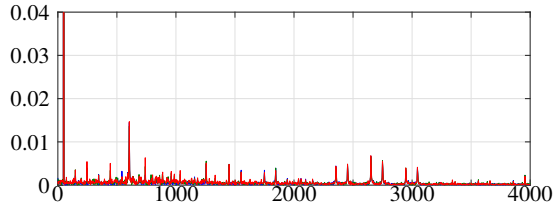

(b) Stator current harmonic spectrum (THD = 3.60%).

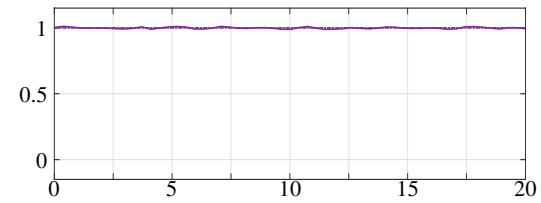

(c) Electromagnetic torque.

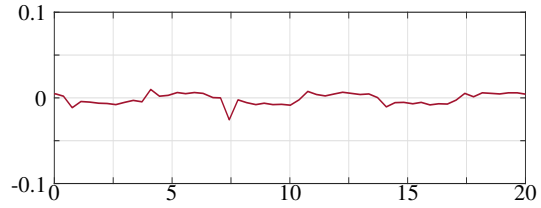

(d) The neutral point potential v_n.

Figure 5.18: Experimental results of direct MPC at steady-state operation, $f_{\mathrm{sw}} = 700\,\mathrm{Hz}$.

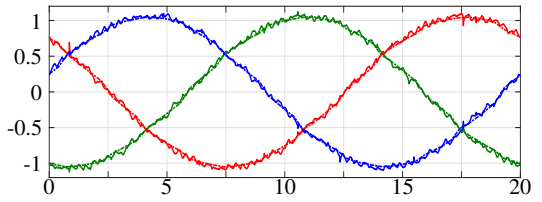

(a) Three-phase stator current $\boldsymbol{i}_{s,abc}$.

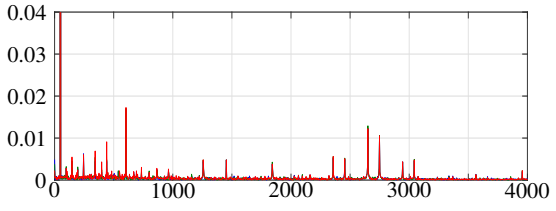

(b) Stator current harmonic spectrum (THD = 3.81%).

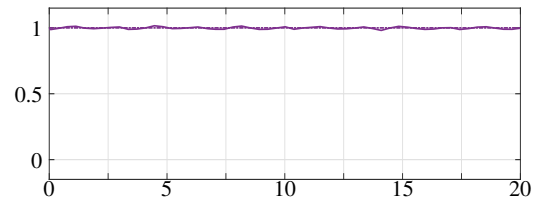

(c) Electromagnetic torque.

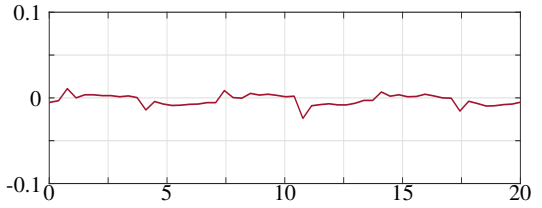

(d) The neutral point potential v_n.

Figure 5.19: Experimental results of FOC at steady-state operation, $f_{\mathrm{sw}} = 700\,\mathrm{Hz}$.

FOC achieves very similar steady-state performance, i.e., the three-phase stator current tracks its reference accurately and the NP potential is well balanced. However, the stator current has a slightly higher ripple especially of low frequency, as shown in Fig. 5.19(b), resulting in a slightly increased THD, i.e., 3.81% compared to 3.60% of the direct MPC scheme. This can be explained by the fact that the linear PI controllers of FOC cannot quickly compensate for the disturbance caused by the NP potential ripple and the nonlinear effects in the IM, e.g., slotting and saturation effects. As a result, low-frequency harmonics (e.g., from 5^{th} and up to 13^{th}) are pronounced in the harmonic spectrum of FOC. In contrast, the direct MPC strategy, thanks to its high control bandwidth, can effectively suppress these harmonics caused by the floating NP and the nonlinear effects of the IM.

Furthermore, the three-phase switch position $\boldsymbol{u}_{abc}$ generated by direct MPC and FOC is shown

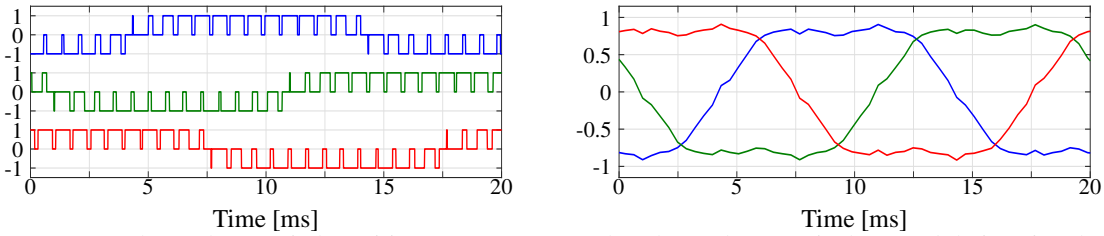

(a) Three-phase switch position. (b) Three-phase equivalent modulating signal.

Figure 5.20: Three-phase switch position and equivalent modulating signal of direct MPC at steady state, $f_{\text{sw}} = 700\,\text{Hz}$.

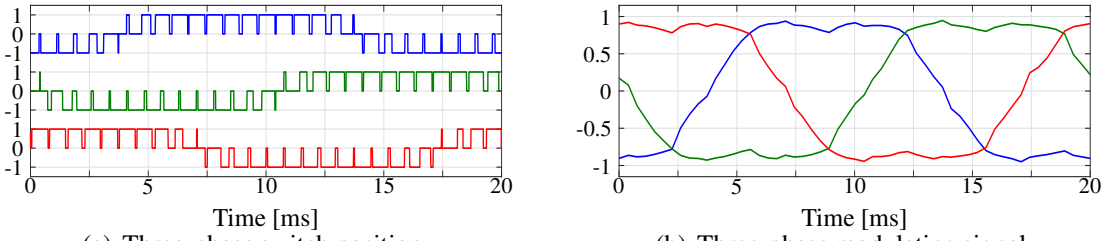

(a) Three-phase switch position. (b) Three-phase modulating signal.

Figure 5.21: Three-phase switch position and modulating signal of FOC at steady state, $f_{\text{sw}} = 700\,\text{Hz}$.

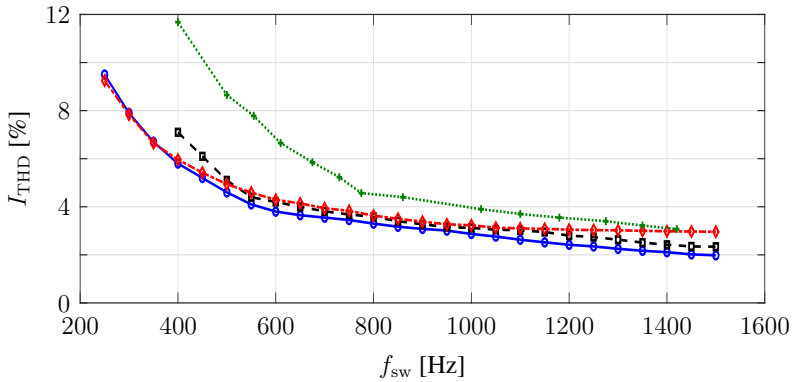

Figure 5.22: Trade-off between current THD and switching frequency for the proposed direct MPC (blue, solid line), FOC (black, dashed line), FCS-MPC1 (green, dotted line), and FCS-MPC2 (red, dash-dotted line).

in Figs. 5.20(a) and 5.21(a), respectively. As shown, direct MPC yields a very similar switching pattern as that of FOC with SVM in steady-state operation, i.e., each phase switches one level up or down within one T_s, although there is no explicit modulation stage. The latter implies that there is no modulating signal in direct MPC. However, to provide more insight into the workings of the proposed algorithm, we introduce the variable $\bar{\boldsymbol{u}}_{abc} = (\sum_{i=0}^{3} \boldsymbol{u}_{abc}(t_i)\tilde{t}_i)/T_s$, where $\tilde{t}_i = t_{i+1} - t_i$, with $i \in \{0, 1, 2, 3\}$ and $t_4 = T_s$, which can be interpreted as an equivalent modulating signal. As can be seen in Figs. 5.20(b) and 5.21(b), the equivalent modulating signal of the direct MPC scheme is similar to the modulating signal of FOC with SVM. It is worth noting that $\bar{\boldsymbol{u}}_{abc}$ has the shape of a modulating signal injected with a CMV signal. This is an inherent feature of the proposed method as no external signals are injected to the output of

the MPC algorithm.
Finally, the tradeoff curves between the current THD and the switching frequency for direct MPC and FOC are shown in Fig. 5.22. Moreover, two conventional FCS-MPC methods are also implemented for comparison purposes. Specifically, the first FCS-MPC method (referred to as FCS-MPC1) has the objective function

$$J = \|\boldsymbol{i}_{s,\mathrm{ref}}(k+1) - \boldsymbol{i}_s(k+1)\|_1 + \lambda_{v_n}|v_{n,\mathrm{ref}}(k+1) - v_n(k+1)|\,,$$

i.e., it does not penalize the switching effort and uses the ℓ_1-norm, while the switching frequency is adjusted by modifying the sampling interval T_s. The objective function of the second FCS-MPC method (FCS-MPC2) is based on the ℓ_2-norm, and penalizes the control effort, i.e.,[5]

$$\begin{aligned} J =& \|\boldsymbol{y}_{s,\mathrm{ref}}(k+1) - \boldsymbol{y}_s(k+1)\|_2^2 + \\ & \lambda_{v_n}(v_{n,\mathrm{ref}}(k+1) - v_n(k+1))^2 + \lambda_u\|\Delta\boldsymbol{u}_{abc}(k)\|_2^2\,. \end{aligned}$$

For this method the sampling frequency is set equal to $f_s = 16\,\mathrm{kHz}$, while the switching frequency is adjusted by tuning the weighting factor λ_u in the objective function.
As can be seen from Fig. 5.22, FCS-MPC1 yields the worst steady-state performance over the whole range of the examined switching frequencies. Moreover, both the proposed direct MPC and FOC achieve lower current THD than FCS-MPC2 for $f_{\mathrm{sw}} \in [550, 1550]\,\mathrm{Hz}$. For FCS-MPC2 to achieve lower values of THD much higher sampling frequencies would be required which would render its real-time implementation challenging [8]. Hence, these results demonstrate the advantages of the proposed control method as it is suitable for a wider range of switching frequencies. This observation is also supported by the fact that the presented algorithm outperforms FOC over the whole range of switching frequencies. Moreover, as can be seen, at the low switching frequency range ($f_{\mathrm{sw}} < 550\,\mathrm{Hz}$), the current THD of FOC increases significantly as f_{sw} decreases, while FOC becomes unstable at $f_{\mathrm{sw}} < 400\,\mathrm{Hz}$. This is in stark contrast with the performance of the proposed direct MPC scheme and FCS-MPC2, which still produce relatively low current THD at such low switching frequencies.

5.3.2 Performance During Transients

The transient behavior of the proposed direct MPC is tested by commanding the torque reference to step from $T_{e,\mathrm{ref}} = 1$ to $0\,\mathrm{p.u.}$, and from $T_{e,\mathrm{ref}} = 0$ to $1\,\mathrm{p.u.}$, while operating at the same switching frequency as before, i.e., $f_{\mathrm{sw}} = 700\,\mathrm{Hz}$. As shown in Fig. 5.23, where the torque reference step-down scenario is depicted, the direct MPC scheme quickly regulates the current—and thus the torque—to their new references, within around $2\,\mathrm{ms}$, while keeping the NP potential well balanced. Such a favorable behavior can be achieved due to the polarity reversal of the deadbeat solution $\boldsymbol{v}^*_{\mathrm{db},abc}$ at the beginning of the transient. As a result, the switch position $\boldsymbol{u}_{abc}(t_0)$ at the beginning of the transient is adjusted to reflect this change. In doing so, such switch positions and corresponding switching times are computed that result in the shortest settling time possible. This point is clearly shown in Fig. 5.23(e), where the three-phase switch position is depicted during the transient. Moreover, the equivalent modulating signal illustrated in Fig. 5.23(d) further highlights this behavior. In comparison, the performance of FOC under

[5]The reader is referred to [8] for insights into the discussed designs of FCS-MPC.

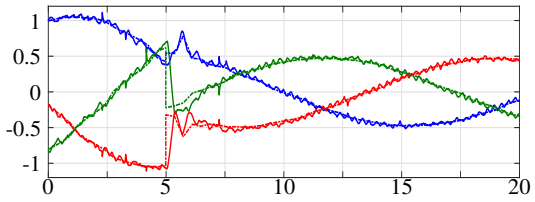

(a) Three-phase stator current $\boldsymbol{i}_{s,abc}$.

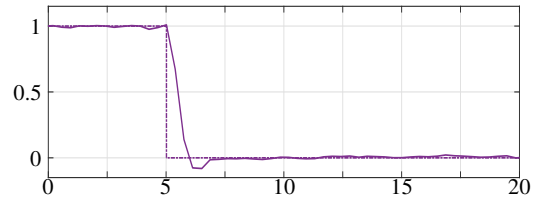

(b) Electromagnetic torque.

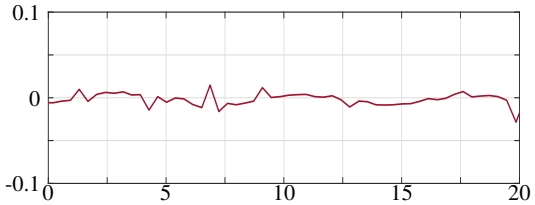

(c) The neutral point potential v_n.

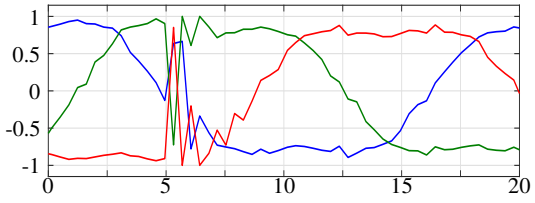

(d) Three-phase equivalent modulating signal.

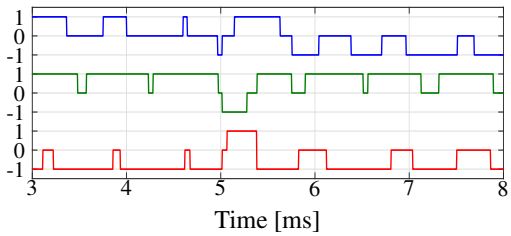

(e) Three-phase switch position (zoomed in at transient).

Figure 5.23: Experimental results of direct MPC at a torque reference step-down transient.

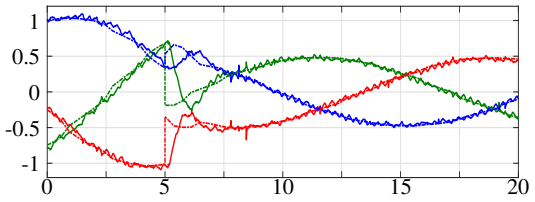

(a) Three-phase stator current $\boldsymbol{i}_{s,abc}$.

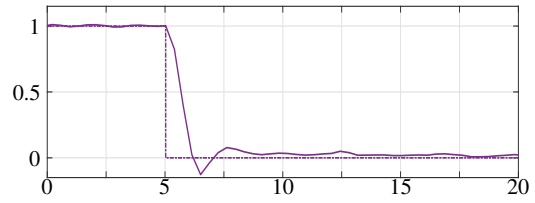

(b) Electromagnetic torque.

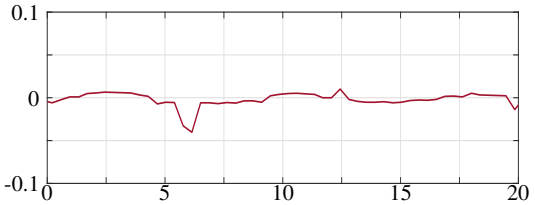

(c) The neutral point potential v_n.

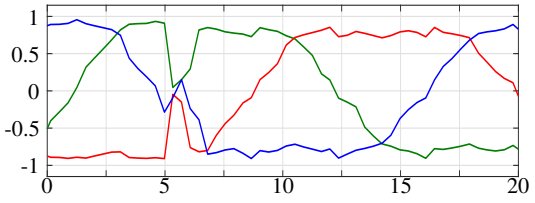

(d) Three-phase equivalent modulating signal.

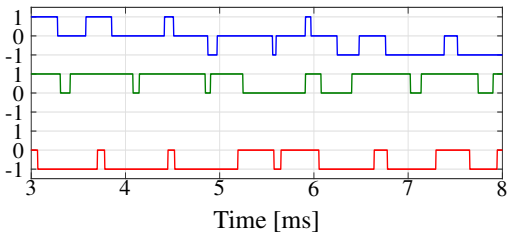

(e) Three-phase switch position (zoomed in at transient).

Figure 5.24: Experimental results of FOC at a torque reference step-down transient.

the same scenario is not as good, see Fig. 5.24. As can be seen, FOC takes a significantly longer time (around 4 ms) to settle to the new operating point, due to the fact that the available

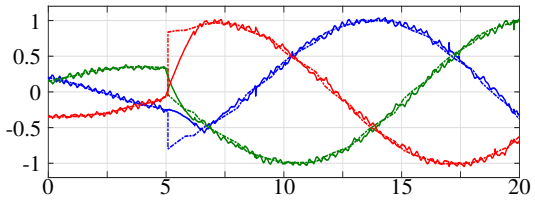

(a) Three-phase stator current $\boldsymbol{i}_{s,abc}$.

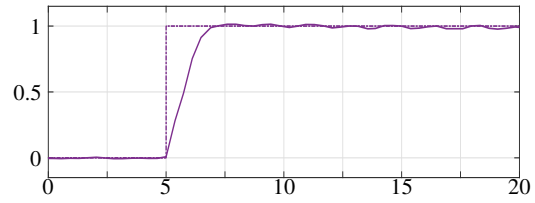

(b) Electromagnetic torque.

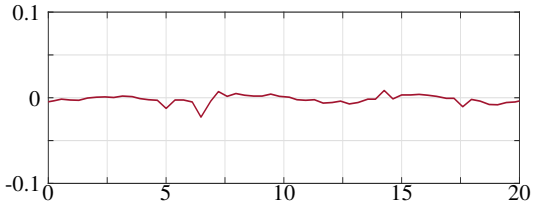

(c) The neutral point potential v_n.

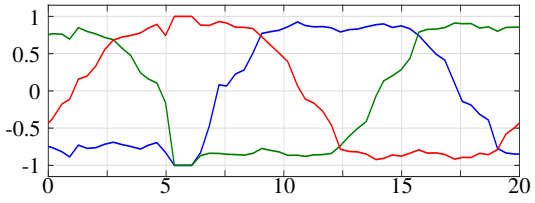

(d) Three-phase equivalent modulating signal.

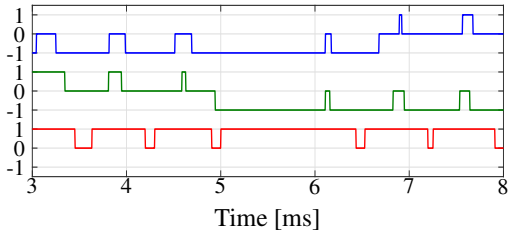

(e) Three-phase switch position (zoomed in at transient).

Figure 5.25: Experimental results of direct MPC at a torque reference step-up transient.

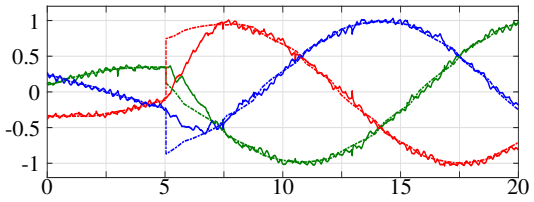

(a) Three-phase stator current $\boldsymbol{i}_{s,abc}$.

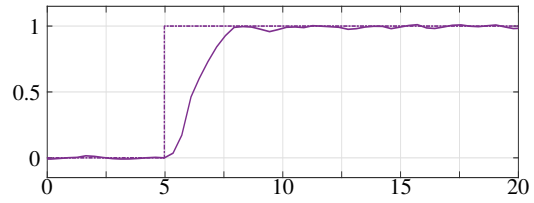

(b) Electromagnetic torque.

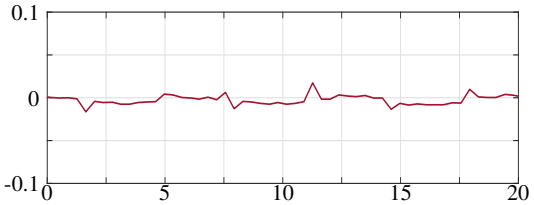

(c) The neutral point potential v_n.

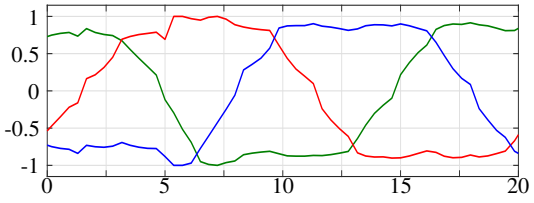

(d) Three-phase equivalent modulating signal.

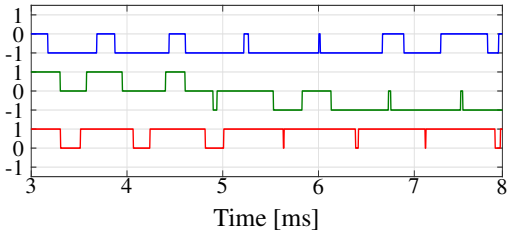

(e) Three-phase switch position (zoomed in at transient).

Figure 5.26: Experimental results of FOC at a torque reference step-up transient.

dc-link voltage is underutilized, as a polarity reversal is not achieved. Besides, a spike on the NP potential can be observed during the transient, see Fig. 5.24(c).

As for the torque reference step-up change, direct MPC pushes the switching instants to the

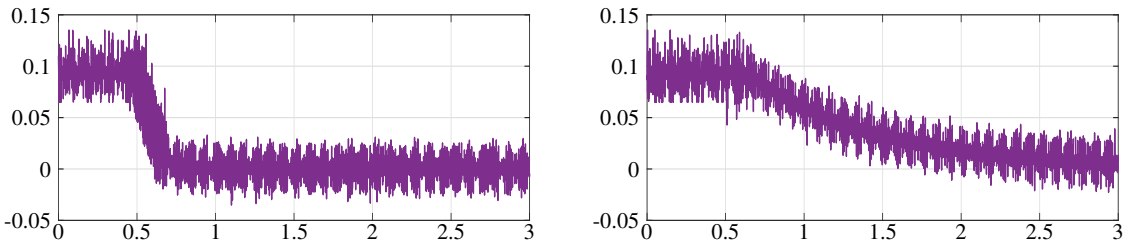

(a) Proposed direct MPC. (b) Natural balancing.

Figure 5.27: NP potential balancing.

limits, i.e., at the beginning or end of each T_s, such that only the switch position (i.e., $\boldsymbol{u}_{abc}(t_0)$ or $\boldsymbol{u}_{abc}(t_3)$) that regulates the current and torque to their new references as fast as possible is applied for the whole sampling interval, see Fig. 5.25. By doing so, the available dc-link voltage is fully utilized, and the settling time is only limited by the physical limits of the system. In contrast, FOC cannot push the modulating signal immediately to the maximum limit due to its relatively low bandwidth limited by the integrating element in the controller. As a result, the direct MPC scheme achieves a significantly faster settling time of about $2\,\mathrm{ms}$, which is almost half of that required by FOC, see Fig. 5.26.

5.3.3 Neutral Point Potential Balancing

To further verify the active NP balancing capability of the proposed direct MPC strategy, the drive system is tested at nominal speed but with no mechanical load, i.e., there is only magnetizing current. This working condition is recognized as a critical one for 3L-NPC inverters [32,59]. For this test a $0.1\,\mathrm{p.u.}$ offset is initially introduced to the NP potential. As can be seen, direct MPC regulates the NP potential quickly to zero within around $0.2\,\mathrm{s}$, see Fig. 5.27(a). On the other hand, FOC cannot exhibit such a favorable balancing property. This is due to the fact that the PI-based NP controller in FOC tends to become unstable under no-load conditions [32]. For this reason, it is typical to disable the NP controller at zero PF such that natural balancing mechanism of the NP potential is enabled [60]. As shown in Fig. 5.27(b), the NP potential balancing is achieved in about $2\,\mathrm{s}$ under such conditions. This time is one order of magnitude longer than that required by the presented direct MPC scheme. These results clearly demonstrate the advantages of the inherent active NP potential balancing capability of the proposed control method.

5.3.4 Computational Burden

The main challenge of the real-time implementation of the direct MPC scheme is the relatively high computational burden caused by solving the QP problems. Thanks to the efficient projection algorithm developed in [26], and its refinement based on the fast Nesterov gradient method [54], the computational burden is kept modest. To quantify this, Fig. 5.28(a) shows the probability distribution of the number of iteration steps n_{it} required by the developed QP solver to find the solution. As can be seen, at most 15 iterations are required. To further elucidate this point, Fig. 5.28(b) depicts the turnaround time $t_{\mathrm{ta,tot}}$ of the whole direct MPC scheme in

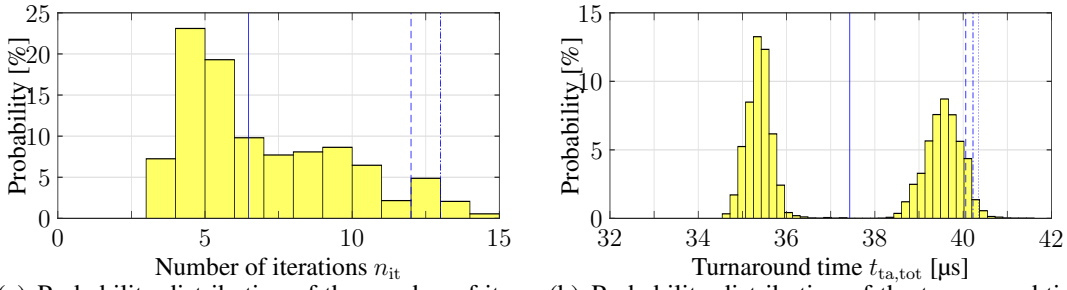

(a) Probability distribution of the number of iteration steps required by the QP algorithm.

(b) Probability distribution of the turnaround time $t_{\mathrm{ta,tot}}$.

Figure 5.28: Probability distribution of the number of iteration steps required by the QP algorithm and the turnaround time $t_{\mathrm{ta,tot}}$. The average number of iterations is indicated by the solid vertical line. The 95, 98, and 99 percentiles are shown as dashed, dashed-dotted, and dotted vertical lines, respectively.

Table 5.7: The average/maximum turnaround time $t_{\mathrm{ta,ave}}/t_{\mathrm{ta,max}}$ of the four discussed control algorithms running on dSPACE.

Turnaround time	FOC	FCS-MPC1	FCS-MPC2	Direct MPC
average $t_{\mathrm{ta,ave}}$ (µs)	15.2	16.4	16.5	37.4
max $t_{\mathrm{ta,max}}$ (µs)	18.2	19.6	19.8	41.6

the dSPACE. As can be seen, the probability distribution of the turnaround time $t_{\mathrm{ta,tot}}$ is concentrated mainly around two locations, depending on whether one or two QPs are solved in real time. The number of QPs solved depends on the geometry of the underlying optimization problem and the ability of the solver to exclude suboptimal solutions at a very early stage. Nevertheless, in the worst-case scenario, only two QPs need to be solved, thus greatly alleviating the computational complexity of the proposed optimal control method. As a result, the maximum turnaround time of the developed direct MPC algorithm is only $41.6\,\mu$s, see Table 5.7 where the average and maximum turnaround times of the four discussed control algorithms are summarized. This time is much smaller than the sampling interval T_s, which in the case of $f_{\mathrm{sw}} = 700\,$Hz is about $370\,\mu$s, meaning that only about 10% of the available time is used to execute the controller. In contrast to that, e.g., FCS-MPC2, whose sampling time is $62.5\,\mu$s, requires about $20/62.5 = 32\%$ of the available time for the controller.

CHAPTER 6

Model Predictive Control for Grid-tied Converters with LCL Filters

In this chapter, the direct MPC method is refined to control GTCs, with the goal to guarantee high power quality and robustness during nominal and faulty grid conditions. To this end, a prediction model suitable for a wide range of operation conditions is first derived. Then, the reference values of the controlled variables, i.e., the grid current, filter capacitor voltage, and converter current, are generated such that a favorable control performance is achieved during both nominal operations and grid faults. To do so, the harmonic impedance model of the system is employed. In a next step, the direct MPC scheme is designed as multi-objective optimization problem that can address all considered cases. The formulated constrained QP underlying the MPC is finally solved in a computationally efficient manner in real time with an in-house solver.

6.1 Control Model

Fig. 6.1 depicts the grid-tied converter with an LCL filter. A three-phase two-level voltage source inverter (VSI) is considered in this case study. Therefore, each phase leg $x \in \{a,\ b,\ c\}$ has two switching states $u_x \in \{-1,\ 1\}$, which correspond to the two discrete voltage output $\frac{V_{\mathrm{dc}}}{2}$ and $-\frac{V_{\mathrm{dc}}}{2}$, respectively, with V_{dc} denoting the dc-link voltage. Let $\boldsymbol{u}_{abc} = [u_a\ u_b\ u_c]^T$ denote the three-phase switch position, the converter output voltage $\boldsymbol{v}_{\mathrm{conv}}$ is given by

$$\boldsymbol{v}_{\mathrm{conv}} = \frac{V_{\mathrm{dc}}}{2}\boldsymbol{K}\boldsymbol{u}_{abc}\,. \tag{6.1}$$

Fig. 6.2 shows the equivalent circuit of the system, where $\boldsymbol{v}_{\mathrm{conv}}$ ($\boldsymbol{v}_g$) and $\boldsymbol{i}_{\mathrm{conv}}$ ($\boldsymbol{i}_g$) are the converter (grid) voltage and current, respectively, and $\boldsymbol{v}_c$ is the voltage across the filter capacitor. Besides, L_{lc} (L_{lg}) and R_{lc} (R_{lg}) are the converter (grid) side inductance and resistance of the filter, receptively, C_c (R_c) is the capacitance (resistance) of the filter capacitor, and L_g (R_g) is

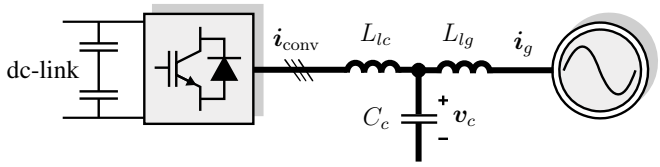

Figure 6.1: Grid-tied converter with an LCL filter.

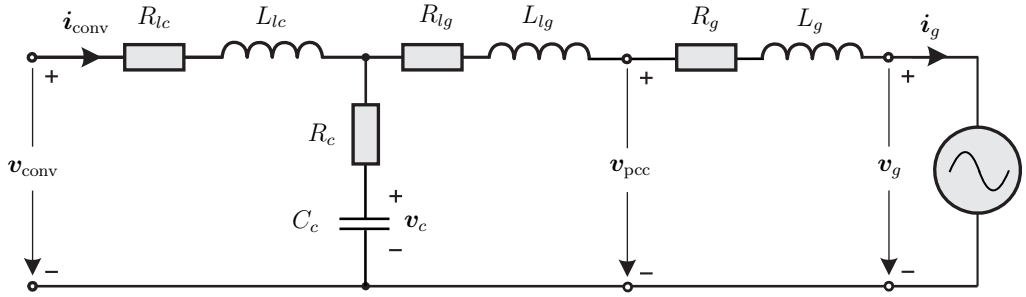

Figure 6.2: Equivalent circuit of the grid-tied converter with an LCL filter.

the grid inductance (resistance). By applying the Kirchhof's circuit law to the equivalent circuit, the state-space model of the system is derived as

$$\frac{\mathrm{d}\boldsymbol{i}_{\text{conv}}}{\mathrm{d}t} = \frac{1}{L_{lc}}(-(R_{lc}+R_c)\boldsymbol{i}_{\text{conv}} + R_c\boldsymbol{i}_g - \boldsymbol{v}_c + \boldsymbol{v}_{\text{conv}}) \tag{6.2a}$$

$$\frac{\mathrm{d}\boldsymbol{i}_g}{\mathrm{d}t} = \frac{1}{L_{lg}}(-(R_{lg}+R_c)\boldsymbol{i}_g + R_c\boldsymbol{i}_{\text{conv}} + \boldsymbol{v}_c - \boldsymbol{v}_{\text{pcc}}) \tag{6.2b}$$

$$\frac{\mathrm{d}\boldsymbol{v}_c}{\mathrm{d}t} = \frac{1}{C_c}(\boldsymbol{i}_{\text{conv}} - \boldsymbol{i}_g)\,. \tag{6.2c}$$

By considering generic grid conditions, the voltage at the PCC can be written as

$$\boldsymbol{v}_{\text{pcc}} = \sum_{h\in\mathcal{H}} \boldsymbol{v}_{\text{pcc},h} = \sum_{h\in\mathcal{H}} \hat{V}_h \begin{bmatrix} \cos\left(h\omega_g t + \varphi_h\right) \\ \sin\left(h\omega_g t + \varphi_h\right) \end{bmatrix}, \tag{6.3}$$

where h denotes the harmonic order and $\mathcal{H}$ is the set of all harmonics.[1] Moreover, ω_g is the angular grid frequency, $\hat{V}_h$ and φ_h are the amplitude and phase of the h^{th} harmonic, respectively, and they can be detected with phase-lock loops (PLLs) augmented with a decoupling network and low-pass filters (LPFs) [61]. Based on (6.3), the dynamics of the PCC voltage are described by

$$\frac{\mathrm{d}\boldsymbol{v}_{\text{pcc}}}{\mathrm{d}t} = \sum_{h\in\mathcal{H}} h\omega_g \boldsymbol{J}\boldsymbol{v}_{\text{pcc},h}\,, \quad \text{with} \quad \boldsymbol{J} = \begin{bmatrix} 0 & -1 \\ 1 & 0 \end{bmatrix}. \tag{6.4}$$

[1]Without loss of generality, in this work, the fundamental component as well as the (negative) 5^{th} and the (positive) 7^{th} harmonics are considered in nominal operating conditions, i.e., $\mathcal{H} = \{1, -5, 7\}$, while the positive- and negative-sequence fundamental components are considered during faulty conditions, i.e., $\mathcal{H} = \{-1, 1\}$.

Based on (6.2) and (6.4), the continuous-time state-space model of the system is

$$\frac{\mathrm{d}\boldsymbol{x}(t)}{\mathrm{d}t} = \boldsymbol{F}\boldsymbol{x}(t) + \boldsymbol{G}\boldsymbol{u}_{abc}(t) + \boldsymbol{\varepsilon}(t) \tag{6.5a}$$

$$\boldsymbol{y}(t) = \boldsymbol{C}\boldsymbol{x}(t)\,, \tag{6.5b}$$

where $\boldsymbol{x} = [\boldsymbol{i}_{\mathrm{conv}}^T\ \boldsymbol{i}_g^T\ \boldsymbol{v}_c^T\ \boldsymbol{v}_{\mathrm{pcc}}^T]^T$ is the state vector, $\boldsymbol{y} = [\boldsymbol{i}_{\mathrm{conv}}^T\ \boldsymbol{i}_g^T\ \boldsymbol{v}_c^T]^T$ the output vector, and $\boldsymbol{\varepsilon} = [\boldsymbol{0}_{6\times1}^T\ (\sum_{h\in\mathcal{H}} h\omega_g \boldsymbol{J}\boldsymbol{v}_{\mathrm{pcc},h})^T]^T$. Moreover, the matrices in (6.5) are

$$\boldsymbol{F} = \begin{bmatrix} -\frac{R_{lc}+R_c}{L_{lc}}\boldsymbol{I}_2 & \frac{R_c}{L_{lc}}\boldsymbol{I}_2 & -\frac{1}{L_{lc}}\boldsymbol{I}_2 & \boldsymbol{0}_{2\times2} \\ \frac{R_c}{L_{lg}}\boldsymbol{I}_2 & -\frac{R_{lg}+R_c}{L_{lg}}\boldsymbol{I}_2 & \frac{1}{L_{lg}}\boldsymbol{I}_2 & -\frac{1}{L_{lg}}\boldsymbol{I}_2 \\ \frac{1}{C_c}\boldsymbol{I}_2 & -\frac{1}{C_c}\boldsymbol{I}_2 & \boldsymbol{0}_{2\times2} & \boldsymbol{0}_{2\times2} \\ \boldsymbol{0}_{2\times2} & \boldsymbol{0}_{2\times2} & \boldsymbol{0}_{2\times2} & \boldsymbol{0}_{2\times2} \end{bmatrix}$$

$$\boldsymbol{G} = \frac{V_{\mathrm{dc}}}{2L_{lc}}[\boldsymbol{I}_2\ \boldsymbol{0}_{2\times6}]^T\boldsymbol{K} \quad \text{and} \quad \boldsymbol{C} = [\boldsymbol{I}_6\ \boldsymbol{0}_{6\times2}]\,,$$

where $\boldsymbol{I}$ and $\boldsymbol{0}$ are the identity and zero matrices, respectively, the dimensions of which are indicated by the corresponding subscripts. Finally, using exact discretization, the discrete-time state-space model is derived as

$$\boldsymbol{x}(k+1) = \boldsymbol{A}\boldsymbol{x}(k) + \boldsymbol{B}\boldsymbol{u}_{abc}(k) + \boldsymbol{d}(k) \tag{6.7a}$$

$$\boldsymbol{y}(k) = \boldsymbol{C}\boldsymbol{x}(k)\,, \tag{6.7b}$$

with

$$\boldsymbol{A} = \boldsymbol{e}^{\boldsymbol{F}T_s}\,, \quad \boldsymbol{B} = \int_0^{T_s} \boldsymbol{e}^{\boldsymbol{F}\tau}\mathrm{d}\tau\boldsymbol{G}\,, \quad \boldsymbol{d} = \int_0^{T_s} \boldsymbol{e}^{\boldsymbol{F}\tau}\mathrm{d}\tau\boldsymbol{\varepsilon}\,,$$

T_s being the sampling interval, and $k \in \mathbb{N}$ the discrete time step.

6.2 Direct MPC with Fixed Switching Frequency for Adverse Grid Conditions

6.2.1 Output References

The control objective of the proposed direct MPC is to regulate the output variables $\boldsymbol{y}$ to their reference values $\boldsymbol{y}_{\mathrm{ref}} = [\boldsymbol{i}_{\mathrm{conv,ref}}^T\ \boldsymbol{i}_{g,\mathrm{ref}}^T\ \boldsymbol{v}_{c,\mathrm{ref}}^T]^T$, so that the desired active P_{ref} and reactive Q_{ref} power exchange at the PCC is successfully controlled. Considering different grid conditions, the calculation of the output reference vector $\boldsymbol{y}_{\mathrm{ref}}$ can be grouped into two cases, as presented in the sequel.

6.2.1.1 Nominal Operations

The grid voltage often contains harmonics. Nevertheless, even in the presence of such persistent disturbances, the current injected into the PCC should have a low THD value in nominal

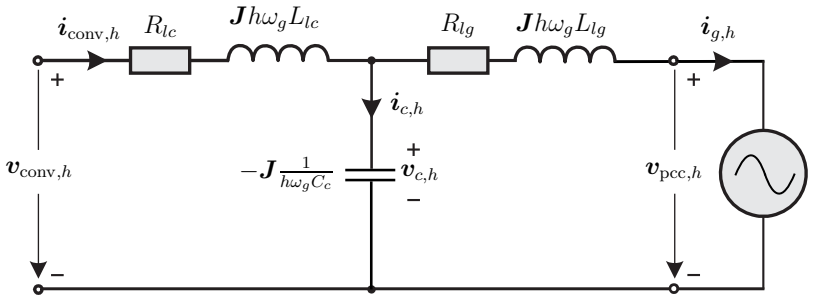

Figure 6.3: Harmonic impedance circuit of the grid-tied converter with an LCL filter in the stationary ($\alpha\beta$) frame.

operation to meet the relevant grid code. To ensure this, the grid current reference $\boldsymbol{i}_{g,\mathrm{ref}} = [i_{g,\mathrm{ref},\alpha}\ i_{g,\mathrm{ref},\beta}]^T$ should contain only the fundamental component, i.e.,

$$i_{g,\mathrm{ref},\alpha} = \frac{2}{3}\frac{P_{\mathrm{ref}} v_{\mathrm{pcc},\alpha,1} + Q_{\mathrm{ref}} v_{\mathrm{pcc},\beta,1}}{\|\boldsymbol{v}_{\mathrm{pcc},1}\|_2^2} \tag{6.8a}$$

$$i_{g,\mathrm{ref},\beta} = \frac{2}{3}\frac{P_{\mathrm{ref}} v_{\mathrm{pcc},\beta,1} - Q_{\mathrm{ref}} v_{\mathrm{pcc},\alpha,1}}{\|\boldsymbol{v}_{\mathrm{pcc},1}\|_2^2}\,. \tag{6.8b}$$

In a next step, the capacitor voltage reference $\boldsymbol{v}_{c,\mathrm{ref}}$ and the converter current reference $\boldsymbol{i}_{\mathrm{conv,ref}}$ are calculated based on the harmonic impedance circuit, shown in Fig. 6.3, where the capacitor resistance R_c is neglected because of its small value. This yields

$$\boldsymbol{v}_{c,\mathrm{ref},h} = \boldsymbol{v}_{\mathrm{pcc},h} + \boldsymbol{Z}_{lg,h}\boldsymbol{i}_{g,\mathrm{ref},h} \tag{6.9a}$$

$$\boldsymbol{i}_{\mathrm{conv,ref},h} = \boldsymbol{i}_{g,\mathrm{ref},h} + \boldsymbol{Z}_{c,\mathrm{inv},h}\boldsymbol{v}_{c,\mathrm{ref},h}\,, \tag{6.9b}$$

with

$$\boldsymbol{Z}_{lg,h} = R_{lg}\boldsymbol{I}_2 + \boldsymbol{J}h\omega_g L_{lg} \quad \text{and} \quad \boldsymbol{Z}_{c,\mathrm{inv},h} = \boldsymbol{J}h\omega_g C_c\,.$$

Note that $\boldsymbol{i}_{g,\mathrm{ref},h} = \boldsymbol{0}$ for $h \neq 1$, while $\boldsymbol{i}_{g,\mathrm{ref},1} = \boldsymbol{i}_{g,\mathrm{ref}}$ is calculated from (6.8). Finally, the references of the capacitor voltage and the converter current are calculated by superimposing all harmonic components, i.e.,

$$\boldsymbol{v}_{c,\mathrm{ref}} = \sum_{h\in\mathcal{H}} \boldsymbol{v}_{c,\mathrm{ref},h} \quad \text{and} \quad \boldsymbol{i}_{\mathrm{conv,ref}} = \sum_{h\in\mathcal{H}} \boldsymbol{i}_{\mathrm{conv,ref},h}\,.$$

6.2.1.2 Grid Faults

During grid faults, the three-phase grid voltage—and consequently the voltage at the PCC—contains both positive- and negative-sequence voltage components at the fundamental frequency [40], i.e., $\boldsymbol{v}_{\mathrm{pcc},1}$ and $\boldsymbol{v}_{\mathrm{pcc},-1}$. Depending on the control goals, the grid current reference can be calculated based on different strategies [41]. In the following, two typical strategies are discussed.

First, the grid current is split into two components as

$$\boldsymbol{i}_{g,\mathrm{ref}} = \boldsymbol{i}_{p,\mathrm{ref}} + \boldsymbol{i}_{q,\mathrm{ref}}\,, \tag{6.10}$$

where $\boldsymbol{i}_{p,\mathrm{ref}}$ and $\boldsymbol{i}_{q,\mathrm{ref}}$ can be interpreted as the active and reactive current vectors, respectively [62]. When a balanced three-phase sinusoidal current is desired at the PCC, the balanced positive-sequence control (BPSC) strategy can be used to calculate the grid current references according to

$$\boldsymbol{i}_{p,\mathrm{ref}} = \frac{P_{\mathrm{ref}}}{\|\boldsymbol{v}_{\mathrm{pcc},1}\|_2^2}\boldsymbol{v}_{\mathrm{pcc},1} \tag{6.11a}$$

$$\boldsymbol{i}_{q,\mathrm{ref}} = \frac{Q_{\mathrm{ref}}}{\|\boldsymbol{v}_{\mathrm{pcc},1}\|_2^2}\boldsymbol{v}_{\mathrm{pcc},1}^{\perp}\,, \tag{6.11b}$$

where $\boldsymbol{v}_{\mathrm{pcc},1}^{\perp} = \boldsymbol{J}\boldsymbol{v}_{\mathrm{pcc},1}$ is the (leading) orthogonal vector of $\boldsymbol{v}_{\mathrm{pcc},1}$. Note that (6.10) and (6.11) yield the same result as (6.8). This implies that when a balanced sinusoidal current is required at the PCC, the active and reactive powers oscillate during a grid fault because of the negative-sequence voltage component, as also shown in Section 7.2.
An alternative approach is the positive- and negative-sequence control (PNSC) strategy. This method considers both the positive- and negative-sequence fundamental voltage components in the calculation of the active and reactive current references, i.e.,

$$\boldsymbol{i}_{p,\mathrm{ref}} = \frac{P_{\mathrm{ref}}}{\|\boldsymbol{v}_{\mathrm{pcc},1}\|_2^2 + \|\boldsymbol{v}_{\mathrm{pcc},-1}\|_2^2}(\boldsymbol{v}_{\mathrm{pcc},1} + \boldsymbol{v}_{\mathrm{pcc},-1}) \tag{6.12a}$$

$$\boldsymbol{i}_{q,\mathrm{ref}} = \frac{Q_{\mathrm{ref}}}{\|\boldsymbol{v}_{\mathrm{pcc},1}\|_2^2 + \|\boldsymbol{v}_{\mathrm{pcc},-1}\|_2^2}(\boldsymbol{v}_{\mathrm{pcc},1}^{\perp} + \boldsymbol{v}_{\mathrm{pcc},-1}^{\perp})\,. \tag{6.12b}$$

By doing so, the current references consist of both positive- and negative-sequence components, resulting in a constant active power when the reactive power reference is set to zero. Finally, the capacitor voltage $\boldsymbol{v}_{c,\mathrm{ref}}$ and the converter current $\boldsymbol{i}_{\mathrm{conv,ref}}$ references are calculated by following the same principle explained in Section 6.2.1.1.

6.2.2 Control Method

As a direct controller, the proposed MPC algorithm manipulates the converter switches directly. However, in contrast to typical direct control strategies, the proposed method ensures a fixed switching frequency by forcing each phase to switch once per sampling interval T_s. To this end, the vector of switching time instants $\boldsymbol{t}$ is introduced along with the corresponding switching sequence $\boldsymbol{U}$ as

$$\begin{aligned}\boldsymbol{t} &= [t_1 \;\; t_2 \;\; t_3]^T \\ \boldsymbol{U} &= [\boldsymbol{u}_{abc}^T(t_0) \;\; \boldsymbol{u}_{abc}^T(t_1) \;\; \boldsymbol{u}_{abc}^T(t_2) \;\; \boldsymbol{u}_{abc}^T(t_3)]^T\,,\end{aligned} \tag{6.13}$$

where the switching time instants respect $0 \leq t_1 \leq t_2 \leq t_3 \leq T_s$. Moreover, $\boldsymbol{u}_{abc}(t_0)$ is the switch position at the beginning of the sampling interval, i.e., $t_0 \equiv 0$, while $\boldsymbol{u}_{abc}(t_i)$, with $i \in \{1,\ 2,\ 3\}$, is the switch position after one of the three phases switches at instant t_i. Considering (6.13) and the fact that all three phases have to switch within each T_s once, it follows that the three phases can switch in six possible chronological orders. This gives rise to six candidate switching sequences $\boldsymbol{U}_z$ with $z \in \{1,\ 2 \ldots 6\}$, as summarized in Table 4.1.
Having fixed the switching frequency with the above-mentioned procedure, the goal of the controller is to minimize the (approximate) rms ripple of the controlled variables. This can be

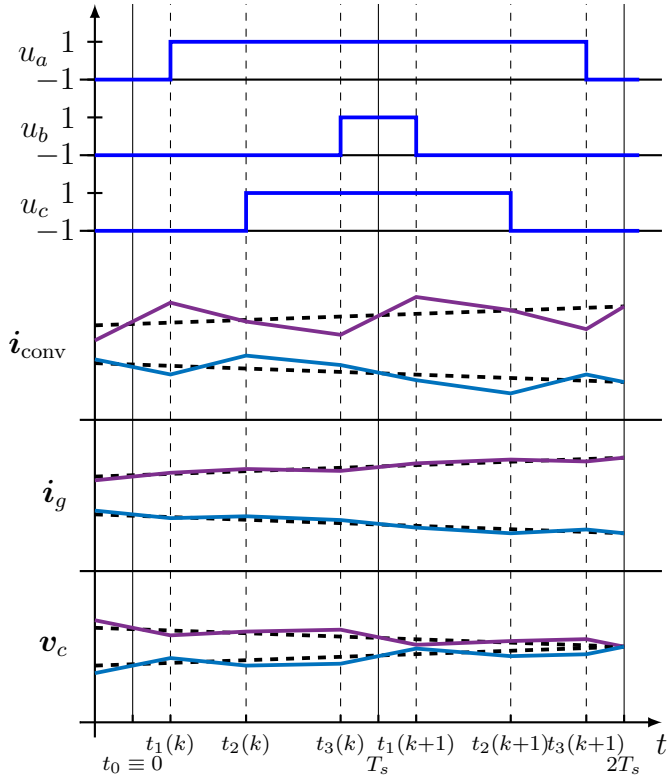

Figure 6.4: Example of the evolution of the outputs over two sampling intervals by applying the depicted switching sequence.

achieved by designing the objective function to capture the output tracking error at the switching time instants. Moreover, to avoid arbitrary changes in the control input, its rate of change within one sampling interval is modeled and accounted for in the objective function. Therefore, the objective function is defined as

$$J = \sum_{i=1}^{3} \left\| \boldsymbol{y}_{\text{ref}}(t_i(k)) - \boldsymbol{y}(t_i(k)) \right\|_{\boldsymbol{Q}}^2 + \left\| \boldsymbol{\Lambda} \big(\boldsymbol{y}_{\text{ref}}(T_s(k)) - \boldsymbol{y}(T_s(k)) \big) \right\|_{\boldsymbol{Q}}^2 + \lambda_u \left\| \Delta \bar{\boldsymbol{u}}_{abc}(k) \right\|_2^2 , \tag{6.14}$$

where $\Delta \bar{\boldsymbol{u}}_{abc}(k) = \bar{\boldsymbol{u}}_{abc}(k) - \bar{\boldsymbol{u}}_{abc}(k-1)$ is the change of the averaged control input between two consecutive sampling intervals, with $\bar{\boldsymbol{u}}_{abc} = (\sum_{i=0}^{3} \boldsymbol{u}_{abc}(t_i)\tilde{t}_i)/T_s$, while $\tilde{t}_i = t_{i+1} - t_i$, with $i \in \{0, 1, 2, 3\}$ and $t_4 = T_s$. Moreover, $\lambda_u > 0$ is the weighting factor that adjusts the trade-off between control and output tracking effort, while the diagonal positive definite matrix $\boldsymbol{Q} \succ 0$ sets the priority among the tracking of the different controlled variables. Finally, $\boldsymbol{\Lambda} \succ 0$ is introduced to penalize more heavily the output error at the end of the sampling interval. As explained in [23], by doing so, the output error at the discrete time instants is driven to zero, enabling the effective elimination of the undesired low-frequency harmonics.

In a next step, the evolution of the system output is predicted for each candidate switching sequence $\boldsymbol{U}_z$. Given that the sampling interval T_s is much smaller than the fundamental period, the evolution of the output trajectories can be considered as linear within one T_s. Therefore, the

future behavior of the system can be calculated with

$$\boldsymbol{y}(t_{i+1}(k)) = \boldsymbol{y}(t_i(k)) + \boldsymbol{m}(t_i(k))(t_{i+1}(k) - t_i(k))\,, \tag{6.15}$$

where $\boldsymbol{m}(t_i(k))$ is the gradient of the output vector when the switch position $\boldsymbol{u}_{abc}(t_i(k))$ is applied, i.e.,

$$\begin{aligned}\boldsymbol{m}(t_i(k)) &= \frac{\boldsymbol{y}(k+1) - \boldsymbol{y}(k)}{T_s} \\ &= \frac{\boldsymbol{C}((\boldsymbol{A} - \boldsymbol{I})\boldsymbol{x}(k) + \boldsymbol{B}\boldsymbol{u}_{abc}(t_i(k)) + \boldsymbol{d}(k))}{T_s}\,.\end{aligned} \tag{6.16}$$

with $i \in \{0, 1, 2, 3\}$ and $t_4 = T_s$.
Following the same principle, the output reference is assumed to evolve linearly within one sampling interval,[2] i.e.,

$$\boldsymbol{y}_{\mathrm{ref}}(t) = \boldsymbol{y}_{\mathrm{ref}}(k) + \boldsymbol{m}_{\mathrm{ref}}(k)\,t\,, \tag{6.17}$$

with

$$\boldsymbol{m}_{\mathrm{ref}}(k) = \frac{\boldsymbol{y}_{\mathrm{ref}}(k+1) - \boldsymbol{y}_{\mathrm{ref}}(k)}{T_s}\,. \tag{6.18}$$

An example of the evolution of the output variables for a given switching sequence along with their references is shown in Fig. 6.4.
Based on the above, the objective function can be written in the following vector form

$$J = \|\boldsymbol{r} - \boldsymbol{M}\boldsymbol{t}\|^2_{\widetilde{\boldsymbol{Q}}} + \lambda_u \|\boldsymbol{S}\boldsymbol{t} - \boldsymbol{w}\|_2^2\,, \tag{6.19}$$

where the vector $\boldsymbol{r} \in \mathbb{R}^{24}$ and the matrix $\boldsymbol{M} \in \mathbb{R}^{24\times 3}$ are

$$\boldsymbol{r} = \begin{bmatrix} \boldsymbol{y}_{\mathrm{ref}}(t_0) - \boldsymbol{y}(t_0) \\ \boldsymbol{y}_{\mathrm{ref}}(t_0) - \boldsymbol{y}(t_0) \\ \boldsymbol{y}_{\mathrm{ref}}(t_0) - \boldsymbol{y}(t_0) \\ \boldsymbol{\Lambda}(\boldsymbol{y}_{\mathrm{ref}}(T_s) - \boldsymbol{y}(t_0) - \boldsymbol{m}(t_3)T_s) \end{bmatrix} \tag{6.20}$$

and

$$\boldsymbol{M} = \begin{bmatrix} \boldsymbol{m}_{t_0} & \boldsymbol{0}_3 & \boldsymbol{0}_3 \\ \boldsymbol{m}_0 & \boldsymbol{m}_{t_1} & \boldsymbol{0}_3 \\ \boldsymbol{m}_0 & \boldsymbol{m}_1 & \boldsymbol{m}_{t_2} \\ \boldsymbol{\Lambda}\boldsymbol{m}_0 & \boldsymbol{\Lambda}\boldsymbol{m}_1 & \boldsymbol{\Lambda}\boldsymbol{m}_2 \end{bmatrix} \tag{6.21}$$

with

$$\boldsymbol{m}_{t_i} = \boldsymbol{m}(t_i) - \boldsymbol{m}_{\mathrm{ref}} \tag{6.22}$$

$$\boldsymbol{m}_i = \boldsymbol{m}(t_i) - \boldsymbol{m}(t_{i+1}) \tag{6.23}$$

[2]Note that the references of the capacitor voltage and the converter current include harmonics at the same frequencies as that of the grid voltage. However, these harmonics are of low order, thus, the evolution of the references can still be assumed linear within one T_s.

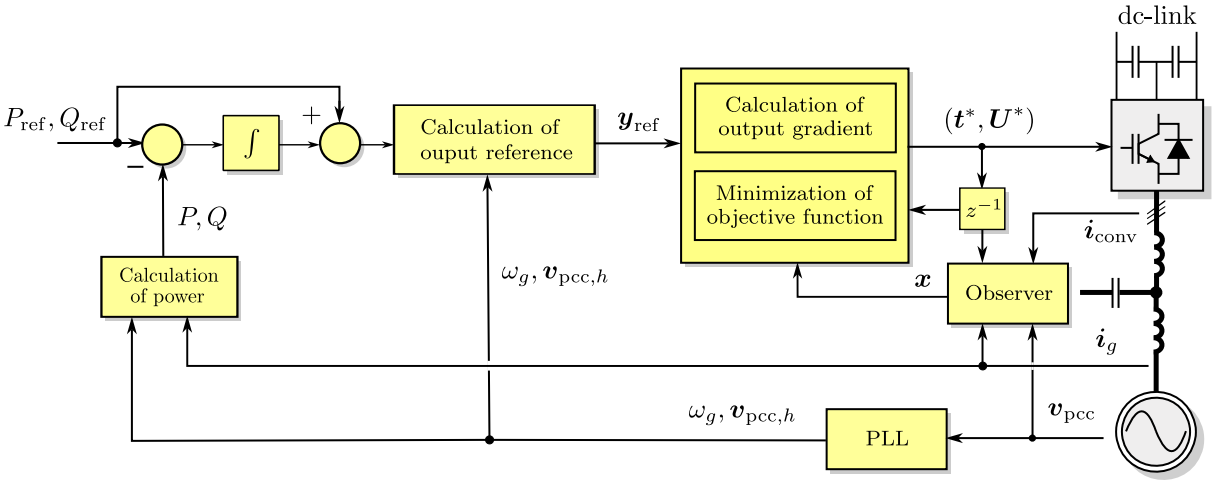

Figure 6.5: Fixed switching frequency direct MPC for a three-phase grid-tied converter with an LCL filter.

Algorithm 6 Fixed Switching Frequency Direct MPC

Given $P_{\text{ref}}(k)$, $Q_{\text{ref}}(k)$ and $\boldsymbol{x}(k)$

1: Calculate the output reference vector $\boldsymbol{y}_{\text{ref}}$ from P_{ref} and Q_{ref}
2: Enumerate the possible switching sequences $\boldsymbol{U}_z$, $z \in \{1, 2, \ldots, 6\}$, and calculate the corresponding output gradient
3: For each $\boldsymbol{U}_z$:
    Detect if $\boldsymbol{U}_z$ is unsuited;
    If not, solve the QP (6.26). This yields $\boldsymbol{t}_z$ and J_z.
4: Compare the J_z of each candidate $\boldsymbol{U}_z$, and find the globally optimal solution $\boldsymbol{t}^*$ and $\boldsymbol{U}^*$.
Return $\boldsymbol{t}^*(k)$ and $\boldsymbol{U}^*(k)$.

where $i \in \{0,\ 1,\ 2\}$. Moreover, the matrix $\boldsymbol{S} \in \mathbb{R}^{3\times 3}$ and the vector $\boldsymbol{w} \in \mathbb{R}^3$ are

$$\boldsymbol{S} = \frac{1}{T_s}\begin{bmatrix}\Delta\boldsymbol{u}_{abc}(t_1) & \Delta\boldsymbol{u}_{abc}(t_2) & \Delta\boldsymbol{u}_{abc}(t_3)\end{bmatrix} \tag{6.24a}$$

$$\boldsymbol{w} = \boldsymbol{u}_{abc}(t_3) - \bar{\boldsymbol{u}}_{abc}(k-1)\,. \tag{6.24b}$$

with

$$\Delta\boldsymbol{u}(t_i) = \boldsymbol{u}_{abc}(t_i) - \boldsymbol{u}_{abc}(t_{i-1})\,, \quad i \in \{1,\ 2,\ 3\}. \tag{6.25}$$

Finally, $\widetilde{\boldsymbol{Q}} = \text{diag}(\boldsymbol{Q}, \boldsymbol{Q}, \boldsymbol{Q}, \boldsymbol{Q})$.

6.2.3 Optimization Problem

Based on the above, an optimization problem is formulated as a constrained QP for each one of the six candidate switching sequences $\boldsymbol{U}_z$. Specifically, the direct MPC problem is written in the form

$$\begin{aligned}\underset{\boldsymbol{t}\in\mathbb{R}^3}{\text{minimize}} \quad & \frac{1}{2}\boldsymbol{t}^T\boldsymbol{H}\boldsymbol{t} - \boldsymbol{f}^T\boldsymbol{t} \\ \text{subject to} \quad & 0 \le t_1(k) \le t_2(k) \le t_3(k) \le T_s\,.\end{aligned} \tag{6.26}$$

where the Hessian matrix $\boldsymbol{H} \in \mathbb{R}^{3\times3}$ and the vector $\boldsymbol{f} \in \mathbb{R}^3$ are

$$\boldsymbol{H} = \boldsymbol{M}^T\widetilde{\boldsymbol{Q}}\boldsymbol{M} + \lambda_u\boldsymbol{S}^T\boldsymbol{S}\,,$$

and

$$\boldsymbol{f} = \boldsymbol{M}^T\boldsymbol{r} + \lambda_u\boldsymbol{S}^T\boldsymbol{w}\,.$$

Problem (6.26) can be efficiently solved with the in-house solver presented Chapter 5. This solver is developed to fully exploit the geometry of (6.26) as it can quickly detect the unsuited switching sequences by a simple one-step projection. As a result, only two QPs need to be solved in the worst-case scenario, see Section 5.1 for more details.

In a last step, each QP that is eventually considered in the optimization process is solved to yield the locally optimal switching time instants $\boldsymbol{t}_z$ and the corresponding sequence $\boldsymbol{U}_z$, along with the associated cost J_z. To find the globally optimal solution, i.e., the pair $\{\boldsymbol{t}^*, \boldsymbol{U}^*\}$, the costs J_z of the solved QPs are compared and the pair that corresponds to the smallest cost is selected as the to-be-applied solution [23]. The proposed direct MPC scheme is summarized in the block diagram shown in Fig. 6.5,[3] while the pseudocode is provided in Algorithm 6.

Finally, it is worth mentioning that MPC, being in essence a proportional controller, can be aversely affected by modeling errors and mismatches, measurement noise, etc. The influence of these is manifested as a steady-state tracking error [63]. This offset can be effectively eliminated by introducing an integrating element in the control loop. In this work, this is done by augmenting the power references with the integral of their tracking errors, see Fig. 6.5.

[3]The capacitor voltage of the LCL filter is not always available in practice. To obtain the full-state information, an observer, e.g., a Kalman filter as the one designed in [26], can be used.

CHAPTER 7

Performance Evaluation for Grid-tied Converters with LCL Filters

The performance of the proposed direct MPC scheme for GTCs with LCL filters is examined in the laboratory with the test setup shown in Fig. 7.1. The converter is supplied by a stiff dc source and the grid emulator is the TC.ACS from Regatron. The real-time control platform is a dSPACE SCALEXIO system, consisting of an intel XEON processor and a Xilinx Kintex-7 field-programmable gate array (FPGA). The controller is implemented on the processor, and the data acquisition and generation of the switching signals are done on the FPGA. The rated values and the parameters of the system are given in Tables 7.1 and 7.2, respectively. For all the examined scenarios, the sampling frequency is chosen as $f_s = 10$ kHz, implying a switching frequency $f_{\text{sw}} = 5$ kHz. Besides, the weighting matrices are chosen as $\boldsymbol{Q} = \text{diag}(1, 1, 1, 1, 1, 1)$, $\boldsymbol{\Lambda} = \text{diag}(15, 15, 15)$ and $\lambda_u = 1 \cdot 10^{-3}$. Finally, all results are shown in the p.u. system.

7.1 Operation under Distorted Grid

7.1.1 Steady-State Operation

The steady-state performance of the proposed MPC scheme is first examined for the case where the grid voltage is seriously distorted as it contains a pronounced 5^{th} and 7^{th} harmonic, each of

Table 7.1: Rated values of the system.

Parameter	Symbol	SI Value
Rated voltage	V_R	200 V
Rated current	I_R	9 A
Grid frequency	f_{sR}	50 Hz

Table 7.2: System parameters in the SI and the p.u. system.

Parameter	SI (p.u.) symbol	SI (p.u.) value
Grid-side resistance	R_{lg} (R_{lg})	$0.07\,\Omega$ (0.0055)
Grid-side inductance	L_{lg} (X_{lg})	3.0 mH (0.0735)
Converter-side resistance	R_{lc} (R_{lc})	$0.1\,\Omega$ (0.0078)
Converter-side inductance	L_{lc} (X_{lc})	3.3 mH (0.0808)
Filter capacitor resistance	R_c (R_c)	$0.8\,\text{m}\Omega$ ($6.23 \cdot 10^{-5}$)
Filter capacitor capacitance	C_c (X_c)	8 µF (0.0322)
Filter resonant frequency	f_{res}	1417 Hz
Dc-link voltage	V_{dc} (V_{dc})	350 V (2.1433)

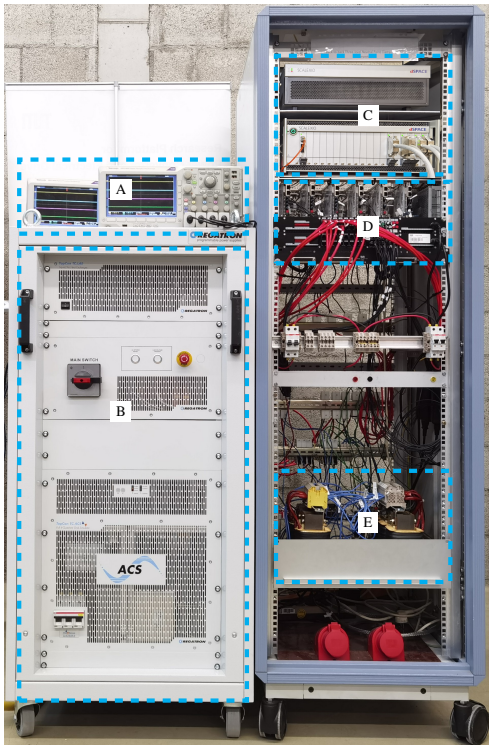

Figure 7.1: Setup of the three-phase 2L grid-tied converter with an LCL filter. A: Oscilloscope, B: Grid emulator, C: dSPACE SCALEXIO real-time control system, D: Three phase 2L converters with imperix PEB8038 submodules and interface, E: LCL filter

which has amplitude of 0.1 p.u. For this test, the system is operating at rated power under unity power factor, i.e., $P_{\text{ref}} = 1$ p.u. and $Q_{\text{ref}} = 0$ p.u. As nominal operation is considered here, the goal is to produce a balanced three-phase grid current with as low a THD as possible. Thus, the output references are calculated with (6.8) and (6.9). Fig. 7.2 shows the performance of the system in consideration. As can be seen, all controlled variables, i.e., $\boldsymbol{i}_{\text{conv}}$, $\boldsymbol{i}_g$ and $\boldsymbol{v}_c$, track their references accurately, thus ensuring that the injected power at the PCC is of high quality. This is further demonstrated by the grid current harmonic spectrum, shown in Fig. 7.2(e). The high-frequency harmonics due to the switching are effectively attenuated by the LCL filter, while

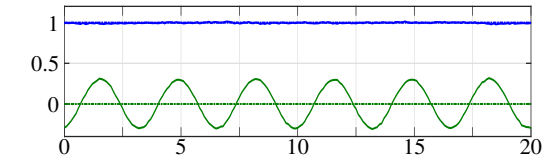

Time [ms]

(a) Active and reactive power at the PCC.

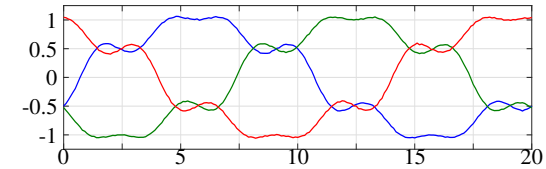

Time [ms]

(b) Three-phase PCC voltage $\boldsymbol{v}_{\mathrm{pcc},abc}$.

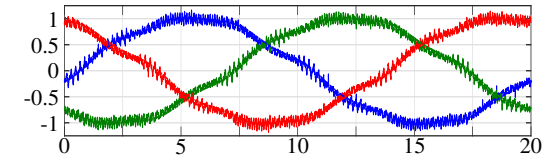

Time [ms]

(c) Three-phase converter current $\boldsymbol{i}_{\mathrm{conv},abc}$.

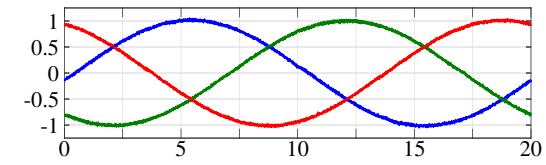

Time [ms]

(d) Three-phase grid current $\boldsymbol{i}_{g,abc}$.

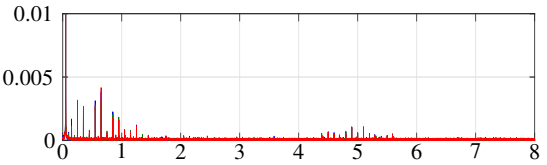

Frequency [kHz]

(e) Grid current harmonic spectrum (THD = 1.83%).

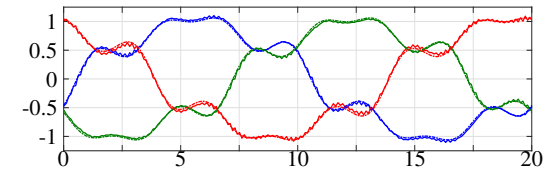

Time [ms]

(f) Three-phase capacitor voltage $\boldsymbol{v}_{c,abc}$.

Figure 7.2: Experimental results of direct MPC at steady-state operation under the distorted grid condition, $f_{\mathrm{sw}} = 5\,\mathrm{kHz}$.

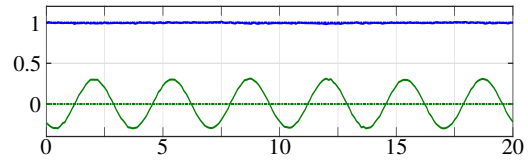

Time [ms]

(a) Active and reactive power at the PCC.

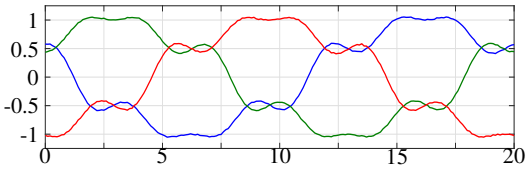

Time [ms]

(b) Three-phase PCC voltage $\boldsymbol{v}_{\mathrm{pcc},abc}$.

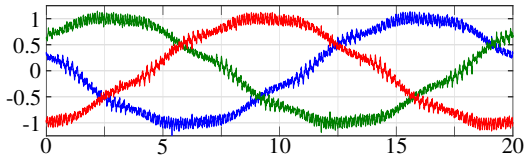

Time [ms]

(c) Three-phase converter current $\boldsymbol{i}_{\mathrm{conv},abc}$.

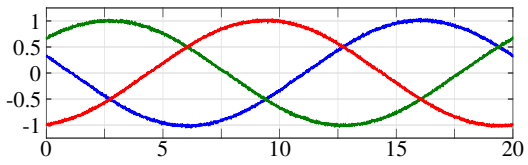

Time [ms]

(d) Three-phase grid current $\boldsymbol{i}_{g,abc}$.

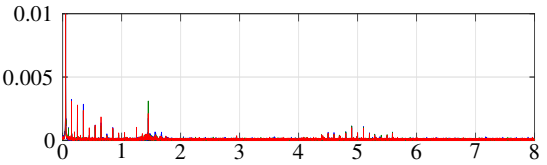

Frequency [kHz]

(e) Grid current harmonic spectrum (THD = 1.85%).

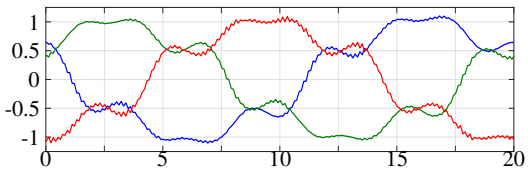

Time [ms]

(f) Three-phase capacitor voltage $\boldsymbol{v}_{c,abc}$.

Figure 7.3: Experimental results of VOC at steady-state operation under the distorted grid condition, $f_{\mathrm{sw}} = 5\,\mathrm{kHz}$.

the low-frequency harmonics that result from the voltage grid harmonics are compensated for by properly regulating the filter capacitor voltage $\boldsymbol{v}_c$ and the converter current $\boldsymbol{i}_{\mathrm{conv}}$ along their

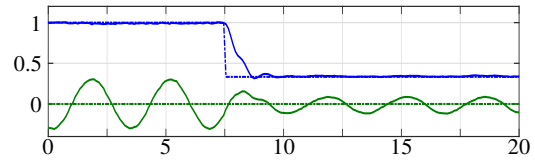

(a) Active and reactive power at the PCC.

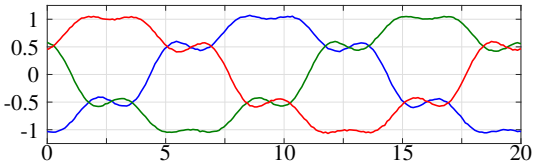

(b) Three-phase PCC voltage $\boldsymbol{v}_{\mathrm{pcc},abc}$.

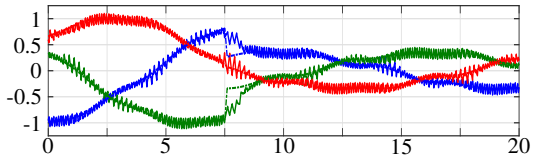

(c) Three-phase converter current $\boldsymbol{i}_{\mathrm{conv},abc}$.

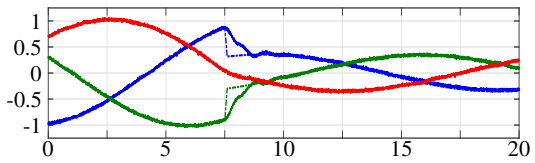

(d) Three-phase grid current $\boldsymbol{i}_{g,abc}$.

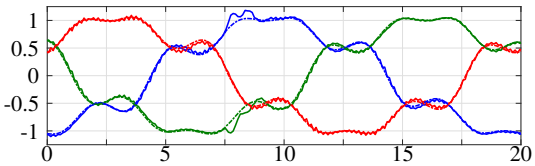

(e) Three-phase capacitor voltage $\boldsymbol{v}_{c,abc}$.

Figure 7.4: Experimental results of direct MPC at a step-down power transient under the distorted grid condition, $f_{\mathrm{sw}} = 5\,\mathrm{kHz}$.

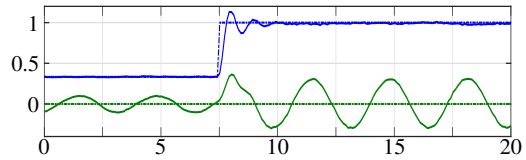

(a) Active and reactive power at the PCC.

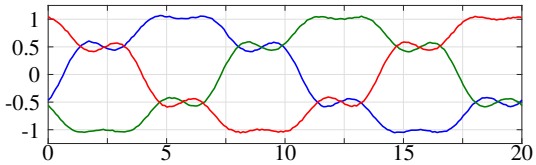

(b) Three-phase PCC voltage $\boldsymbol{v}_{\mathrm{pcc},abc}$.

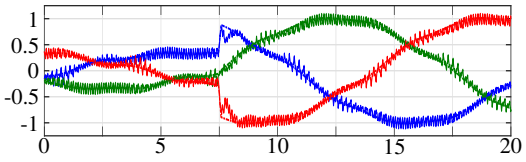

(c) Three-phase converter current $\boldsymbol{i}_{\mathrm{conv},abc}$.

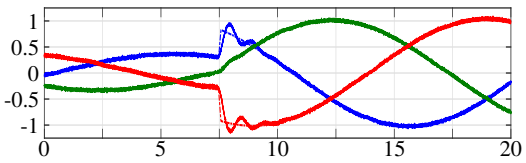

(d) Three-phase grid current $\boldsymbol{i}_{g,abc}$.

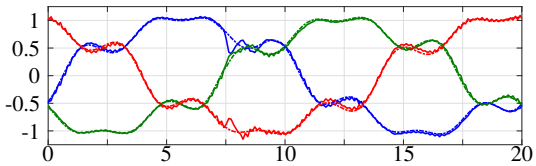

(e) Three-phase capacitor voltage $\boldsymbol{v}_{c,abc}$.

Figure 7.5: Experimental results of direct MPC at a step-up power transient under the distorted grid condition, $f_{\mathrm{sw}} = 5\,\mathrm{kHz}$.

tailored reference values. As a result, the grid current THD is only 1.83%. It is noteworthy that such a low THD value is achieved despite the somewhat pronounced 11^{th} and 13^{th} harmonics which appear due to additional low-frequency harmonics in the grid that are not directly accounted for.

For comparison purposes, a conventional PI-based VOC strategy [36] with SVM is also implemented. This method is augmented with a capacitor-current-feedback loop for active damping [64]. Moreover, additional PI-based control loops are designed in rotating reference frames synchronized with the pronounced grid voltage harmonics to compensate for them [2]. The pa-

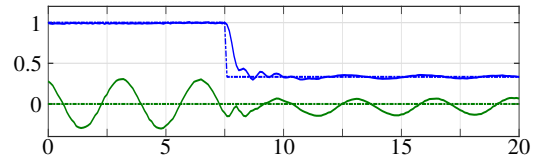

(a) Active and reactive power at the PCC.

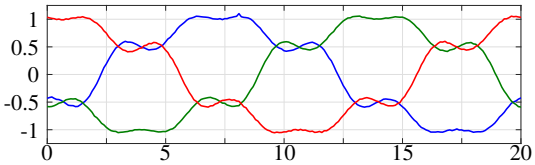

(b) Three-phase PCC voltage $\boldsymbol{v}_{\mathrm{pcc},abc}$.

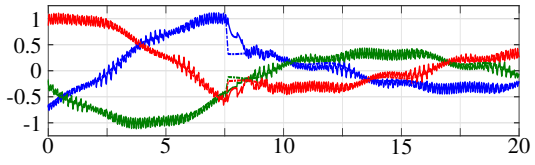

(c) Three-phase converter current $\boldsymbol{i}_{\mathrm{conv},abc}$.

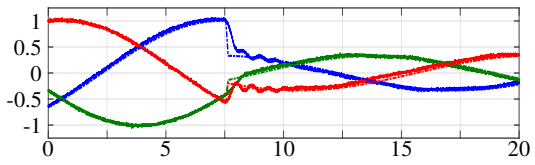

(d) Three-phase grid current $\boldsymbol{i}_{g,abc}$.

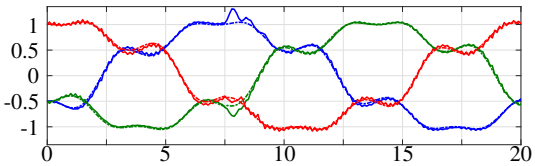

(e) Three-phase capacitor voltage $\boldsymbol{v}_{c,abc}$.

Figure 7.6: Experimental results of VOC during an active power reference step-up change under distorted grid conditions, $f_{\mathrm{sw}} = 5\,\mathrm{kHz}$.

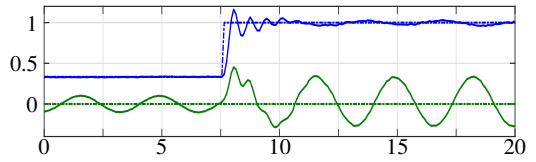

(a) Active and reactive power at the PCC.

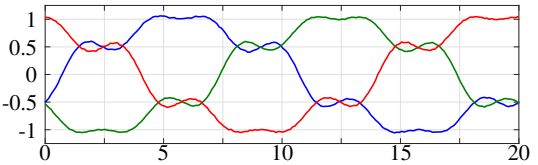

(b) Three-phase PCC voltage $\boldsymbol{v}_{\mathrm{pcc},abc}$.

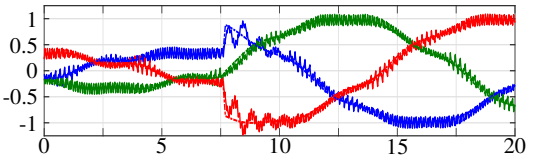

(c) Three-phase converter current $\boldsymbol{i}_{\mathrm{conv},abc}$.

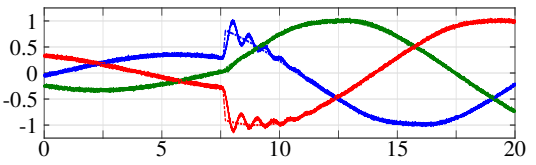

(d) Three-phase grid current $\boldsymbol{i}_{g,abc}$.

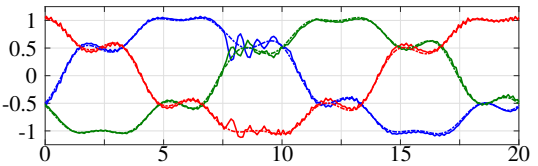

(e) Three-phase capacitor voltage $\boldsymbol{v}_{c,abc}$.

Figure 7.7: Experimental results of VOC during an active power reference step down under distorted grid conditions, $f_{\mathrm{sw}} = 5\,\mathrm{kHz}$.

rameters of the PI controllers are tuned according to the optimum method [65], and the gain in the active-damping loop is tuned according to the root loci analysis [66]. As shown in Fig. 7.3, the steady-state performance of the conventional linear controller with a separate modulation stage is very similar to that of the proposed direct MPC in that both methods achieve similar THD values for the grid current. However, it is noticeable that the grid current spectrum produced by VOC has pronounced harmonics around the filter resonance frequency $f_{\mathrm{res}} = 1417\,\mathrm{Hz}$. This is in contrast to the direct MPC, which demonstrates the better active damping ability of the proposed control method.

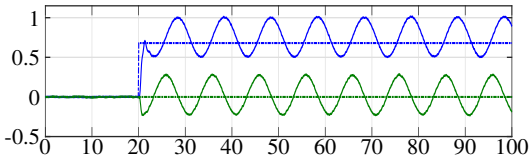

(a) Active and reactive power at the PCC.

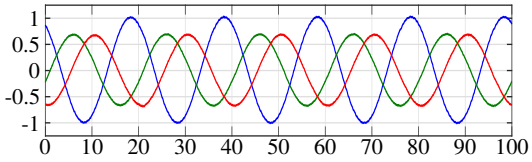

(b) Three-phase PCC voltage $\boldsymbol{v}_{\mathrm{pcc},abc}$.

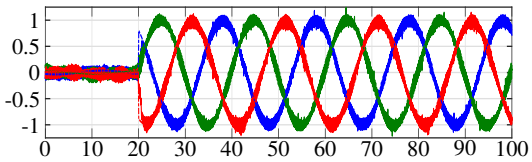

(c) Three-phase converter current $\boldsymbol{i}_{\mathrm{conv},abc}$.

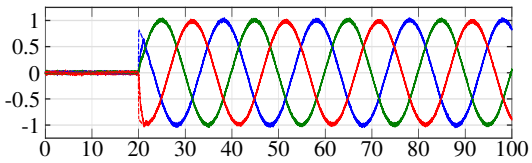

(d) Three-phase grid current $\boldsymbol{i}_{g,abc}$.

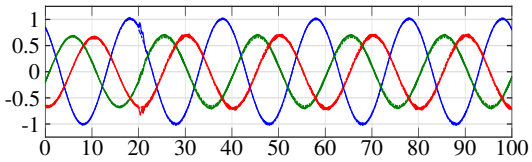

(e) Three-phase capacitor voltage $\boldsymbol{v}_{c,abc}$.

Figure 7.8: Experimental results of direct MPC during an active power reference step-up change under distorted grid conditions, $f_{\mathrm{sw}} = 5\,\mathrm{kHz}$.

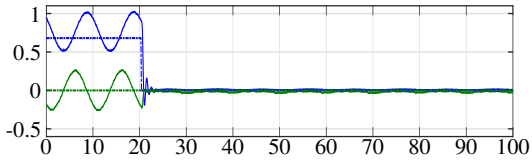

(a) Active and reactive power at the PCC.

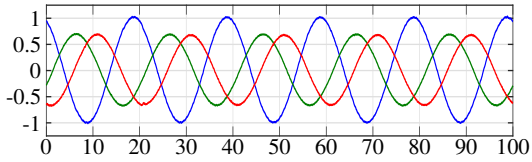

(b) Three-phase PCC voltage $\boldsymbol{v}_{\mathrm{pcc},abc}$.

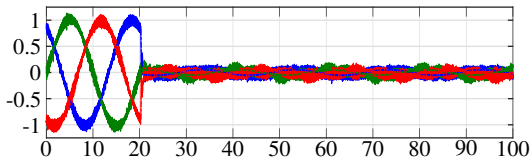

(c) Three-phase converter current $\boldsymbol{i}_{\mathrm{conv},abc}$.

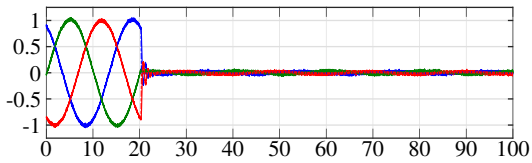

(d) Three-phase grid current $\boldsymbol{i}_{g,abc}$.

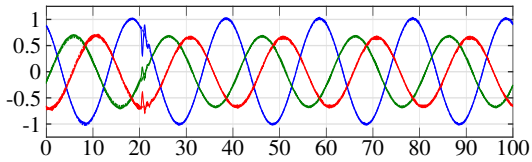

(e) Three-phase capacitor voltage $\boldsymbol{v}_{c,abc}$.

Figure 7.9: Experimental results of direct MPC during an active power reference step-down change under distorted grid conditions, $f_{\mathrm{sw}} = 5\,\mathrm{kHz}$.

7.1.2 Transient Operation

While operating under a distorted grid, as described above, the dynamic behavior of the proposed direct MPC algorithm is assessed by commanding the active power reference to step down from $P_{\mathrm{ref}} = 1\,\mathrm{p.u.}$ to $P_{\mathrm{ref}} = 0.33\,\mathrm{p.u.}$ and then back up from $P_{\mathrm{ref}} = 0.33\,\mathrm{p.u.}$ to $P_{\mathrm{ref}} = 1\,\mathrm{p.u.}$. As shown in Figs. 7.4 and 7.5, the direct MPC scheme quickly regulates all the controlled variables $\boldsymbol{y} = [\boldsymbol{i}_{\mathrm{conv}}^T\ \boldsymbol{i}_g^T\ \boldsymbol{v}_c^T]^T$—and thus the power P—to their new references with very little oscillations. In comparison, clear oscillations can be observed in the transient performance of VOC under the

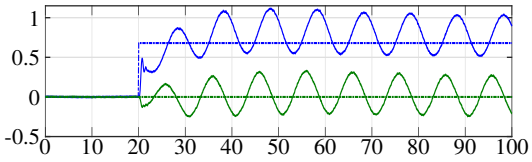

(a) Active and reactive power at the PCC.

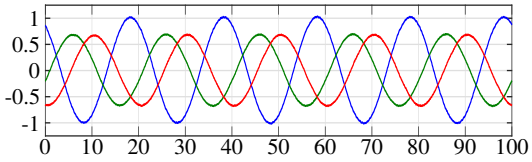

(b) Three-phase PCC voltage $\boldsymbol{v}_{\mathrm{pcc},abc}$.

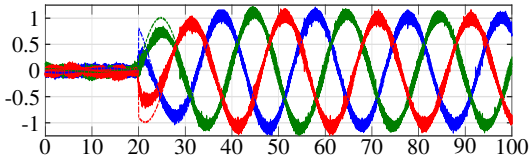

(c) Three-phase converter current $\boldsymbol{i}_{\mathrm{conv},abc}$.

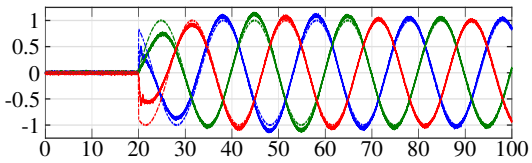

(d) Three-phase grid current $\boldsymbol{i}_{g,abc}$.

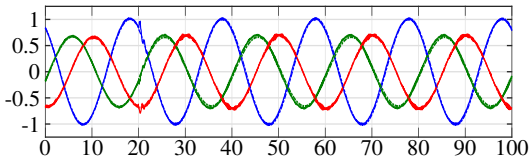

(e) Three-phase capacitor voltage $\boldsymbol{v}_{c,abc}$.

Figure 7.10: Experimental results of VOC (DSRF-CC) during an active power reference step-up change under faulty grid conditions, $f_{\mathrm{sw}} = 5\,\mathrm{kHz}$.

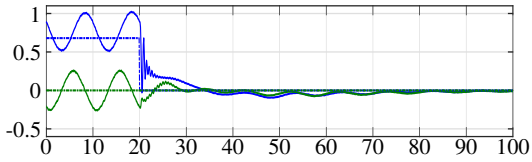

(a) Active and reactive power at the PCC.

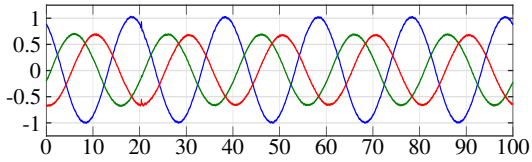

(b) Three-phase PCC voltage $\boldsymbol{v}_{\mathrm{pcc},abc}$.

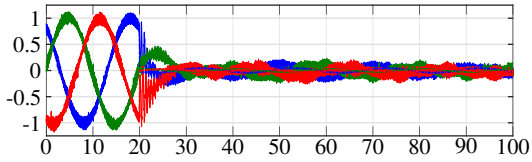

(c) Three-phase converter current $\boldsymbol{i}_{\mathrm{conv},abc}$.

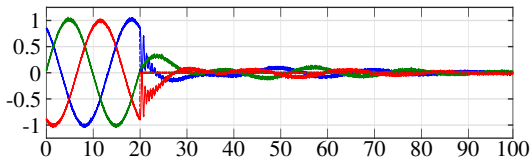

(d) Three-phase grid current $\boldsymbol{i}_{g,abc}$.

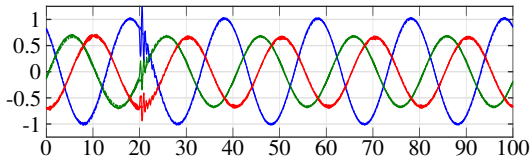

(e) Three-phase capacitor voltage $\boldsymbol{v}_{c,abc}$.

Figure 7.11: Experimental results of VOC (DSRF-CC) during an active power reference step-down change under faulty grid conditions, $f_{\mathrm{sw}} = 5\,\mathrm{kHz}$.

same scenarios, see Figs. 7.6 and 7.7, respectively. As a result, VOC is slower than the proposed direct MPC as it takes about 2.5 ms to settle to the new operating point, while it requires more than one fundamental period to fully suppress the oscillation in the active power. This is a typical behavior of linear controllers when applied to MIMO and high-order systems. More specifically, VOC addresses these system characteristics by decomposing the control problem into multiple single-input single-output (SISO) control loops. However, these loops tend to interact among each other in an adverse manner since they are not fully decoupled, and are thus

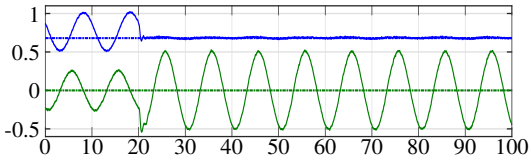

(a) Active and reactive power at the PCC.

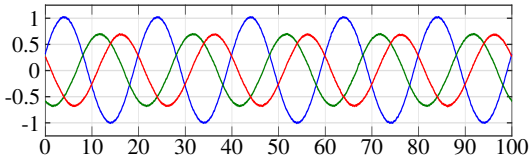

(b) Three-phase PCC voltage $\boldsymbol{v}_{\mathrm{pcc},abc}$.

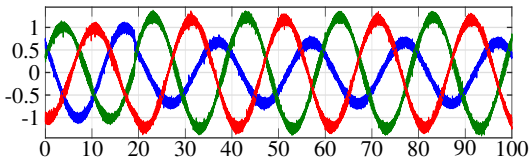

(c) Three-phase converter current $\boldsymbol{i}_{\mathrm{conv},abc}$.

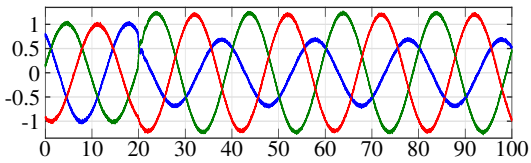

(d) Three-phase grid current $\boldsymbol{i}_{g,abc}$.

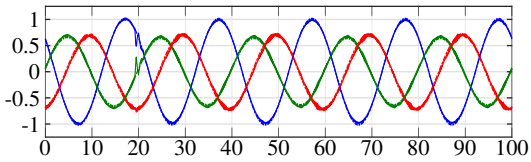

(e) Three-phase capacitor voltage $\boldsymbol{v}_{c,abc}$.

Figure 7.12: Experimental results of direct MPC during a change from BPSC to PNSC under faulty grid conditions, $f_{\mathrm{sw}} = 5\,\mathrm{kHz}$.

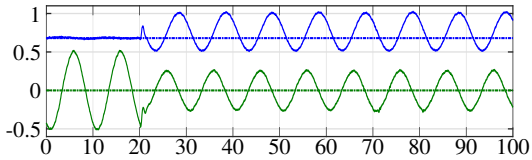

(a) Active and reactive power at the PCC.

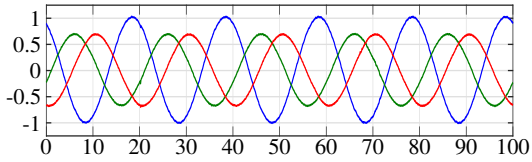

(b) Three-phase PCC voltage $\boldsymbol{v}_{\mathrm{pcc},abc}$.

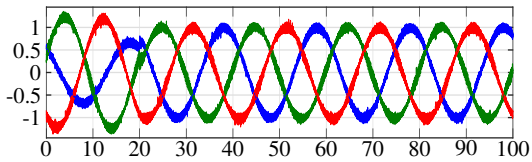

(c) Three-phase converter current $\boldsymbol{i}_{\mathrm{conv},abc}$.

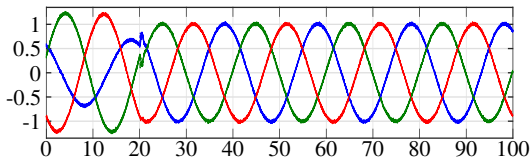

(d) Three-phase grid current $\boldsymbol{i}_{g,abc}$.

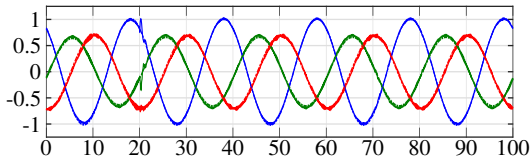

(e) Three-phase capacitor voltage $\boldsymbol{v}_{c,abc}$.

Figure 7.13: Experimental results of direct MPC during a change from PNSC to BPSC under faulty grid conditions, $f_{\mathrm{sw}} = 5\,\mathrm{kHz}$.

working in an uncoordinated manner, especially during transients. In contrast to this, the direct MPC scheme accounts for all the control objectives in one constrained optimization problem and addresses them in one computational stage. Thanks to this, MPC can tellingly reject any disturbances as control and modulation act in a fully coordinated manner.

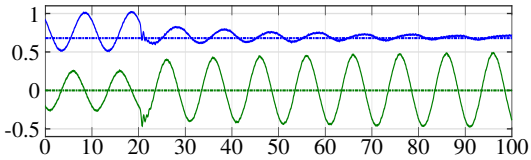

(a) Active and reactive power at the PCC.

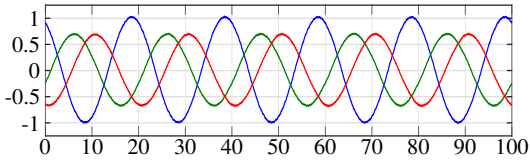

(b) Three-phase PCC voltage $\boldsymbol{v}_{\mathrm{pcc},abc}$.

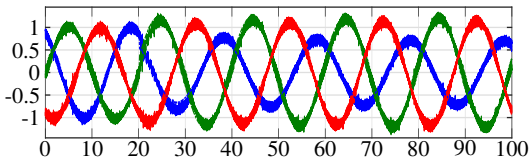

(c) Three-phase converter current $\boldsymbol{i}_{\mathrm{conv},abc}$.

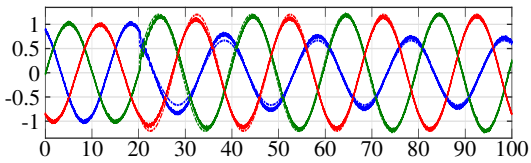

(d) Three-phase grid current $\boldsymbol{i}_{g,abc}$.

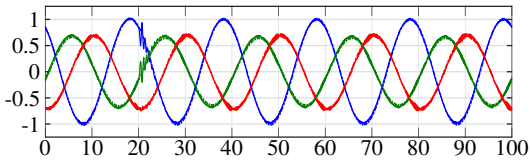

(e) Three-phase capacitor voltage $\boldsymbol{v}_{c,abc}$.

Figure 7.14: Experimental results of VOC (DSRF-CC) during a change from BPSC to PNSC under faulty grid conditions, $f_{\mathrm{sw}} = 5\,\mathrm{kHz}$.

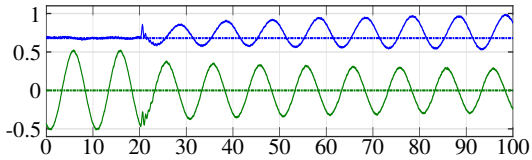

(a) Active and reactive power at the PCC.

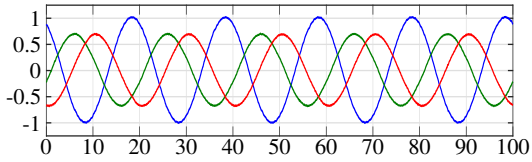

(b) Three-phase grid voltage $\boldsymbol{v}_{g,abc}$.

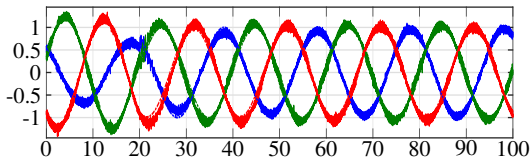

(c) Three-phase converter current $\boldsymbol{i}_{\mathrm{conv},abc}$.

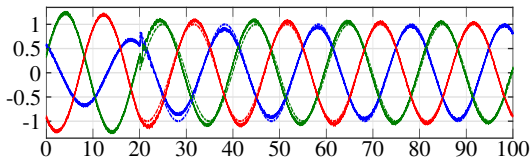

(d) Three-phase grid current $\boldsymbol{i}_{g,abc}$.

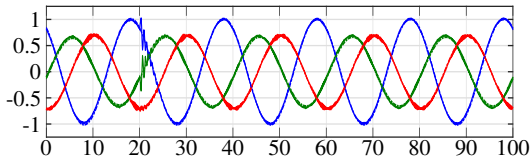

(e) Three-phase capacitor voltage $\boldsymbol{v}_{c,abc}$.

Figure 7.15: Experimental results of VOC (DSRF-CC) during a change from PNSC to BPSC under faulty grid conditions, $f_{\mathrm{sw}} = 5\,\mathrm{kHz}$.

7.2 Grid Faults

The performance of the direct MPC scheme is also examined in the presence of grid faults. More specifically, the discussed scenario considers a phase-to-phase fault in the grid voltage. Consequently, an imbalance appears in the PCC voltage as it now contains negative-sequence components as well, i.e., the PCC voltage is of the form $\boldsymbol{v}_{\mathrm{pcc}} = \boldsymbol{v}_{\mathrm{pcc},1} + \boldsymbol{v}_{\mathrm{pcc},-1}$, where it is assumed that the amplitude of the positive-sequence component is $\hat{V}_1 = 0.75\,\mathrm{p.u.}$ and that

of the negative-sequence component $\hat{V}_{-1} = 0.25$ p.u. Moreover, the BPSC strategy is used to generate the reference values fed into the proposed direct MPC method. Figs. 7.8 and 7.9 show the behavior of the system in this scenario when an active power reference step-up and step-down change is commanded at $t = 20$ ms, respectively. As shown, in both cases, the system reaches the new operating point just within 2 ms, while no oscillations are observed. Moreover, the grid currents are sinusoidal, with low harmonic content, and well balanced, as expected with the BPSC strategy.

For comparison purposes, a linear controller, namely, the decoupled double synchronous reference frame current controller (DSRF-CC) [42], is also implemented, while the cross-feedback decoupling network is used along with LPFs [61] to extract the positive- and negative-sequence current components. Its performance under the same scenarios is shown in Figs. 7.10 and 7.11. As can be seen, the transient performance of DSRF-CC is much slower compared to that of direct MPC. Especially during the power reference step-down change, not only large oscillations appear at the beginning of the transient, but also it takes almost 80 ms—which is about 40 times greater than the time required by the direct MPC scheme—to finally settle to the new operating point.

Another interesting transient scenario is the transition between the two methods that provide the output references, see Section 6.2.1.2. As shown in Figs. 7.12 and 7.13, direct MPC can seamlessly switch between BPSC and PNSC strategies, producing either a balanced three-phase current or a constant active power, respectively. In comparison, the transitions of DSRF-CC between the two methods require significantly more time, see Figs. 7.14 and 7.15. Similar to the dynamic performance shown in Figs. 7.10 and 7.11, DSRF-CC needs about 80 ms to finally reach the new reference values provided by either BPSC or PNSC. This slow dynamic response is mainly due to the LPFs in the current control loops,[1] which are necessary in the DSRF-CC scheme for attenuating the oscillations caused by the interaction between the positive- and negative-sequence current vectors.

[1]The cut-off frequency was set to $\omega_f = \omega_g/\sqrt{2}$, as suggested by many previous studies, e.g., [41, 61]. Note that the control tends to be unstable when the cut-off frequency is tuned to be either too high or too low, see [41, Section 10.3].

CHAPTER 8

Conclusion

In this work, a control software solution based on model predictive control (MPC) is developed for grid-tied variable speed drives (VSDs). More specifically, a highly efficient and reliable in-house quadratic programming (QP) solver was first developed to significantly reduce the computational burden of the MPC scheme, thus rendering the real-time implementation feasible. Then, specific control solutions are developed for both machine-side and grid-side converters.

On the machine side, the proposed MPC scheme can easily formulate all the control objectives—i.e., the machine stator current control and the inverter neutral point (NP) balancing—and the modulation problems into one constrained optimization problem. In contrast to the conventional field-oriented control (FOC) with space vector modulation (SVM), the direct MPC scheme directly manipulates the inverter switch positions to fully exploit the discrete nature of the inverter such that superior performance is achieved both at steady-state and transient operating conditions. To this aim, the direct MPC scheme implicitly introduces a fixed modulation cycle and symmetric switching patterns, i.e., akin to SVM, so that a constant switching frequency and a discrete output harmonic spectrum with low THD are achieved at steady states. Moreover, the direct MPC scheme exploits the characteristic of direct control schemes during transients, i.e., it directly manipulates the inverter switch positions such that the available dc-link voltage is fully utilized, leading to very short settling times.

On the grid side, the direct MPC strategy can successfully operate the system under nominal and faulty grid conditions. To achieve this, the reference values of the controlled variables, i.e., the grid and converter current, as well as the filter capacitor voltage, are generated to account for the different grid conditions. Subsequently, a versatile system modeling that relies on the gradient of the system output is employed to tackle the system's multi-input multi-output (MIMO) characteristics. In doing so, the design of the control and modulation problems as a unified problem is enabled. As a result, the proposed single control structure is suitable for different scenarios without requiring adjustments and/or retuning when the operating conditions change. This starkly contrasts conventional control methods that rely on linear control techniques, as these decompose the MIMO control problem into several single-input single-output (SISO) control

loops that adversely interact with each other. For this reason, retuning and gain scheduling are required when the operating point changes, leading to a cumbersome tuning procedure and a low bandwidth. These problems are further aggravated since linear control techniques—as opposed to the proposed direct MPC method—are augmented with an active damping loop, which further compromises the performance and design procedure. The superior performance of the proposed direct MPC method was verified with the presented experimental studies that related to operation under nominal conditions characterized by persistent disturbances as well as faulty grid conditions.

Nonetheless, the computational burden of MPC is still considerably high, which remains a significant obstacle to its application in power electronic systems. A possible solution to this problem is shifting computational-intensive algorithms to a field-programmable gate array (FPGA). Besides, switching patterns akin to SVM are adopted in this work. As a result, the steady-state control performance of the direct MPC scheme is similar to that of modulator-based control schemes. Further improvement can be achieved by employing more flexible pulse patterns, e.g., optimized pulse patterns (OPPs). Moreover, this work demonstrated the advantages of MPC in terms of controller bandwidth and robustness against grid faults. Its potential can be further explored by considering other more challenging scenarios encountered in modern grids. For example, the current limiting ability of the controller at voltage sags and phase jumps as well as its performance for grid support, are possible research directions.

List of Figures

List of Tables

Bibliography

[1] C. C. Chan, "The state of the art of electric, hybrid, and fuel cell vehicles," *Proceedings of the IEEE*, vol. 95, no. 4, pp. 704–718, Apr. 2007.

[2] F. Blaabjerg, R. Teodorescu, M. Liserre, and A. Timbus, "Overview of control and grid synchronization for distributed power generation systems," *IEEE Trans. Ind. Electron.*, vol. 53, no. 5, pp. 1398–1409, Oct. 2006.

[3] T. Geyer, *Model predictive control of high power converters and industrial drives*. Hoboken, NJ, USA: Wiley, 2016.

[4] J. Rodríguez, J.-S. Lai, and F. Z. Peng, "Multilevel inverters: A survey of topologies, controls, and applications," *IEEE Trans. Ind. Electron.*, vol. 49, no. 4, pp. 724–738, Aug. 2002.

[5] A. G. Beccuti, S. Mariéthoz, S. Cliquennois, S. Wang, and M. Morari, "Explicit model predictive control of dc-dc switched-mode power supplies with extended Kalman filtering," *IEEE Trans. Ind. Electron.*, vol. 56, no. 6, pp. 1864–1874, Jun. 2009.

[6] J. Rodas, F. Barrero, M. R. Arahal, C. Martín, and R. Gregor, "Online estimation of rotor variables in predictive current controllers: A case study using five-phase induction machines," *IEEE Trans. Ind. Electron.*, vol. 63, no. 9, pp. 5348–5356, Sep. 2016.

[7] D. J. Atkinson, P. P. Acarnley, and J. W. Finch, "Observers for induction motor state and parameter estimation," *IEEE Trans. Ind. Appl.*, vol. 27, no. 6, pp. 1119–1127, Dec. 1991.

[8] P. Karamanakos and T. Geyer, "Guidelines for the design of finite control set model predictive controllers," *IEEE Trans. Power Electron.*, vol. 35, no. 7, pp. 7434–7450, Jul. 2020.

[9] J. Rodríguez and P. Cortés, *Predictive control of power converters and electrical drives*. Chichester, UK: Wiley, 2012.

[10] R. Vargas, P. Cortes, U. Ammann, J. Rodriguez, and J. Pontt, "Predictive control of a three-phase neutral-point-clamped inverter," *IEEE Trans. Ind. Electron.*, vol. 54, no. 5, pp. 2697–2705, Aug. 2007.

[11] P. Karamanakos, T. Geyer, and R. Kennel, "On the choice of norm in finite control set model predictive control," *IEEE Trans. Power Electron.*, vol. 33, no. 8, pp. 7105–7117, Sep. 2018.

[12] T. Geyer and D. E. Quevedo, "Multistep finite control set model predictive control for power electronics," *IEEE Trans. Power Electron.*, vol. 29, no. 12, pp. 6836–6846, Dec. 2014.

[13] E. Liegmann, P. Karamanakos, and R. Kennel, "Real-time implementation of long-horizon direct model predictive control on an embedded system," *IEEE Open J. Ind. Appl.*, vol. 3, pp. 1–12, 2022.

[14] E. Liegmann, P. Karamanakos, T. Geyer, T. Mouton, and R. Kennel, "Long-horizon direct model predictive control with active balancing of the neutral point potential," in *Proc. IEEE Int. Symp. Pred. Control of Elect. Drives and Power Electron.*, Pilsen, Czech Republic, Sep. 2017, pp. 89–94.

[15] T. Geyer, "A comparison of control and modulation schemes for medium-voltage drives: Emerging predictive control concepts versus PWM-based schemes," *IEEE Trans. Ind. Appl.*, vol. 47, no. 3, pp. 1380–1389, May/Jun. 2011.

[16] M. Rossi, P. Karamanakos, and F. Castelli-Dezza, "An indirect model predictive control method for grid-connected three-level neutral point clamped converters with LCL filters," *IEEE Trans. Ind. Appl.*, vol. 58, no. 3, pp. 3750–3768, May/Jun. 2022.

[17] D. G. Holmes and T. A. Lipo, *Pulse Width Modulation for Power Converters: Principles and Practice*. Piscataway, NJ: IEEE Press, 2003.

[18] C. Xue, D. Zhou, and Y. Li, "Hybrid model predictive current and voltage control for LCL-filtered grid-connected inverter," *IEEE J. Emerg. Sel. Topics Power Electron.*, vol. 9, no. 5, pp. 5747–5760, Oct. 2021.

[19] F. Toso, A. Favato, R. Torchio, P. Alotto, and S. Bolognani, "Continuous control set model predictive current control of a microgrid-connected PWM inverter," *IEEE Trans. Power Syst.*, vol. 36, no. 1, pp. 415–425, Jan. 2021.

[20] S. Vazquez, A. Marquez, R. Aguilera, D. Quevedo, J. I. Leon, and L. G. Franquelo, "Predictive optimal switching sequence direct power control for grid-connected power converters," *IEEE Trans. Ind. Electron.*, vol. 62, no. 4, pp. 2010–2020, Apr. 2015.

[21] A. Mora, R. Cárdenas-Dobson, R. P. Aguilera, A. Angulo, F. Donoso, and J. Rodríguez, "Computationally efficient cascaded optimal switching sequence MPC for grid-connected three-level NPC converters," *IEEE Trans. Power Electron.*, vol. 34, no. 12, pp. 12 464–12 475, Dec. 2019.

[22] P. Karamanakos, R. Mattila, and T. Geyer, "Fixed switching frequency direct model predictive control based on output current gradients," in *Proc. IEEE Ind. Electron. Conf.*, Washington, D.C., USA, Oct. 2018, pp. 2329–2334.

[23] P. Karamanakos, M. Nahalparvari, and T. Geyer, "Fixed switching frequency direct model predictive control with continuous and discontinuous modulation for grid-tied converters with LCL filters," *IEEE Trans. Control Syst. Technol.*, vol. 29, no. 4, pp. 1503–1518, 2021.

[24] P. Karamanakos, E. Liegmann, T. Geyer, and R. Kennel, "Model predictive control of power electronic systems: Methods, results, and challenges," *IEEE Open J. Ind. Appl.*, vol. 1, pp. 95–114, 2020.

[25] D. Kouzoupis, A. Zanelli, H. Peyrl, and H. J. Ferreau, "Towards proper assessment of QP algorithms for embedded model predictive control," in *Proc. of the Eur. Control Conf.*, Linz, Austria, Jul. 2015, pp. 2609–2616.

[26] Q. Yang, P. Karamanakos, W. Tian, X. Gao, X. Li, T. Geyer, and R. Kennel, "Computationally efficient fixed switching frequency direct model predictive control," *IEEE Trans. Power Electron.*, vol. 37, no. 3, pp. 2761–2777, Mar. 2022.

[27] Q. Yang, P. Karamanakos, E. Liegmann, W. Tian, T. Geyer, R. Kennel, and M. L. Heldwein, "A fixed switching frequency direct model predictive control for neutral-point-clamped three-level inverters with induction machines," *IEEE Trans. Power Electron.*, vol. 38, no. 11, pp. 13 703–13 716, Nov. 2023.

[28] Q. Yang, P. Karamanakos, W. Tian, T. Geyer, R. Kennel, and M. L. Heldwein, "A fixed switching frequency direct model predictive control for grid-tied converters with lcl filters under adverse grid conditions," *IEEE J. Emerg. Sel. Topics Power Electron.*, 2024.

[29] B. McGrath, D. Holmes, and T. Lipo, "Optimized space vector switching sequences for multilevel inverters," *IEEE Trans. Power Electron.*, vol. 18, no. 6, pp. 1293–1301, Nov. 2003.

[30] K. Hasse, "Zum dynamischen verhalten der asynchronmaschine bei betrieb mit variabler standerfrequenz und standerspannung," *ETZ-A Bd.*, vol. 89, p. 77, 1968.

[31] S. Ogasawara and H. Akagi, "Analysis of variation of neutral point potential in neutral-point-clamped voltage source PWM inverters," in *Proc. IEEE Ind. Appl. Soc. Annu. Mtg.*, vol. 2, Toronto, ON, Canada, Oct. 1993, pp. 965–970.

[32] C. Newton and M. Sumner, "Neutral point control for multi-level inverters: theory, design and operational limitations," in *Proc. IEEE Ind. Appl. Soc. Annu. Mtg.*, New Orleans, LA, USA, Oct. 1997, pp. 1336–1343.

[33] C. Wang and Y. Li, "Analysis and calculation of zero-sequence voltage considering neutral-point potential balancing in three-level npc converters," *IEEE Trans. Ind. Electron.*, vol. 57, no. 7, pp. 2262–2271, Jul. 2010.

[34] H. Akagi, E. H. Watanabe, and M. Aredes, *Instantaneous power theory and applications to power conditioning*. John Wiley & Sons, 2017.

[35] "Ieee recommended practices and requirements for harmonic control in electrical power systems," *IEEE Standard 519-2014 (Revision of IEEE Std 519-1992)*, pp. 1–29, Jul. 2014.

[36] M. Liserre, F. Blaabjerg, and S. Hansen, "Design and control of an lcl-filter-based three-phase active rectifier," *IEEE Trans. Ind. Appl.*, vol. 41, no. 5, pp. 1281–1291, Sep./Oct. 2005.

[37] J. Dannehl, F. W. Fuchs, S. Hansen, and P. B. Thøgersen, "Investigation of active damping approaches for pi-based current control of grid-connected pulse width modulation converters with lcl filters," *IEEE Trans. Ind. Appl.*, vol. 46, no. 4, pp. 1509–1517, Jul./Aug. 2010.

[38] V. Kaura and V. Blasko, "Operation of a phase locked loop system under distorted utility conditions," *IEEE Trans. Ind. Appl.*, vol. 33, no. 1, pp. 58–63, Jan./Feb. 1997.

[39] P. Rodriguez, J. Pou, J. Bergas, J. I. Candela, R. P. Burgos, and D. Boroyevich, "Decoupled double synchronous reference frame pll for power converters control," *IEEE Trans. Power Electron.*, vol. 22, no. 2, pp. 584–592, 2007.

[40] M. H. Bollen and L. Zhang, "Different methods for classification of three-phase unbalanced voltage dips due to faults," *Electric power systems research*, vol. 66, no. 1, pp. 59–69, 2003.

[41] R. Teodorescu, M. Liserre, and P. Rodriguez, *Grid converters for photovoltaic and wind power systems*. John Wiley & Sons, 2011.

[42] H.-S. Song and K. Nam, "Dual current control scheme for PWM converter under unbalanced input voltage conditions," *IEEE Trans. Ind. Electron.*, vol. 46, no. 5, pp. 953–959, Oct. 1999.

[43] T. Geyer, P. Karamanakos, and R. Kennel, "On the benefit of long-horizon direct model predictive control for drives with LC filters," in *Proc. IEEE Energy Convers. Congr. Expo.*, Pittsburgh, PA, USA, Sep. 2014, pp. 3520–3527.

[44] T. Geyer, "Algebraic tuning guidelines for model predictive torque and flux control," *IEEE Trans. Ind. Appl.*, vol. 54, no. 5, pp. 4464–4475, Sep./Oct. 2018.

[45] L. Ben-Brahim and A. Kawamura, "Digital control of induction motor current with deadbeat response using predictive state observer," *IEEE Trans. Power Electron.*, vol. 7, no. 3, pp. 551–559, Jul. 1992.

[46] J. Nocedal and S. Wright, *Numerical optimization*, 2nd ed. New York, NY, USA: Springer, 2006.

[47] S. Richter, T. Geyer, and M. Morari, "Resource-efficient gradient methods for model predictive pulse pattern control on an FPGA," *IEEE Trans. Control Syst. Technol.*, vol. 25, no. 3, pp. 828–841, May 2017.

[48] A. B. Németh and S. Z. Németh, "How to project onto an isotone projection cone," *Linear Algebra Appl.*, vol. 433, no. 1, pp. 41–51, Jul. 2010.

[49] S. Boyd and L. Vandenberghe, *Convex Optimization*. Cambridge, UK: Cambridge Univ. Press, 2004.

[50] J. Barzilai and J. M. Borwein, "Two-point step size gradient methods," *IMA J. of Num. Anal.*, vol. 8, no. 1, pp. 141–148, Jan. 1988.

[51] Y.-H. Dai and R. Fletcher, "New algorithms for singly linearly constrained quadratic programs subject to lower and upper bounds," *Math. Program.*, vol. 106, no. 3, pp. 403–421, May 2006.

[52] R. Fletcher, "On the Barzilai-Borwein method," in *Optim. and Control with Appl.* Boston, MA, USA: Springer, 2005, pp. 235–256.

[53] Y.-H. Dai and R. Fletcher, "Projected Barzilai-Borwein methods for large-scale box-constrained quadratic programming," *Numer. Math.*, vol. 100, no. 1, pp. 21–47, Mar. 2005.

[54] Y. Nesterov, *Introductory lectures on convex optimization: A basic course*. Springer Science & Business Media, 2003, vol. 87.

[55] S. Richter, C. N. Jones, and M. Morari, "Real-time input-constrained mpc using fast gradient methods," in *Proc. IEEE Conf. Decis. Control*, Shanghai, China, Dec. 2009, pp. 7387–7393.

[56] G. M. Joksimovic, J. Riger, T. M. Wolbank, N. Peric, and M. Vasak, "Stator-current spectrum signature of healthy cage rotor induction machines," *IEEE Trans. Ind. Electron.*, vol. 60, no. 9, pp. 4025–4033, Sep. 2013.

[57] J.-K. Seok, J.-S. Kim, and S.-K. Sul, "Overmodulation strategy for high-performance torque control," *IEEE Trans. Power Electron.*, vol. 13, no. 4, pp. 786–792, Jul. 1998.

[58] D. Schröder and J. Böcker, *Elektrische antriebe-regelung von antriebssystemen*. Springer, 2009, vol. 2.

[59] K. Yamanaka, A. Hava, H. Kirino, Y. Tanaka, N. Koga, and T. Kume, "A novel neutral point potential stabilization technique using the information of output current polarities and voltage vector," *IEEE Trans. Ind. Appl.*, vol. 38, no. 6, pp. 1572–1580, Nov./Dec. 2002.

[60] H. du Toit Mouton, "Natural balancing of three-level neutral-point-clamped pwm inverters," *IEEE Trans. Ind. Electron.*, vol. 49, no. 5, pp. 1017–1025, Oct. 2002.

[61] P. Rodriguez, J. Pou, J. Bergas, J. I. Candela, R. P. Burgos, and D. Boroyevich, "Decoupled double synchronous reference frame PLL for power converters control," *IEEE Trans. Power Electron.*, vol. 22, no. 2, pp. 584–592, Mar. 2007.

[62] H. Akagi, E. H. Watanabe, and M. Aredes, *Instantaneous power theory and applications to power conditioning*. John Wiley & Sons, 2017.

[63] G. Pannocchia, M. Gabiccini, and A. Artoni, "Offset-free MPC explained: Novelties, subtleties, and applications," *IFAC-PapersOnLine*, vol. 48, no. 23, pp. 342–351, 2015.

[64] C. Bao, X. Ruan, X. Wang, W. Li, D. Pan, and K. Weng, "Step-by-step controller design for LCL-type grid-connected inverter with capacitor–current-feedback active-damping," *IEEE Trans. Power Electron.*, vol. 29, no. 3, pp. 1239–1253, Mar. 2014.

[65] V. Blasko and V. Kaura, "A novel control to actively damp resonance in input LC filter of a three-phase voltage source converter," *IEEE Trans. Ind. Appl.*, vol. 33, no. 2, pp. 542–550, Mar./Apr. 1997.

[66] S. G. Parker, B. P. McGrath, and D. G. Holmes, "Regions of active damping control for LCL filters," *IEEE Trans. Ind. Appl.*, vol. 50, no. 1, pp. 424–432, Jan./Feb. 2014.